Static and Dynamic Response of a Sandwich Structure Under Axial Compression

by

Wooseok Ji

A dissertation submitted in partial fulfillment
of the requirements for the degree of
Doctor of Philosophy
(Aerospace Engineering)
in The University of Michigan
2008

Doctoral Committee:

Professor Anthony M. Waas, Chair
Professor Alan Wineman
Assistant Professor Veera Sundararaghavan
Professor Zdeněk Bažant, Northwestern University

To my parents and my lovely wife.

ACKNOWLEDGEMENTS

None other than my advisor, Anthony Waas, can top the list of people I would like to take the opportunity here to thank. He accepted me into his environment and guided me through with his unlimited patience and energy. My respect for him as a researcher, engineer, and human being is unparalleled. His support, guidance, and advice have been invaluable and deserve a special recognition. Thank you for your continuous support and advice throughout the past five years. It has been an extremely educational and rewarding experience. I have enjoyed the enthusiasm and energy that you have brought towards all aspects of my life at Michigan. I have enjoyed working with you tremendously and I hope we will continue to do so for years to come.

I am also very grateful to all the members of my doctoral committee: Zednek Bazant, Alan Wineman, and Veera Sundararaghavan. It has been a privilege to have all of them participated in this important part of my life's work. All of them have been sources of inspiration and support in various stages of my dissertation, through their writings and in person. Without their suggestions, timely advice, and comprehensive understanding of various aspects of my study, my work would not have taken this shape and direction. I am also deeply grateful to Professor Dan Adams of the Mechanical Engineering Department at the University of Utah for supplying they sandwich panels for my experiment.

My gratitude is also extended to my PhD colleagues and everyone of my research

group for all of their support and help throughout the years. Shiladitya Basu, Shunjun Song, Pete Gustafson, Wey Heok Ng, Scott Stapleton, and Evan Pineda, I have always enjoyed your company and all our conversations inside and outside the lab. It has been great meeting all of you and communicating and working with you. Special words of thanks apply to Amit Salvi for his invaluable help in the lab and for always taking time to discuss my model, my results, and our lives. I would be remiss if I didn't recognize Jiwon Mok. She has become a great friend over the last few years and I owe her many debts of gratitude.

My admiration and gratitude go out to my family member in Korea; my brother, my parents, my parents-in-law, and my brother-in-law for supporting my study abroad and encouragement throughout my life. I am grateful for their unfailing love and support that has been very rewarding. I attribute my success to their reassuring love and sacrifice. Last, but certainly not least, I must thank Sandra, the most wonderful woman and best friend in my life. Through her love, patience, support, and unwavering belief in me, I have been able to complete this long dissertation journey. Thank you with all my heart and soul. I am forever indebted to you for giving me life, your love, and your heart. I love you more than yesterday, but less than I will tomorrow.

TABLE OF CONTENTS

LIST OF FIGURES

Figure

LIST OF TABLES

Table

CHAPTER I

Introduction

1.1 Introduction

Sandwich structures, constructed by bonding two stiff, thin-walled face sheets to a light weight, relatively flexible thick core, are widely used in various industrial applications demanding a high bending stiffness per unit weight. The large separation introduced by the relatively thick and low stiffness core and the relatively thin and high axial stiffness of the face sheets (compared to the core) aid in effectively increasing the thickness of the sandwich beam, leading to a large bending stiffness per unit weight. Under in-plane compression, a sandwich structure has a very different failure mechanism than a corresponding monolithic structure. Typical sandwich panels are shown in Fig. 1.1. Failure of a sandwich beam under end compression is by a number of competing mechanisms, two of which are global and local buckling instabilities.

Many useful theoretical analyses have been conducted in the past to analyze the global and local buckling of a sandwich beam. Many of these studies modeled the face sheet as an Euler-Bernoulli beam [45, 37, 22, 1, 43] with the differences among the analyses being in the modeling method of the core. Plantema [45] assumed exponential functions to describe the stress decay away from the face sheet into the core, so that the displacements of the face sheet which are transmitted to the core

damp out rapidly in the thickness direction. Léotoing et al. [37], and Frostig and Baruch [22], assumed the core as a linear elastic foundation, and applied a higher-order theory to describe the displacement fields of the core. In the analysis of Allen [1] and Niu and Talreja [43], the core is assumed to be a elastic isotropic material. They suggested a unified expression for the wrinkling stresses of the possible deformation modes expressed through a case parameter, when the beam is pinned at each end. The effect of the core shear response and its incorporation in carrying out non-linear material and kinematic analyses are addressed in the work of Bažant and Beghini [6], and Beghini et al. [10]. A comprehensive review of past work in sandwich beam buckling studies, up to 1998, is contained in the review by Ley et al. [39].

A number of experimental studies have also been performed to investigate compression response. Fleck and Sridhar [20] tested various sandwich columns made of different combination of material and having different geometrical properties. They observed different failure modes depending on the material properties of the core and geometrical properties of the column. Fagerberg [19] uncovered a transition in the failure mode by examining sandwich beams of different core stiffness. He postulated that the transition from wrinkling to pure compression failure of the face sheet occurs when the modulus of the core is sufficient to support the face sheet, in effect a sandwich beam with a high ratio of E_c/E_f, where E_c is the core Young's modulus and E_f the face sheet Young's modulus.

Despite of the wide ranging engineering applications of sandwich structures and the many theoretical and experimental studies on the static response of such structures, the dynamic response of sandwich structures subjected to dynamic compressive loading has not received as much attention. Since the outstanding capability of absorbing impact energy due to a tailorable core material, "optimized" sandwich

structures are now widely being considered for structural systems where crashworthiness is an important requirement. Examples are floors of helicopters, the crew exploration vehicle (CEV) of NASA and several ship structures.

Previous work in the dynamic domain has focused on transverse loading of sandwich structures, with respect to blast protection [21, 51, 59, 57]. However, an equally important consideration for structural integrity and collapse is a thorough understanding of the response and failure of a sandwich structure when subjected to short duration axial loading. For instance, modern ships used by the US navy that consist of acreage application of sandwich panels can, under extreme condition such as impacting a glazier, be subjected to suddenly applied axial compressive loads.

The objective of the present thesis is, therefore, to explore the differences in response of a sandwich structure when subjected to static and dynamic axial compressive loads. To achieve this objective, a sandwich beam type structure is studied, both theoretically and experimentally. At the time of writing this thesis, several publications related to the thesis work were already prepared. As a result, several chapters in the thesis are self contained publications that have already appeared in journals or are currently under review and in preparation. Where this is the case, a footnote will indicate so.

1.2 Organization of the thesis

The next two chapters of this thesis address the static buckling of a sandwich beam, where each constituent (core and face sheet) is treated within the framework of 2D linear elasticity. Both periodic and non-periodic buckling modes are addressed and the importance of choosing the correct work–conjugate stress and strain measure in formulating the buckling problem is discussed. The analysis presented can be used

as a benchmark in comparing other simplified sandwich beam models (for example, when face sheets are treated as Euler-Bernoulli or Timoshenko beams) as well as finite element based solution.

Chapter IV addresses the dynamic buckling of an impacted column and the time evolution of the buckle pattern in the case of a slightly imperfect column. Initially, new ideas related to the notion of a "critical time to buckle" are introduced using a monolithic Euler-Bernoulli beam column that is suddenly impacted by a falling mass. Next, the analysis is extended to a thick sandwich column, where the thin face sheets are treated as beam-columns and the core as an equivalent elastic foundation.

Chapter V presents the result of an experimental study on the static response of an axially compressed sandwich column. Different column length as well as different ratios of face sheet to core thickness are investigated. Different failure modes are identified and the result from the experiments are compared against theoretical and finite element based prediction.

Chapter VI contains the result of an experimental study on the dynamic buckling of a sandwich column. Sandwich columns of various lengths are subjected to axial impact by a falling mass. Time dependent load and strain data with ultra high-speed imaging are used to capture the dynamic buckling event. The experimental results are compared against analytical studies of Chapter IV and finite element based simulation of the impact event. Final conclusion and a summary of findings are presented in Chapter VII along with suggestions for future work.

1.3 Original contributions of the thesis

1. A comprehensive 2D elastic analysis of a sandwich column under axial compression loading has been conducted. The solution for both periodic and non-

periodic buckling modes can be used as a benchmark to verify other simplified models of sandwich columns and finite element based computation.

2. Using a 2D elasticity formulation (where both the face sheets and core are treated as 2D elastic continua), the proper work conjugate measure for sandwich beam buckling have been formulated, extending previous work by Bažant [5, 9, 6]. The correct FE formulation of the 2D buckling problem has been presented.

3. The "critical time to buckle", a new notion that corresponds to the critical load in static buckling of columns, has been introduced and quantified for a column that is impacted at one end. The formulation has been extended to sandwich column using a beam on an elastic foundation model.

4. A comprehensive set of experimental results in support of the theoretical findings in items 1, 2, and 3 have been presented. In addition, new failure mechanisms and the temporal history of how a sandwich column responds to axial impact has been uncovered through the experimental results.

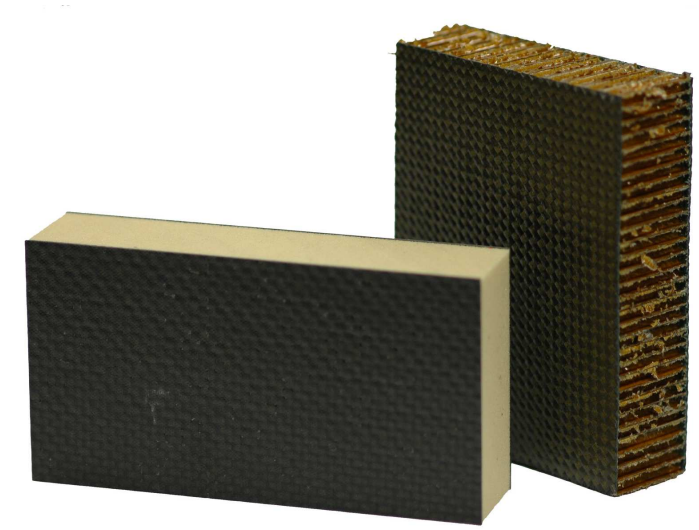

(a)

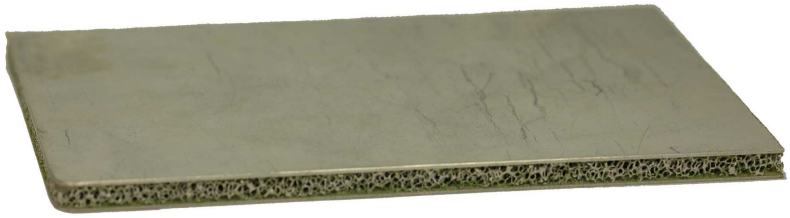

(b)

Figure 1.1: Typical examples of sandwich constructions. (a) composite laminates face sheets covering a PVC foam core or a aramid honeycomb core (b) Aluminum face sheets with a aluminum foam core

CHAPTER II

Exact elastic solution of the sandwich beam buckling problem[1]

2.1 Introduction

Most theories on static stability problems of a compressively loaded sandwich beam have been developed with their own sets of assumptions. These assumptions are typically made on the basis of the beam geometry, the material behavior, and the buckling deformation mode. Many theoretical analyses for sandwich structures have been conducted in the past with the assumption of an isotropic core with 'thin' face sheets, e.g., foam cores covered with metal or quasi-isotropic thin fiber-reinforced laminate skins [1, 22, 38, 43, 45]. However, many sandwich structural components used in various industrial applications consist of cores with orthotropic phases and with face sheets whose thickness can be an appreciable amount of the core thickness. The latter is true in applications involving heavily loaded marine structures. In addition to the assumptions made on the geometry and the material, the most common assumption on the buckling deformation mode is that of periodicity. A large number of analytical predictions on global and local instabilities of sandwich panels have been derived, assuming that the buckling deformation mode is sinusoidal [1, 22, 30, 33, 38, 43, 45]. This assumption on the deformation mode precludes the

[1]The results in this chapter have been published as journal articles. See Ref. [30] and [29] in the bibliography.

possibility of a non-uniform buckling mode, which can sometimes occur at a lower externally applied load than the corresponding load for the periodic buckling mode.

In previous studies, the modeling methods for the face sheets and the core have also included different sets of assumptions. Typically, the face sheets are modeled as Euler-Bernoulli beams [1, 22, 38, 43, 45], with the differences among the analyses being in the modeling method of the core. The core can be assumed as a model of linear decay of through-the-thickness deflections [1], a high-order transversely flexible material [22], an elastic foundation [38], a linear elastic isotropic material [43], a model of exponential decay of through-the-thickness deflections [45], and so on. Since these assumptions are valid when certain specific conditions are satisfied, it is important to determine the range of validity of these previous theoretical studies with respect to accuracy.

Bažant and co-workers [6, 7, 8, 10] have systematically evaluated the effect of core shear on buckling of sandwich beams where the face sheets are treated as beams. Using an energetic variational analysis of critical loads and the initial post-critical response, these studies have shown the form of the proper tangent shear modulus that needs to be used in conjunction with different formulations of sandwich panel buckling problems. Even though the significance of the proper conjugate incremental stress and incremental strain measure for buckling problem was introduced as early as 1971 [5], it appears that the importance of these findings with respect to the sandwich beam buckling problem have gone unnoticed.

The sandwich beam model considered here treats both the face sheet and core as linear elastic two-dimensional (2D) continua. The materials can be either orthotropic or isotropic. Very general deformation modes are considered corresponding to find various buckling deformation modes and corresponding buckling loads. This com-

prehensive analysis on the general static instability problem of a sandwich beam is based on the constituents remaining linear elastic.

In developing the analysis, the procedure to find the critical buckling stress is discussed first, based on two possible buckling deformation modes of the beam: one is referred to as wrinkling and the other as edge buckling. Both are short wavelength buckling modes. The results obtained are compared with previous theoretical and experimental results. Finite Element Analyses (FEA) are performed to support the theoretical predictions.

2.2 Problem formulation

2.2.1 Theoretical study

The sandwich panel to be studied here is schematically illustrated in Fig. 2.1. The top face sheet and the bottom face sheet with thickness of t^t and t^b, respectively, are separated by the core of thickness t^c. Perfect bonding is enforced at the interfaces between the face sheets and the core. Local cartesian coordinate systems are assigned to each layer with superscripts t, c, and b denoting the top face sheet, the core, and the bottom face sheet, respectively. This nomenclature will be applied to any quantity defined in this paper. The sandwich panel is subject to axial compressive loading and assumed to undergo a plane strain deformation in the xz–plane. It is of interest to inquire the existence of a new equilibrium state where the deformed configuration is not the trivial uniform straining parallel to the x–axis. The method to solve this buckling problem is similar to what has been presented by by Fu and Waas for the 2D thick orthotropic ring [23], Ji and Waas for periodic buckling of sandwich beams [30], and for the 2D fiber micro buckling of a layered material [53].

Bažant and Beghini [6, 7] showed that, for sandwich type structures with a soft core situated at the middle, the Green–Lagrange strain measure must be used if the

strains are small and the elastic moduli are kept constant throughout the analysis. The objective stress measure, which is energetically conjugate to the Green–Lagrange strain measure, is the second Piola–Kirchhoff stress, σ_{ij}, and the corresponding incremental stress measure is the Trefftz stress $\tau_{ij} = \sigma'_{ij} + \sigma^0_{kj} u_{i,k}$. A superscript "0" is used to identify quantities associated with the initial position of equilibrium while a superscript " $'$ " denotes those quantities arising due to the disturbance from the initial state of stress. Then, the field equations governing the incremental stresses arising due to the perturbation in the x–direction from the uniformly strained state are,

$$
\begin{aligned}
&\frac{\partial}{\partial x}\left[\sigma'_{xx} + \sigma^0_{xx}\frac{\partial u}{\partial x}\right] + \frac{\partial \sigma'_{xy}}{\partial y} + \frac{\partial \sigma'_{xz}}{\partial z} = 0 \\
&\frac{\partial}{\partial x}\left[\sigma'_{xy} + \sigma^0_{xx}\frac{\partial v}{\partial x}\right] + \frac{\partial \sigma'_{yy}}{\partial y} + \frac{\partial \sigma'_{zy}}{\partial z} = 0 \\
&\frac{\partial}{\partial x}\left[\sigma'_{xz} + \sigma^0_{xx}\frac{\partial w}{\partial x}\right] + \frac{\partial \sigma'_{yz}}{\partial y} + \frac{\partial \sigma'_{zz}}{\partial z} = 0
\end{aligned}
\tag{2.1}
$$

The face sheets and core are assumed to be homogeneous and linearly elastic orthotropic solids. Consequently, it is assumed that the perturbed stresses are related to the perturbed strains in the same manner as in the unperturbed material. Therefore, the stress-strain relationship without "$'$" for simplicity is

$$
\begin{Bmatrix} \sigma^i_{xx} \\ \sigma^i_{yy} \\ \sigma^i_{zz} \\ \sigma^i_{yz} \\ \sigma^i_{xz} \\ \sigma^i_{xy} \end{Bmatrix} =
\begin{bmatrix}
c^i_{11} & c^i_{12} & c^i_{13} & 0 & 0 & 0 \\
c^i_{12} & c^i_{22} & c^i_{23} & 0 & 0 & 0 \\
c^i_{13} & c^i_{23} & c^i_{33} & 0 & 0 & 0 \\
0 & 0 & 0 & c^i_{44} & 0 & 0 \\
0 & 0 & 0 & 0 & c^i_{55} & 0 \\
0 & 0 & 0 & 0 & 0 & c^i_{66}
\end{bmatrix}
\begin{Bmatrix} e^i_{xx} \\ e^i_{yy} \\ e^i_{zz} \\ 2e^i_{yz} \\ 2e^i_{xz} \\ 2e^i_{xy} \end{Bmatrix}
\qquad (i = t,\ c,\ or\ b)
\tag{2.2}
$$

where c^i_{jk} are the stiffness constants and e^i_{jk} are the linearized strain components. Note that the specific elastic moduli corresponding to the incremental stresses ex-

pressed in the field equation Eq. (2.1) are used. The strains associated with the incremental displacements are simplified to the form of

$$e^i_{jk} = \frac{1}{2}\left(u^i_{j,k} + u^i_{k,j}\right) \tag{2.3}$$

by employment of the classical linear elasticity theory [44].

Using the above constitutive relations, Eq. (2.2), and the strain–displacement relations, Eq. (3.3), to eliminate the stress in favor of the strains in Eq. (2.1), yields,

$$\begin{aligned} (c^i_{11} - \sigma^i)\frac{\partial^2 u^i}{\partial {x^i}^2} + c^i_{55}\frac{\partial^2 u^i}{\partial {z^i}^2} + (c^i_{13} + c^i_{55})\frac{\partial^2 w^i}{\partial x^i \partial z^i} = 0 \\ c^i_{33}\frac{\partial^2 w^i}{\partial {z^i}^2} + \left(c^i_{55} - \sigma^i\right)\frac{\partial^2 w^i}{\partial {x^i}^2} + \left(c^i_{13} + c^i_{55}\right)\frac{\partial^2 u^i}{\partial x^i \partial z^i} = 0 \end{aligned} \tag{2.4}$$

where σ^i is the initial stress applied to each layer. Note that the second equation of Eq. (2.1) is automatically satisfied due to the restriction to a plane strain deformation in the xz–plane.

The general nontrivial solution to Eq. (2.4) proceeds by seeking to examine the presence of general deformed states of adjacent equilibrium. Thus, let the solutions to Eqs. (2.4) be

$$\begin{aligned} u^i(x^i,\ z^i) = e^{-\alpha x^i}\psi(z^i) \\ w^i(x^i,\ z^i) = e^{-\alpha x^i}\phi(z^i) \end{aligned} \tag{2.5}$$

where $\alpha = p + ri$ and i is the imaginary number, defined as $i = \sqrt{-1}$. Note that the exponential function is used to represent the general buckling deformation mode in the x–direction. For example, if $p = 0$, then Eq. (2.5) represents the typical sine-wave type of deformation in the x–direction. Many previous studies assumed periodic buckling modes in problems of global and local instabilities of uniformly strained sandwich structure, but it has been shown that the sinusoidal assumption is not always justified in the sandwich buckling problem [25, 29].

Assuming that the sandwich beam is symmetrical, i.e., the top and the bottom face sheet have identical geometrical and material properties, only one half of the beam need to be considered in this analysis. Substituting Eq. (2.5) into Eq. (2.4) and solving for $\psi(z^i)$ and $\phi(z^i)$, the following characteristic equation is obtained:

$$\lambda^4 - 2\Big\{\left(1+\frac{1}{2\beta_2^i}\right)s^i - \beta_1^i + \frac{\beta_3^i+\beta_3^{i^2}}{\beta_2^i}\Big\}\alpha^2\lambda^2 + \alpha^4\frac{1}{\beta_2^i}(1-2s^i)(\beta_1^i - s^i) = 0, \tag{2.6}$$

where $\beta_1^i = c_{11}^i/2c_{55}^i$, $\beta_2^i = c_{33}^i/2c_{55}^i$, $\beta_3^i = c_{13}^i/2c_{55}^i$, and $s^i = \sigma^i/2c_{55}^i$. The four roots of the characteristic equation are

$$\begin{aligned}
\lambda_1 &= \alpha\sqrt{\rho_1+\rho_2} \\
\lambda_2 &= -\alpha\sqrt{\rho_1+\rho_2} = -\lambda_1 \\
\lambda_3 &= \alpha\sqrt{\rho_1-\rho_2} \\
\lambda_4 &= -\alpha\sqrt{\rho_1-\rho_2} = -\lambda_3,
\end{aligned}$$

where

$$\begin{aligned}
\rho_1 &= \left(1+\frac{1}{2\beta_2^i}\right)s^i - \beta_1^i + \frac{\beta_3^i+\beta_3^{i^2}}{\beta_2^i} \\
\rho_2 &= \sqrt{{\rho_1}^2 - \frac{1}{\beta_2^i}(1-2s^i)(\beta_1^i - s^i)}.
\end{aligned}$$

Applying the general material properties of the sandwich beam for ρ_1 and ρ_2, it is easily found that $\rho_1+\rho_2 < 0$ and $\rho_1-\rho_2 < 0$. Therefore, suppose that

$$\begin{aligned}
\rho_1+\rho_2 &= -\mu_1^2 \\
\rho_1-\rho_2 &= -\mu_2^2
\end{aligned} \tag{2.7}$$

where μ_1 and μ_2 are positive numbers. Then, the displacement fields of the face sheet and the core can be obtained as follows;

$$\begin{aligned}
u^i(x^i,z^i) = e^{-\alpha x^i}\big[&k_1^iB^i\sin(\mu_1^i\alpha z^i) + k_1^iA^i\cos(\mu_1^i\alpha z^i) + k_2^iD^i\sin(\mu_2^i\alpha z^i) \\
&+ k_2^iC^i\cos(\mu_2^i\alpha z^i)\big]
\end{aligned} \tag{2.8}$$

$$w^i(x^i, z^i) = e^{-\alpha x^i}\left[A^i \sin(\mu_1^i \alpha z^i) + B^i \cos(\mu_1^i \alpha z^i) + C^i \sin(\mu_2^i \alpha z^i) + D^i \cos(\mu_2^i \alpha z^i)\right]$$

where

$$k_1^i = \frac{1 - 2s^i + 2\beta_2^i \mu_1^{i^2}}{\mu_1^i + 2\beta_3^i \mu_1^i}$$
$$k_2^i = \frac{1 - 2s^i + 2\beta_2^i \mu_2^{i^2}}{\mu_2^i + 2\beta_3^i \mu_2^i}.$$

The solutions given above are next subjected to traction and displacement continuity conditions at the interface between the top face sheet and the core;

$$\begin{gathered} u^t - u^c = 0 \\ w^t - w^c = 0 \\ \Delta f_{x^t} - \Delta f_{x^c} = 0 \\ \Delta f_{z^t} - \Delta f_{z^c} = 0 \\ \text{at} \quad z^t = -\frac{h^t}{2} \quad \text{and} \quad z^c = \frac{h^c}{2} \end{gathered} \tag{2.9}$$

and traction free boundary conditions at the outer surface of the top face sheet;

$$\begin{gathered} \Delta f_{x^t} = 0 \\ \Delta f_{z^t} = 0 \\ \text{at} \quad z^t = \frac{h^t}{2} \end{gathered} \tag{2.10}$$

where Δf_{x^i} and Δf_{z^i} are x and z components of traction, respectively. The traction components associated with Eq. (2.4) are

$$\Delta f_x = \left(\sigma_x' + \sigma_x^0 \frac{\partial u}{\partial x}\right)\kappa + \sigma_{xy}'\theta + \sigma_{xz}'\mu$$
$$\Delta f_y = \left(\sigma_{xy}' + \sigma_x^0 \frac{\partial v}{\partial x}\right)\kappa + \sigma_y'\theta + \sigma_{yz}'\mu$$
$$\Delta f_z = \left(\sigma_{xz}' + \sigma_x^0 \frac{\partial w}{\partial x}\right)\kappa + \sigma_{yz}'\theta + \sigma_z'\mu$$

accompanying the displacements u, v, and w, where κ, θ, and μ are the direction cosines of the normal to the undeformed boundary surface.

In addition to the above conditions, the displacement fields $u^c(x^c, z^c)$ and $w^c(x^c, z^c)$ may be subjected to restrictions placed on the deformation mode. In the transition from the uniformly strained state to the perturbed state, two deformation modes of the core are possible. The core can deform anti-symmetrically where the core displacements associated with the perturbation from the uniform straining are constrained to satisfy,

$$\begin{aligned} u^c(x^c, z^c) &= -u^c(x^c, -z^c) \\ w^c(x^c, z^c) &= w^c(x^c, -z^c) \end{aligned} \tag{2.11}$$

Or the core can deform in a symmetric deformation mode for which the core displacements satisfy,

$$\begin{aligned} u^c(x^c, z^c) &= u^c(x^c, -z^c) \\ w^c(x^c, z^c) &= -w^c(x^c, -z^c) \end{aligned} \tag{2.12}$$

Substitution of the displacement fields corresponding to different sets of boundary conditions into Eq. (2.9), Eq. (2.10), and Eq. (2.11) or Eq. (2.12) results in a system of eight linear algebraic homogeneous equations. Vanishing of the determinant associated with this system gives an equation implicit in ϵ of the form

$$f(\epsilon, \rho, \eta) = 0 \tag{2.13}$$

where ϵ ($\epsilon = \sigma/c^t_{55}$) is a normalized buckling stress and ρ ($\rho = ph^t/2$) and η ($\eta = rh^t/2$) are non-dimensional deformation factors. The solution of Eq. (2.13) for a specified ρ and η is the value of buckling stress, σ, associated with the transition to an adjacent state of equilibrium. Once this stress is found, the constants A^t, B^t,... etc. can be determined up to an arbitrary constant. This enables to characterize the buckling mode shapes associated with a given value of buckling stress. In the sections to follow, several cases with different geometrical and material properties will be discussed and compared against previous studies.

2.2.2 Finite element modeling

In order to support the theoretical finding, finite element (FE) computations were performed using the commercial software package ABAQUS. A comprehensive discussion of the ABAQUS FE formulation is given later in Chapter III. Eigenvalue buckling analyses are used to predict the buckling load and its associated buckling deformation mode. The face sheets and the core were modeled as linear elastic 2D continua. Eight-noded quadratic plane strain elements were used for both the face sheets and the core. A sufficiently fine mesh was used with over 3000 elements as shown in Fig. 2.2 resulting in characteristic element lengths that are very small compared to the wrinkling wavelength. Possible buckling modes, depending on geometrical and material parameters of the sandwich beam, observed from finite element analyses are illustrated in Fig. 2.3. The entire beam is uniformly strained from the left end, controlled by the axial displacement. The face sheet and the core are axially fixed at the other end in Fig. 2.3 (b), but the boundary condition in which the core is not subjected directly to the compressive loading is enforced to the structure shown in Fig. 2.3 (c).

2.3 Results and discussions

The buckling deformation modes of a sandwich panel in uniaxial compression loading depends on p and r. As discussed before, certain values of p and r that induce specific buckling behavior will be examined. The buckling modes to be considered here are divided into two categories; periodic and non-periodic modes.

$$p = 0 \quad and \quad r \neq 0 \quad \longrightarrow \quad periodic\ mode$$

$$p < 0 \quad and \quad r \neq 0 \quad \longrightarrow \quad non - periodic\ mode$$

Assumption of a periodic buckling mode has been commonplace in previous studies of the global and local buckling behavior. However, there exists the possibility that non-periodic buckling modes may render the lowest buckling stress.

2.3.1 Periodic buckling mode

If the real part of α is zero, Eq. (2.13) is reduced to

$$\hat{f}(\epsilon, \eta) = 0, \tag{2.14}$$

where ϵ is the normalized global buckling or wrinkling stress and η is the corresponding dimensionless wavelength. For the numerical evaluation of the results, the material properties used in the experiments of Fagerberg [19] have been chosen. The material properties are listed in Table 2.1 for the lamina in the facesheet and Table 2.2 for the cores. The stacking sequence of the face sheet is [0/90]s building a total thickness of 1mm. These material properties will be continuously used for future studies and comparisons.

In order to understand the full buckling behavior of the sandwich beam in a compressive load, the variation of the determinant equation, Eq. (2.14) with the critical stress, ϵ, is plotted in Figure 2.4, as a function of the wavelength. The full buckling behavior can be visualized if the determinant equation is obtained without making any assumptions about the deformation mode of the core. Since all three layers have to be considered here and each layer has 4 unknown constants in its displacement fields, 12 linear algebraic homogeneous equations are deduced from 4 traction free conditions at the outer surface of the top and the bottom face sheet, 4 displacement and 4 traction continuity conditions at the interface between the face sheets and the core.

In Figure 2.4, one solution can be found corresponding to a short wavelength,

and two other solutions corresponding to a moderate or large wavelength. The zero solution, however, is of no interest because it represents the pre-buckled initial equilibrium state of the beam. The buckling stress for the anti-symmetrical deformation mode is found to be always lower than that of the symmetrical one. Therefore, the first root other than zero in Figure 2.4 is the buckling stress corresponding to the anti-symmetrical deformation mode, and the second root corresponds to the symmetrical mode. It is interesting to note that when the wavelength is short, the two roots collapse to a single point. This aspect will be discussed later. As the wavelength becomes large, the double root becomes separated and the gap between the two roots becomes wider as shown. The buckling stress for the anti-symmetrical deformation mode decreases while the other stress increases in the large wavelength limit. For further analysis, it is convenient to decouple the deformation modes to observe the relationship between the buckling stress and its corresponding wavelength, and to compare the two deformation modes. In the following discussion, the symmetric and anti-symmetric deformation modes will be considered and treated separately.

The buckling stresses corresponding to the two deformation modes of the core are shown together in Figure 2.5. From Table 2.2, material properties corresponding to three cores (H30, H80, and H100) are chosen to capture the buckling behavior of the two deformation modes with respect to variation in the stiffness of the core. As discussed in Figure 2.4, the buckling stresses are the same regardless of the deformation modes in the regime of the short wavelength. Furthermore, it is now easily seen that the buckling stresses of the anti-symmetrical mode are always lower than that of the symmetrical mode. These characteristics of the buckling behavior were also shown in Figure 2.4.

Short wavelength buckling

As the length of the beam becomes shorter, sandwich structures tend to fail due to wrinkling. Since wrinkling initiates other failure mechanisms such as core shear failure or delamination between the face sheet and core, the wrinkling stress can be used as the compression strength of the sandwich beam. In the following section, the discussion will be focused on this local buckling behavior, or wrinkling. Results from the present analysis are compared with previous works by Fagerberg [19], Léotoing et al. [37], Niu and Talreja [43], and Plantema [45].

In the short wavelength regime, the critical buckling stress corresponding to each case in Figure 2.5 is found by computing the minimum value of ϵ, and the corresponding η is the associated critical non-dimensional wavelength. Figure 2.5 shows that the critical stress increases and its half wavelength decreases as the core gets stiffer. It is interesting to note that the minimum stress corresponding to the symmetrical deformation mode may coincide with the anti-symmetrical deformation mode, depending on the t_c/t_t ratio in Figure 2.6. If the core is very thick compared to the thickness of the face sheet, only the near regions of the face sheets will be affected due to the perturbation from the face sheets and the middle area remains undeformed. This results in little interaction between the top and bottom face sheet, so that the critical stress predicted by both deformation modes are identical in the short wavelength limit. This wrinkling stress, obtained from the case corresponding to a large value of t_c/t_t will be used for comparison of predicted wrinkling stresses with previous analyses, as will be discussed later. For a small value of t_c/t_t, as indicated in Figure 2.6, wrinkling is absent and the critical stress shows a continuous dependence on the buckling wave length, although, for $t_c/t_t = 10$, the minimum stress corresponding to the symmetric mode is very close to that of the anti-symmetric mode.

Comparison of different wrinkling studies

The present analysis is compared with previous results reported in the literature, in Figure 2.7. The plot shows the critical stresses corresponding to each analysis with various ratios of the Young's modulus of the core and the face sheet, corresponding to materials used in Fagerberg's experiment [19]. In Figure 2.7, the theoretical critical stresses and the FE predictions, except for the result by Léotoing et al. [38], show good agreement with the experimental result in a region of moderate modulus of the core. The values from Léotoing et al. analysis show a higher critical stress in all cases than the experimental results and other analytical predictions. The critical stresses from Niu and Talreja's analysis [43] are also close to the result of the present analysis. Plantema [45], Léotoing et al., and Niu and Talreja used the same technical beam theory for the face sheet, however, the modeling method for the core was different in each case, as mentioned before. Plantema used a exponential decay model for the vertical displacement of the core, and assumed the core thickness is much larger than that of the face sheet. Léotoing et al. developed a higher order elastic foundation theory for the core. Niu and Talreja modeled the core as a linear elastic medium like in the present analysis.

Even though the theoretical results agree very well with the experimental results in a certain region, there is a sudden change in the critical stress of the experimental results as the core is made stiffer. This is due to a transition in the failure mode from wrinkling to kink band failure of the axially loaded fiber in the face sheet [54]. According to Fagerberg [19], the observed failure mode of a sandwich beam with a core that has a moderate or high modulus is not affirmatively wrinkling or compression failure. Although the present analysis shows very good agreement the experimental result when the core is H80 (see Figure 2.7), the real failure mechanism

is too complicated to analyze through a model such as that discussed here. This might be caused by the co-existence of two deformation modes shown in Figure 2.5, leading to mode coupling, which warrants a post buckling analysis. Alternatively, a refined micromechanics based analysis of the face sheets may be needed to capture local face sheet instabilities. In the regime where the wrinkling occurs first, the present analysis reproduces the experimental result very closely, and is in close agreement with the FE prediction.

Evaluation of previous analysis

The previous analyses show similar buckling behavior with the present analysis in Figure 2.7. However, they exhibit different characteristics when the core gets stiffer. The analytical prediction of Niu and Talreja [43] is compared with the result from the present analysis in Figure 2.8. The results of FE analyses are also plotted in Figure 2.8 to verify the buckling mode and stress. Figure 2.8 shows the curves for the critical stress with respect to the ratio of the core modulus to the face sheet modulus. It is noted that the critical stress of the present analysis in Figure 2.8 is obtained based on the core carrying axial load because the stiffness of the core in the x–direction is of the same order of magnitude as that of the face sheet. FE predictions indicate that local buckling occurs first up to a certain ratio of the modulus between the face sheet and the core and, beyond that, global buckling becomes a dominant failure mode. The prediction of the present theoretical analysis reproduces this finding and is in very good agreement with the finite element prediction as shown in Figure 2.8, if the minimum stress is taken as the critical stress between the global and the local buckling stress.

The global buckling of Niu and Talreja [43] is discounted because the local buckling stress is always lower than the global buckling stress regardless of the modulus ratio.

The reason that the trend of their critical stress is different from that of the finite element analysis reported here is that the face sheet in their analysis is considered as an Euler-Bernoulli beam. This modeling method of the face sheet places a restriction on the prediction of the buckling of a sandwich beam with a thick face sheet. As the ratio of the core modulus to the face sheet modulus increases, the wrinkling wavelength decreases to the order of the thickness of the face sheet. This implies that Euler-Bernoulli beam theory is not appropriate in that wavelength regime. However, the critical stress predicted in [43] is lower than that of the present analysis and the finite element analysis as shown in Figure 2.8. This is because the core is assumed not to carry axial load. Figure 2.9 depicts the error incurred by this assumption, i.e., the difference between the critical loads when the core carries the applied axial load and when the core doesn't carry the applied axial load. The critical loads are obtained from the finite element computation. Thus, the results of Figure 2.9 can be used to demarcate those cases that warrant neglect of the core axial load carrying capability.

The present analysis and the FEA produce the same trend as shown Fig. 2.8, but the present analysis continually is lower than the FEA prediction. The deviation is perhaps caused by the FE implementation of the eigenvalue buckling problem. The commercial code ABAQUS uses the Jaumann rate of Cauchy stress in formulating the eigenvalue buckling problem. As pointed out in [5], this stress rate is not energetically conjugate to any finite strain measure. Consequently, this formulation can lead to results for buckling loads that are different than the values presented in this paper, where a different set of conjugate incremental stress and strain measures are used to formulate the buckling problem. The latter choice is a correct pair of energetically work–conjugate quantities. Bažant and Cedolin [9] have shown that the deficiency

associated with the Jaumann rate of Cauchy stress may be relieved by using the Jaumann rate of Kirhhoff stress, which is conjugate to the logarithmic strain measure associated with the Biezeno–Hencky formulation for the infinitesimal elastic stability problem. It is stressed again that if the incremental elastic moduli are to remain constant during the buckling deformation, then the Green–Lagrange strain and the second Piola–Kirhhoff stress must be used in the problem formulation. A detailed discussion regarding the fully 3D elastic stability problem is provided in [9].

Evaluation of previous analysis for an orthotropic sandwich beam

Predictions of the present analysis are now compared with FE predictions for a sandwich structure with orthotropic phases. H is defined as

$$H = \frac{h^t}{2h^t + h^c}, \tag{2.15}$$

and the length of the sandwich panel is $5h^t$, while the width of the panel is $10h^t$. Material properties for each case are described in Table 2.3 from Kardomateas [33], who used classical elasticity to investigate short wavelength periodic wrinkling of a sandwich panel. In that study, non-periodic deformation modes were not addressed. Results from [33] are compared against the present analysis and FE predictions in Fig. 2.10. Good agreement among the present analysis, the FEA results, and results from [33] are observed for all the cases except for Case 4 where H=0.01. In this case, as shown in Fig. 2.10, the disagreement among the analyses are as large as 30%.

2.3.2 Edge buckling

When it is assumed that the compressive uniaxial load on the sandwich beam is carried only by the face sheets, the FE predictions reveal that the buckling deformation is localized as shown in (c) of Figure 2.3. Goodier and Hsu [25] examined edge buckling by modeling the face sheets as an Euler beam and the core as an elastic

foundation. They showed that when the face sheets are sufficiently long and pinned at both ends, and the base of the elastic foundation is free to move, the deflection is localized at the ends and the edge buckling stress is much lower than the wrinkling stress. The elastic foundation on the "floating" base in their work is analogous to a core without axial load carrying capability. Since the face sheets carry practically most of the axial load applied to an entire sandwich structure having a low modulus core, this type of local failure should be considered carefully. In addition, experimental test conditions on compressed sandwich beams may involve boundary conditions that preclude the introduction of load into the core.

Sokolinsky and Frostig [49] studied boundary and loading condition effects on the deflection mode shape of a sandwich panel with a soft core using a closed-form high-order linearized buckling analysis. The face sheets were modeled as an Euler–Bernoulli beam and the core were modeled using the high–order theory. When the core is "soft", i.e., the core stiffness is much lower than the face sheet stiffness, the face sheet absorbs most of compressive loads applied to the sandwich structure and the buckling deformation is non-periodically localized as discussed before. They found various non-periodic deflection modes of the sandwich panel for specific loading and boundary conditions, while the core was assumed to carry no axial load.

The FE analysis is applied to verify non-periodic localized buckling modes as predicted by the generalized two-dimensional analysis presented in this paper and the results are shown schematically in Fig. 2.3, while quantitative comparisons are indicated in Fig. 2.11. The first case, Fig. 2.3 (c1), is a sandwich beam for which the face sheets are supported at their left edges resulting in null bending moment in the face sheets and the beam is compressed from the right side. In the second case, Fig. 2.3 (c2), the face sheets are simply supported at their left edges and the beam is

compressed from the right side. The load carrying capability of the core is eliminated in both cases. Figure 2.11 compares results of each case from the present analysis and FE analysis. The deformation modes are extracted from the middle surface of the top face sheet along the normalized longitudinal length of the sandwich beam. As shown in Fig. 2.11, the present analysis results show good agreement with the results of the FEA. For further discussion of the edge buckling results, the case corresponding to Fig. 2.3 (c1) is now considered.

Fig. 2.12 compares the edge buckling stress with the wrinkling stress calculated from the present analysis. The edge buckling stress can be predicted when the buckling deformation mode is assumed to be non-periodic. In the present analysis, the non-periodic buckling mode can be obtained if the real part of α in Equation Eq. (2.5) is less than zero. The assumption of a periodic buckling mode, which is commonly used in the sandwich beam buckling problem, results in the wrinkling stress in Figure 2.12. Material and geometrical properties of Fagerberg's beam were again used for the numerical evaluation. Fig. 2.12 clearly shows that the edge buckling stress is much lower than the wrinkling stress, and the modeling of the buckling deformation mode should be reconsidered when the core cannot sustain an applicable axial load. As seen from the results in Fig. 2.12, it is important to understand how the sandwich structure is loaded in order to establish whether the core carries any of the applied load. Fig. 2.13 shows the dominant buckling behavior when different assumptions on the deformation mode is made for a wider region of E^c/E^t ratios. The geometry of the sandwich beam is identical to those in the experiment of [19]. The face sheet and the core are modeled as isotropic materials. In the small E^c/E^t ratio regime, periodic and non-periodic deformation modes result in the same buckling behavior. As the core is made stiffer, edge buckling begins to dominate. The wrinkling stress is

higher than the edge buckling stress in this regime because the core begins to carry an appreciable amount of the axial load. Therefore, when a sandwich structure is designed for the face sheet to carry most of the applied load corresponding to a specific support and loading condition, the assumption of a periodic buckling deformation mode may mislead the critical load prediction, unless all possible buckling modes are considered simultaneously.

2.4 Conclusion

A two dimensional elasticity analysis for predicting general instabilities of a sandwich beam is presented. The face sheet and the core of the sandwich beam are modeled as 2D linear elastic orthotropic continua. The analysis investigates different types of buckling modes that are present in a compressed sandwich beam, including periodic and non-periodic deformation modes. When the core is unable to carry any significant axial load and is unconstrained from moving in the transverse direction, edge buckling prevails. In other situations, the anti-symmetrical wrinkling mode is found to yield the lowest buckling stress when the sandwich beam is sufficiently short. For longer beams, global Euler buckling is seen to prevail. The transition of the buckling mode depends on a number of factors, which include the face sheet to core thickness ratio and the ratio of core to face sheet stiffness, for a given length of beam. Predictions from finite element analyses have been used to support the analytical predictions.

Material Property	Value
E_1	107 GPa
E_2	15 GPa
G_{12}	4.3 GPa
ν_{12}	0.3
ν_{21}	0.043
t	0.25 mm

Table 2.1: Material properties of the lamina in the face sheets

Core	Young's Modulus(MPa)	Shear Modulus(MPa)
H30	20	13
H45	40	18
H60	56	22
H80	80	31
H100	105	40
H130	140	52
H200	230	85

Table 2.2: Material properties of the core material

Case 1	$E^c/E^t = 0.001$, $\nu^t = 0.35$, $\nu^c = 0$	
Case 2	$E^c/E^t = 0.002$, $\nu^t = 0.35$, $\nu^c = 0$	
Case 3	$E_1^t = 40$, $E_2^t = E_3^t = 10$ $G_{23}^t = 3.5$, $G_{12}^t = G_3^t 1 = 4.5$ $\nu_{12}^t = 0.26$, $\nu_{23}^t = 0.40$, $\nu_{31}^t = 0.065$	$E^c = 0.075$ $\nu^c = 0.30$
Case 4	$E_1^t = 181$, $E_2^t = E_3^t = 10.3$ $G_{23}^t = 5.96$, $G_{12}^t = G_{31}^t = 7.17$ $\nu_{12}^t = 0.28$, $\nu_{23}^t = 0.49$, $\nu_{31}^t = 0.0159$	$E_1^c = E_2^c = 0.032$, $E_3^c = 0.390$ $G_{23}^c = G_{31}^c = 0.048$, $G_{12}^c = 0.013$ $\nu_{31}^c = \nu_{32}^c = \nu_{21}^c = 0.25$

Table 2.3: Geometric and material parameters used in Fig. 2.10 (moduli unit: GPa)

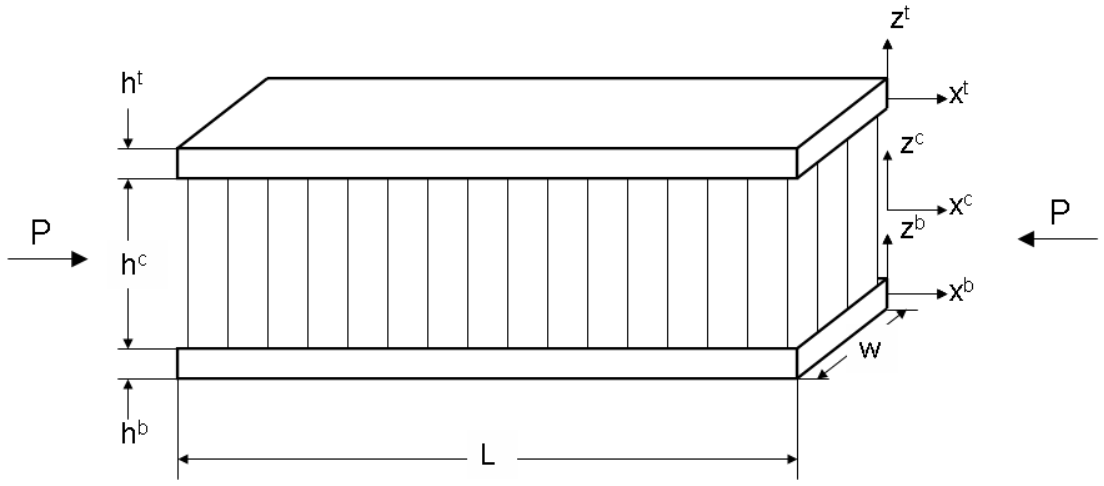

Figure 2.1: Configuration of a sandwich panel

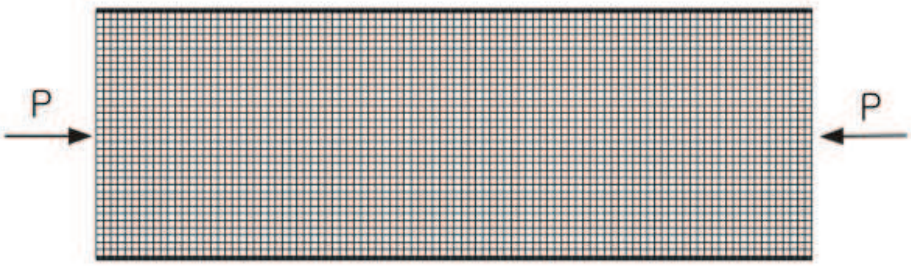

Figure 2.2: Finite element model of the sandwich beam

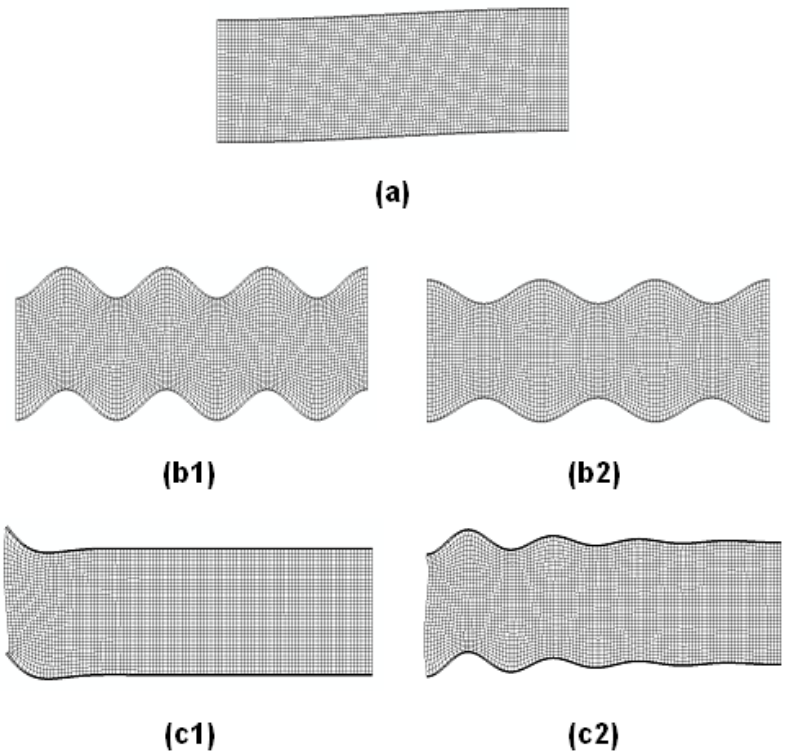

Figure 2.3: Buckling modes from finite element analysis: (a) Global buckling; (b) Anti-symmetrical and symmetrical wrinkling; (c) Edge buckling

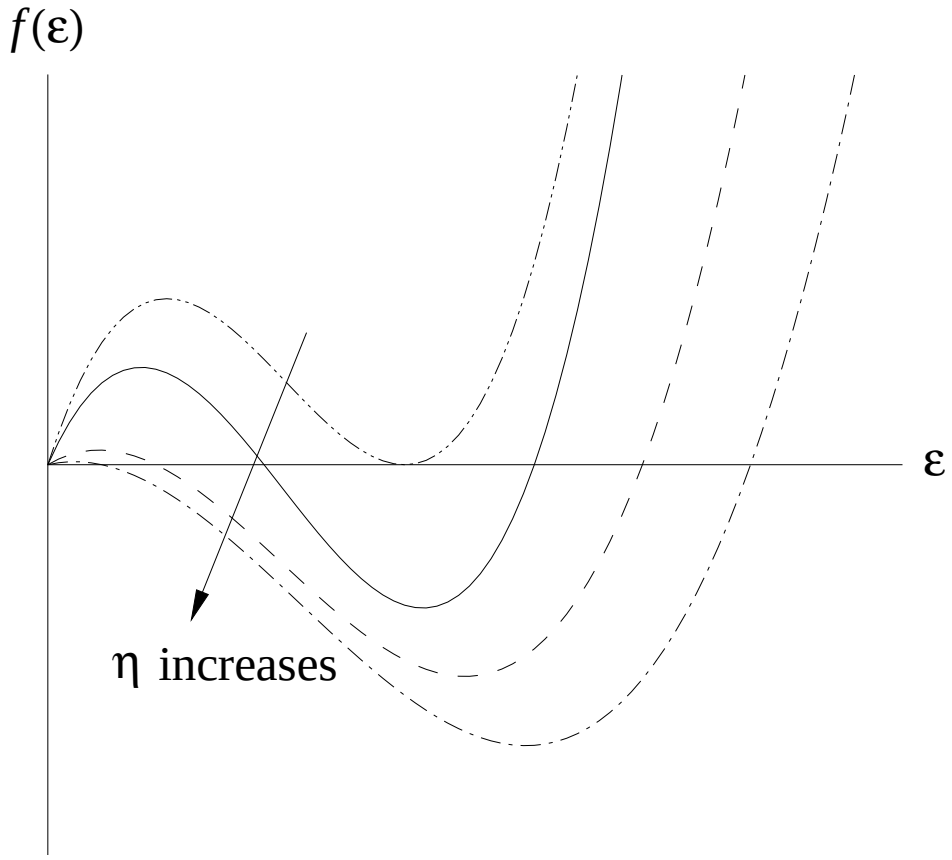

Figure 2.4: Variation of the determinant with non-dimensional buckling stress for the full deformation mode of the core

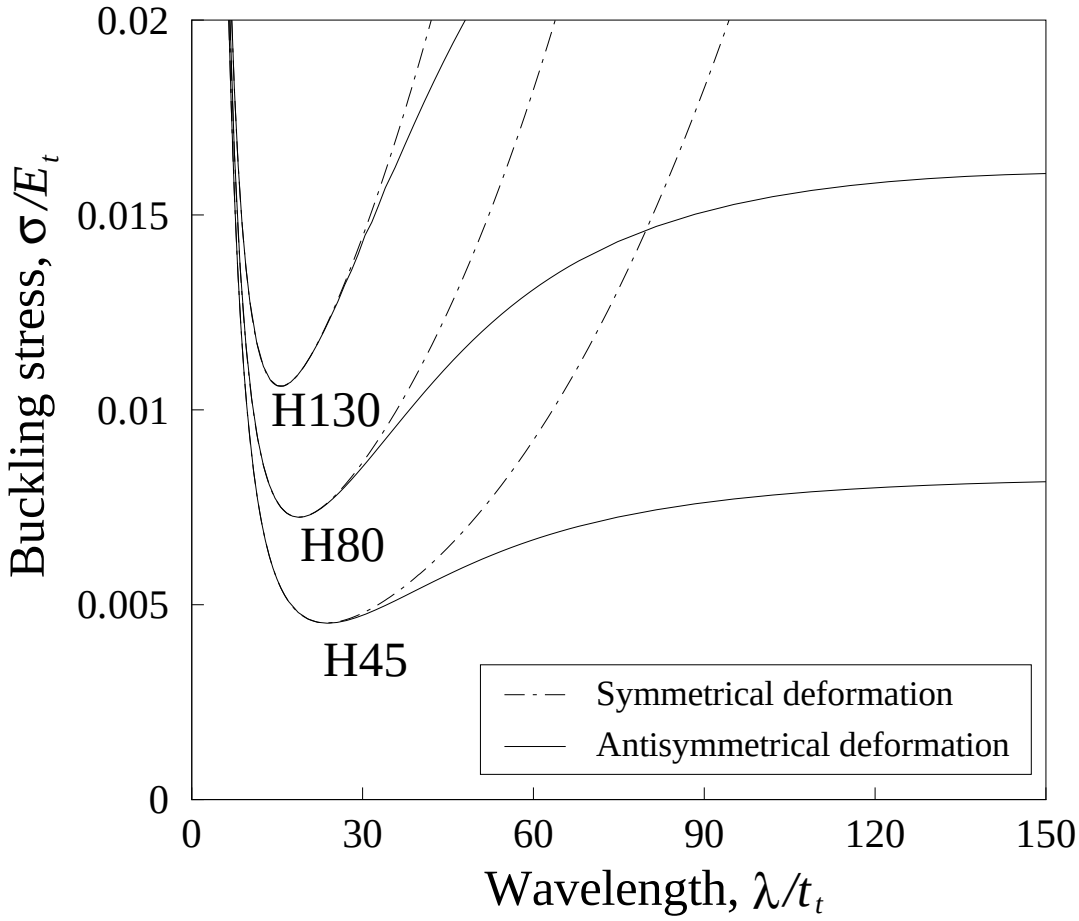

Figure 2.5: Variation of the critical stress with the non-dimensional half wavelength of two deformation modes of the core

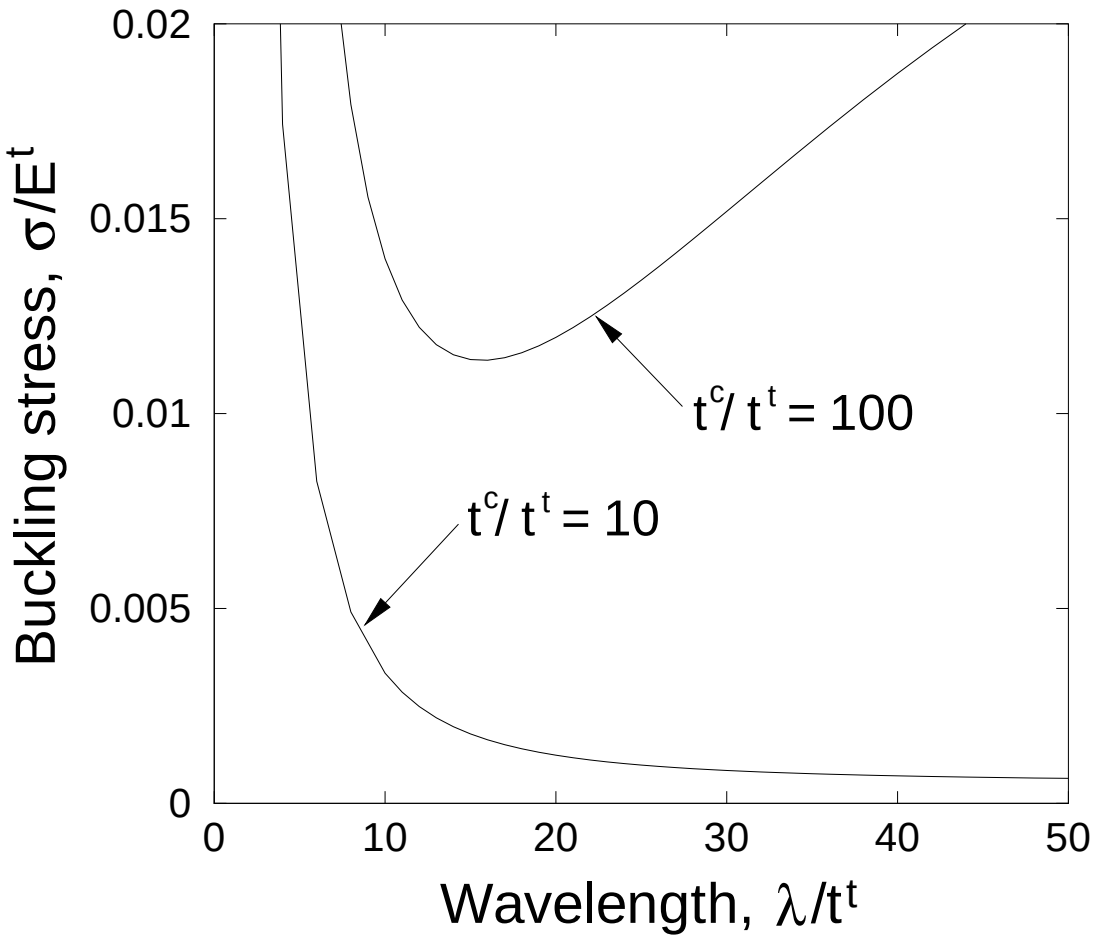

Figure 2.6: Variation of the buckling stress with nondimensional half wavelength of different thickness ratios

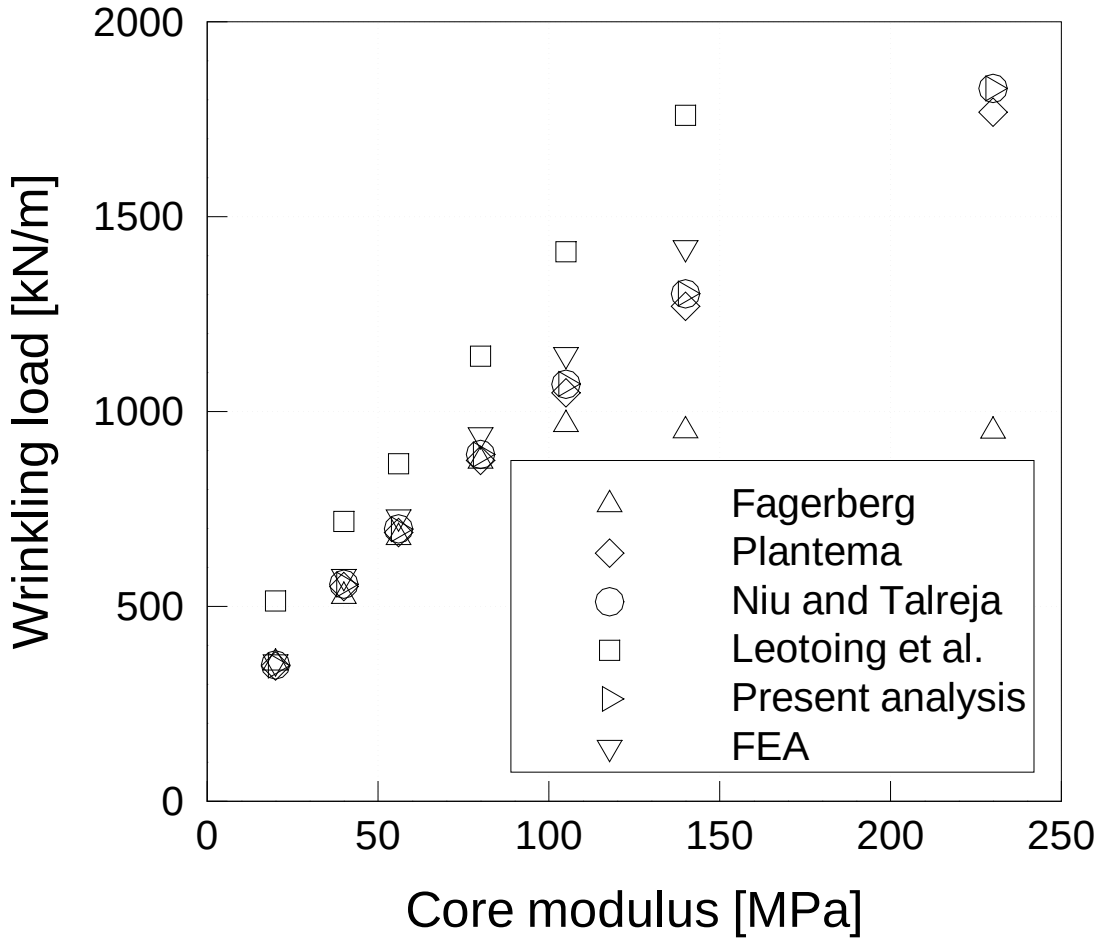

Figure 2.7: Comparison of the present analysis against previous analytical and experimental works

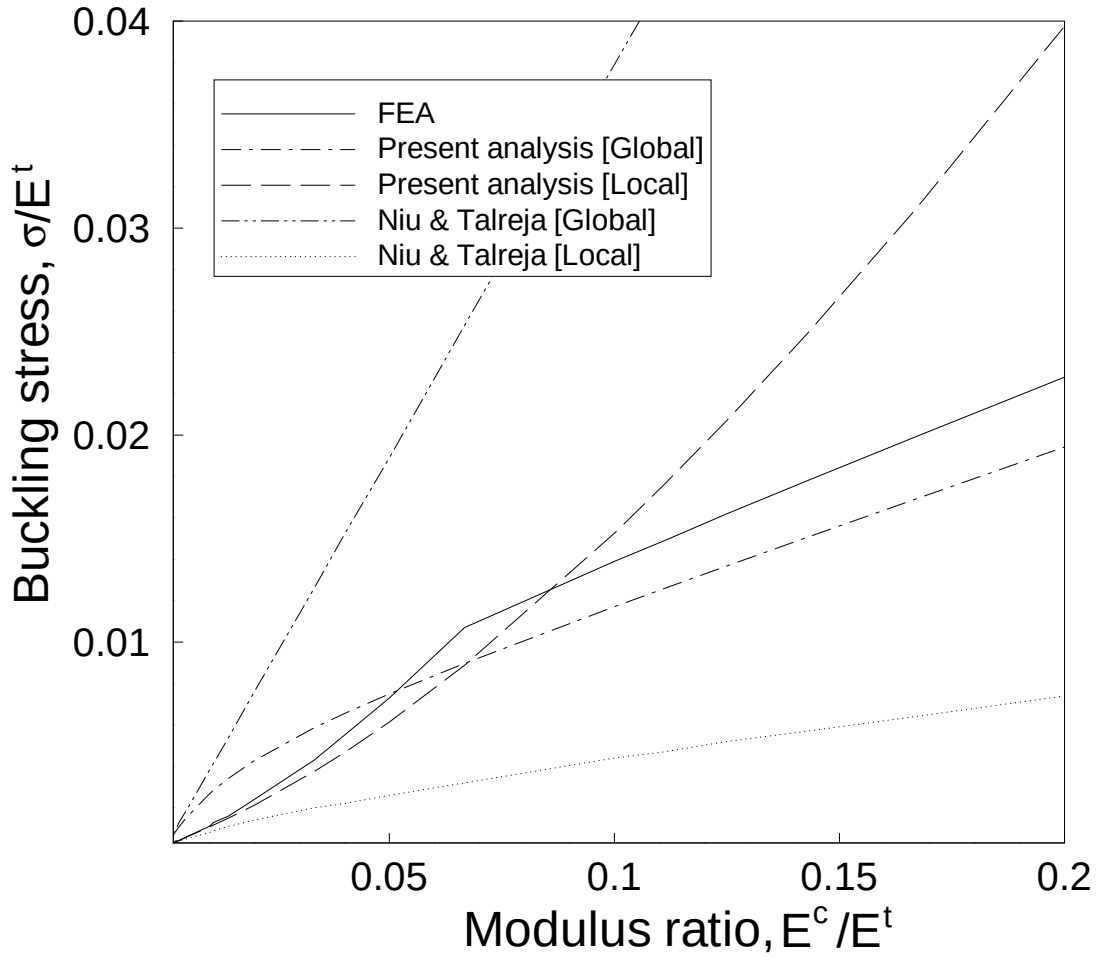

Figure 2.8: Comparison of the present analysis against Niu and Talreja and FEA for the periodic buckling mode

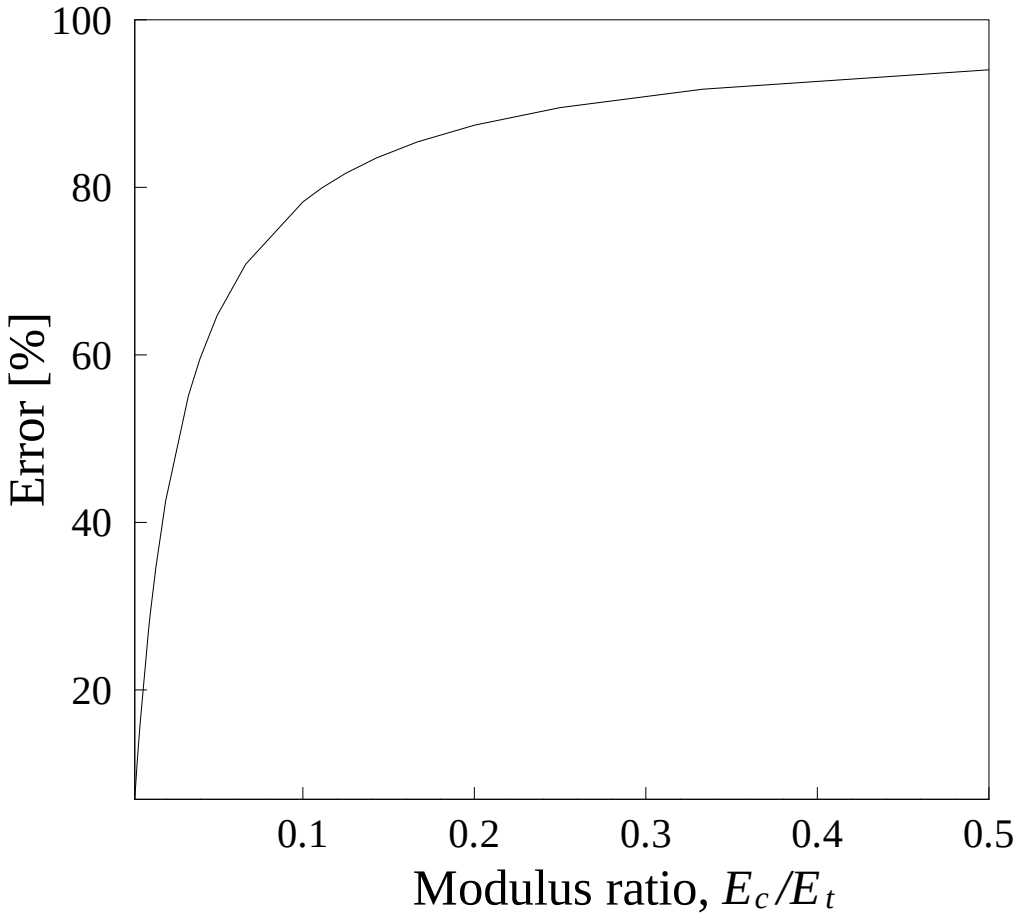

Figure 2.9: The error between the critical loads when the core is assumed to carry axial load and when it is not

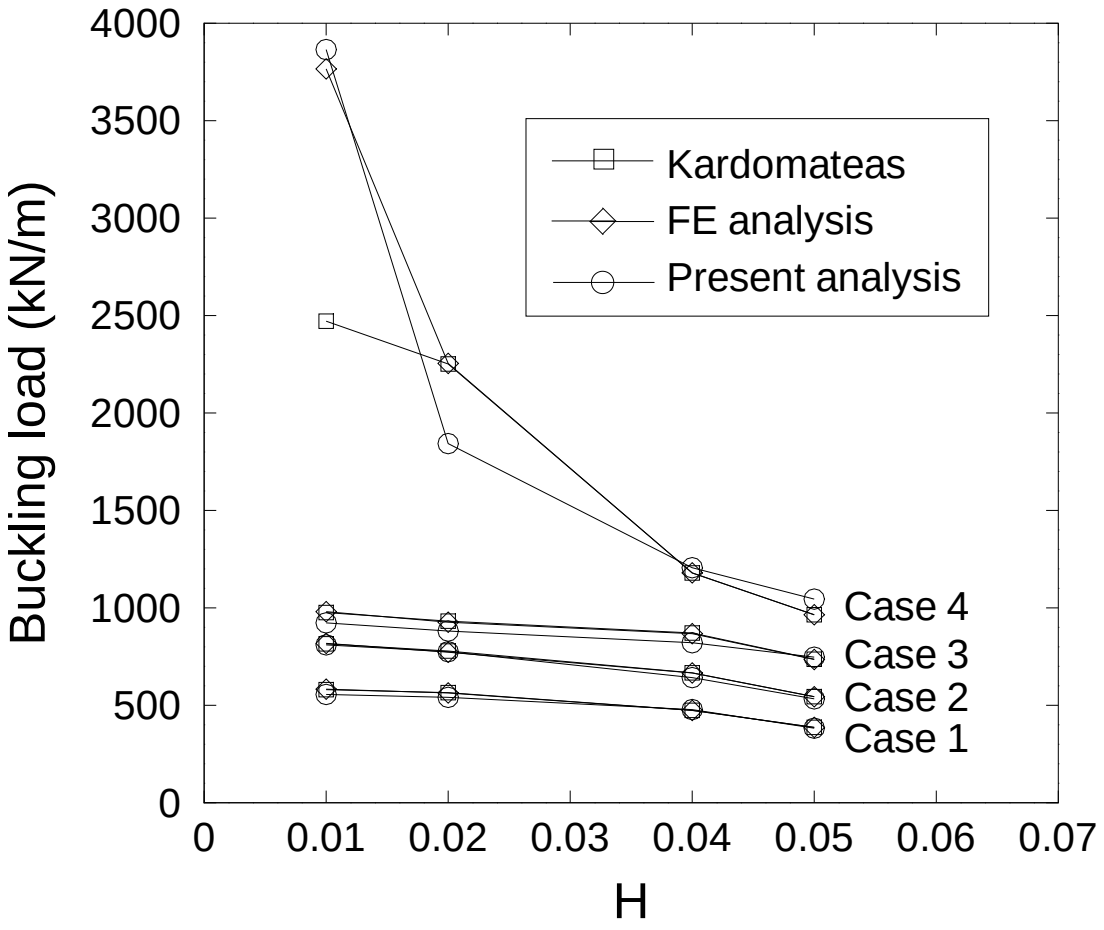

Figure 2.10: Comparison of the present analysis against Kardomateas predictions for the orthotropic sandwich panel

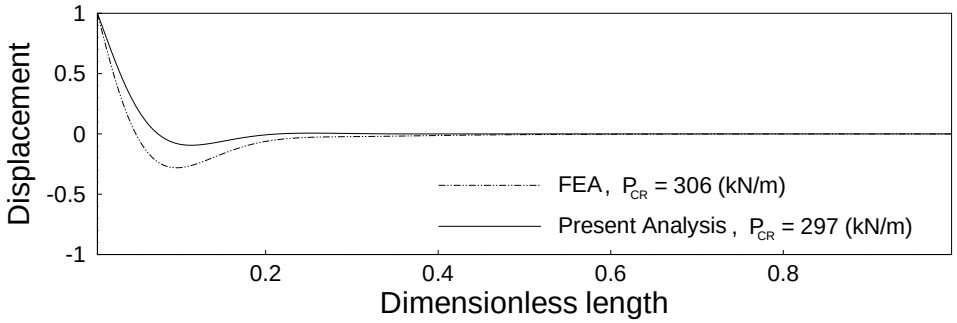

(a) Fig. 2.3 (c1)

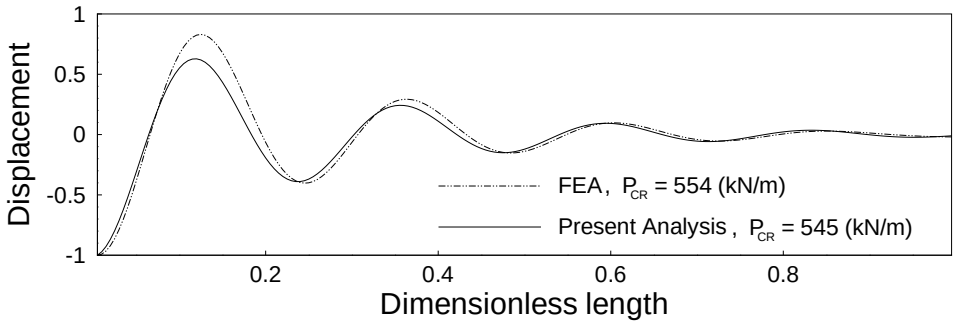

(b) Fig. 2.3 (c2)

Figure 2.11: Comparison of edge buckling deformation modes obtained along the central surface of the top face sheet

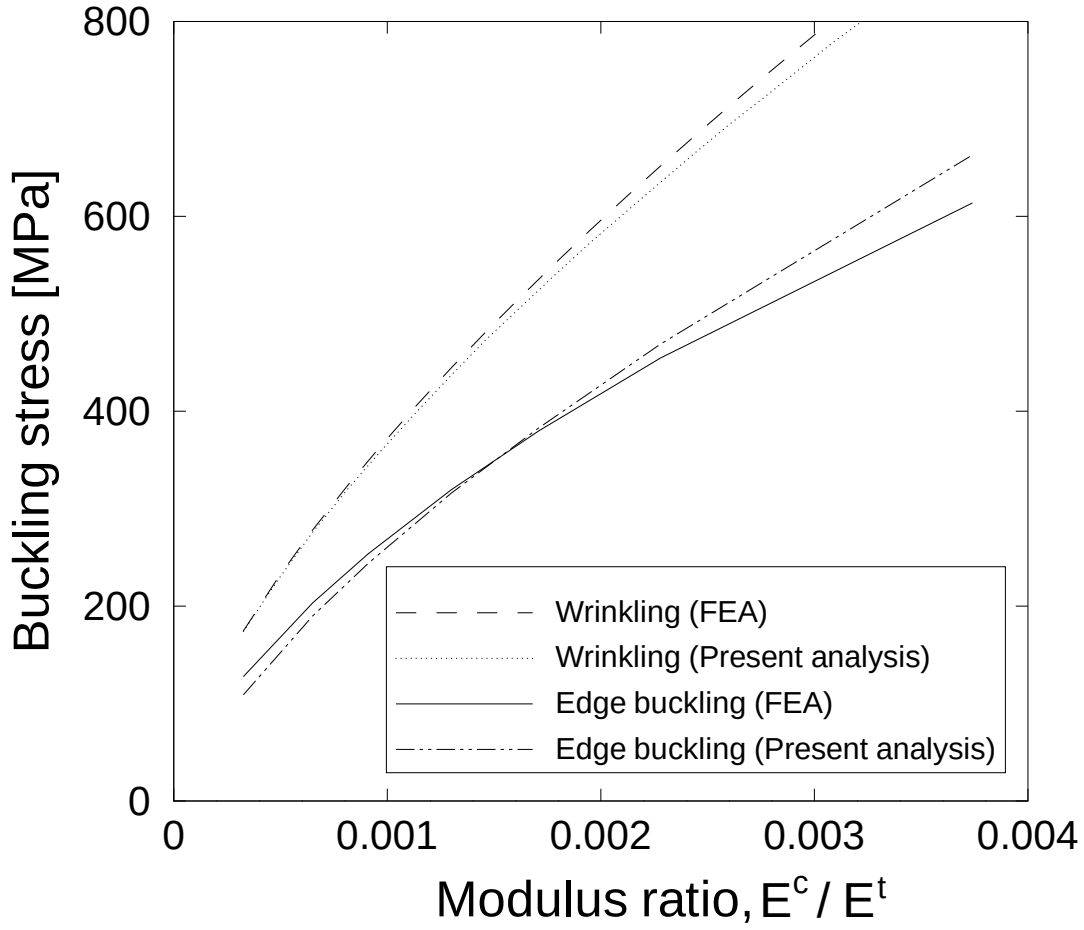

Figure 2.12: Comparison of edge buckling stress and wrinkling stress

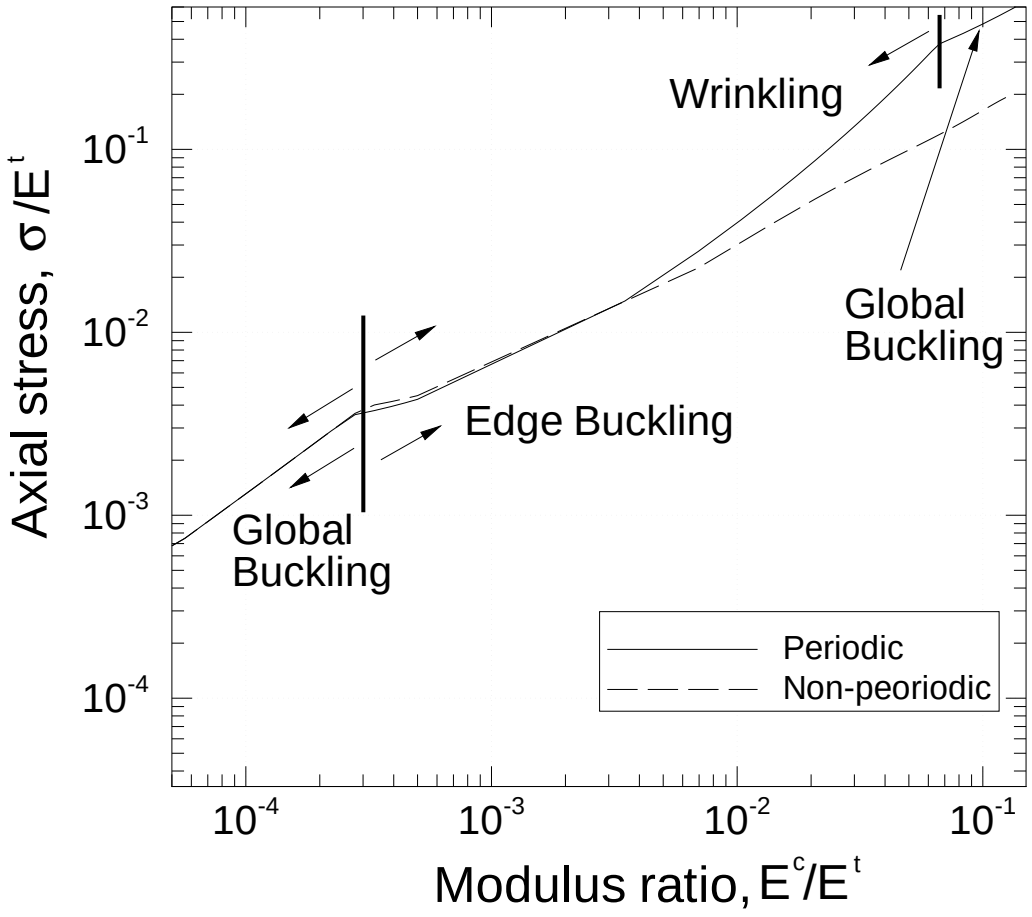

Figure 2.13: Predictions of buckling behavior according to the deformation mode assumption with the modulus ratio

CHAPTER III

Correct formulation for the static buckling analysis of a sandwich beam[1]

3.1 Introduction

The global and local instability problem of a sandwich beam subjected to axial compression has been widely studied theoretically and experimentally in the past decades. There are many useful theoretical models for predicting the global and local buckling of a sandwich beam structure. Early analytical models were developed using specific sets of assumptions for the face sheet and the core [1, 22, 25, 37, 43, 45]. The face sheet has typically been treated as an Euler–Bernoulli beam or a Timoshenko beam. The core has been modeled in a multitude of ways, some of which are a non–linear spring on an elastic foundation, an elastic continuum and so on. In order to ascertain the conditions under which the different sets of assumptions are valid, it is prudent to examine the sandwich beam buckling problem in a general setting. To this end, the sandwich beam buckling problem, under uniaxial loading is re–examined in a plane strain setting, where each constituent is treated within the framework of classical two–dimensional (2D) elasticity.

There are different mathematical formulations in the literature describing the infinitesimal elastic stability of a solid or with and without initial stress. Bažant [5]

[1]This chapter is currently being prepared as a journal paper.

consolidated the different mathematical formulations by proposing a unified general treatment of the infinitesimal elastic stability problem. He showed that when a certain finite strain measure is selected to describe the incremental deformation, its conjugate incremental stress and the corresponding constitutive model must be used in order to recover the same end result regardless of the choice of stress and strain measure. The conditions that are necessary for the equivalence between the different formulations was presented in [5]. In particular, the correct work–conjugate relations between the finite strain and the incremental stress, and the corresponding constitutive model should be consistently used throughout the problem solution phase.

Bažant and Beghini [6, 7] modeled a sandwich beam as a two constituent perfectly bonded solid with a thin face sheet, modeled as a Euler–Bernoulli beam, and a 2D linear elastic core. For a sandwich beam having a relatively soft core material compared to the face sheets, they showed the proper formulation that needed to be used in order to use a constant tangent modulus when the strains are small and the deformation is restrained to be in the linear elastic range. They showed that the formulation associated with the Green–Lagrange strain is suitable for this case.

In developing the presentation here, different formulations for the equilibrium equation governing the instability of a sandwich beam in uniaxial compression are discussed. Each constituent of the beam is treated as an orthotropic continuum in a general 2D plane strain setting. The predictions from the different formulations are compared against each other and also with previous theoretical predictions in order to assess the range of validity of the different solutions. In addition, a new set of finite element equations associated with the sandwich beam buckling problem is also derived.

3.2 Problem formulation

3.2.1 Theoretical study

The sandwich structure is illustrated in Fig. 3.1. A core of thickness h_c is bonded to and situated between a top and a bottom face sheet, with thickness of h_t and h_b, respectively. Perfect bonding is enforced at the common boundaries of the face sheets and the core. Sets of local cartesian coordinates are placed in each layer as shown in Fig. 3.1 with subscripts t, c, and b denoting the top face sheet, the core, and the bottom face sheet, respectively. This nomenclature is preserved throughout this presentation. u, v, and w with subscripts t, c, and b denote displacements of the top face sheet, the core, and the bottom face sheet, respectively, in the x, y, and z directions, respectively. The sandwich beam is subjected to a plane strain deformation in the xz–plane, by the application of a compressive load in the x–direction through smooth rigid end platens that are parallel to the z–axis and move in the x–direction.

When a solid body is considered in a slightly disturbed state from an initial strained state, the general equations governing the incremental stresses arising due to the perturbation from the initial state are [5],

$$\begin{aligned} \frac{\partial \sigma^*_{xx}}{\partial x} + \frac{\partial \sigma^*_{xy}}{\partial y} + \frac{\partial \sigma^*_{xz}}{\partial z} &= 0 \\ \frac{\partial \sigma^*_{xy}}{\partial x} + \frac{\partial \sigma^*_{yy}}{\partial y} + \frac{\partial \sigma^*_{yz}}{\partial z} &= 0 \\ \frac{\partial \sigma^*_{xz}}{\partial x} + \frac{\partial \sigma^*_{yz}}{\partial y} + \frac{\partial \sigma^*_{zz}}{\partial z} &= 0 \end{aligned} \tag{3.1}$$

where

$$\sigma^*_{ij} = \sigma^{\prime(m)}_{ij} + \sigma^0_{kj} u_{i,k} - \left(1 - \frac{m}{2}\right)\left(\sigma^0_{ik} e_{kj} + \sigma^0_{jk} e_{ki}\right) \tag{3.2}$$

and $e_{ij} = 1/2(u_{i,j} + u_{j,i})$. A superscript '0' is used to identify quantities with the initial position of equilibrium while a superscript '$\prime$' denotes quantities arising due

to the disturbance. The superscript '(m)' indicates the particular pair of work–conjugate stress and strain measure that need to be used. Bažant [5] proposed a general unified formulation for the finite strain tensor $\epsilon_{ij}^{(m)}$ and the corresponding constitutive stiffness $C_{ijkl}^{(m)}$ tensor in the form of

$$\epsilon_{ij}^{(m)} = \epsilon_{ij} - \left(1 - \frac{m}{2}\right) e_{ki} e_{kj} \tag{3.3}$$

$$C_{ijkl}^{(m)} = C_{ijkl} + \frac{1}{4}(2 - m)\left(\sigma_{ik}^{0}\delta_{jl} + \sigma_{jk}^{0}\delta_{il} + \sigma_{il}^{0}\delta_{jk} + \sigma_{jl}^{0}\delta_{ik}\right) \tag{3.4}$$

where the value of m classifies the different formulations. For example, $m = 2$ yields the second order Green–Lagrange strain, ϵ_{ij}, while $m = 1$ corresponds to the Biot strain measure, [12]. When $m = 0$, the second order Biezeno–Hencky strain is obtained [11]. Since the stress and the strain measure must be energetically related to each other, the correct pair of incremental stress and incremental strain, and the corresponding constitutive model with the *same value of* m must be used throughout the problem solution phase after a particular choice of finite strain measure is decided upon [5, 9].

In this paper, four formulations of the sandwich problem are considered. The first two (Case 1 and Case 2) are approximations specialized to thin walled structures, while Case 3 and Case 4 correspond to different values of 'm' in a finite strain setting.

- Case 1: Formulation for thin-walled structures using the approximation of constant stiffness tensor, but incorrectly using, m=0 in Eq. (3.2) (instead of $m = 2$)
- Case 2: Formulation for thin-walled structures, where the strains are approximated by neglecting axial deformation compared to rotation and using $m = 0$ in Eq. (3.4)
- Case 3: Biezeno–Hencky formulation ($m = 0$)

- Case 4: Trefftz formulation ($m = 2$)

Case 1 and Case 2 may be regarded as special cases of $m = 0$ formulations. When the rotations are much larger than the axial deformations during buckling deformation of a thin-walled structure, the axial strain components e_{ij} are often ignored compared to the rotational effects ω_{ij}. For this case (Case 1 and Case 2), Eq. (3.2) is simplified to

$$\sigma^*_{ij} = \sigma^{(m)}_{ij} + \sigma^0_{kj}\omega_{ik} \tag{3.5}$$

Case 1 employs the constant modulus approximation which is not the correct corresponding constitutive model to Eq. (3.5) .The results of Case 1 will be compared against the results of Case 2 in order to examine the effect of the improper use of the $m = 0$ formulation. In Case 3, the Biezeno–Hencky formulation is employed to address the buckling problem of a thin–walled structure, without any simplifying approximations. The Trefftz formulation (Case 4) is designated as an assessment of other cases in various analytical discussions forthcoming.

Bažant and Beghini [7] showed that, for sandwich type structures, the Green–Lagrange strain measure must be used if the strains are small and the elastic moduli are kept constant. The differential field equations of Trefftz [52], are associated with the Green–Lagrange finite strain measure. To summarize, Table 3.1 shows the different approximation to the strain, incremental stress, and constitutive relations used in addressing the buckling problem of a sandwich beam.

The sandwich beam considered here is uniformly strained in the x–direction, resulting in zero initial stresses in Eq. (3.2), except $\sigma^0_{xx} = -\sigma$. The field equations governing the incremental stresses arising due to the perturbation from the uniformly strained state can be obtained by substitution of Eq. (3.2) into Eq. (3.1).

Then, for the different cases, the following equilibrium equations are obtained.

Case 1 and Case 2:

$$\begin{aligned} \frac{\partial \sigma'^{(0)}_{xx}}{\partial x} + \frac{\partial \sigma'^{(0)}_{xy}}{\partial y} + \frac{\partial \sigma'^{(0)}_{xz}}{\partial z} &= 0 \\ \frac{\partial \sigma'^{(0)}_{xy}}{\partial x} + \frac{\partial \sigma'^{(0)}_{yy}}{\partial y} + \frac{\partial \sigma'^{(0)}_{yz}}{\partial z} &= 0 \\ \frac{\partial}{\partial x}\left[\sigma'^{(0)}_{xz} - \omega'_y \sigma^0_{xx}\right] + \frac{\partial \sigma'^{(0)}_{yz}}{\partial y} + \frac{\partial \sigma'^{(0)}_{zz}}{\partial z} &= 0 \end{aligned} \tag{3.6}$$

Case 3:

$$\begin{aligned} \frac{\partial}{\partial x}\left[\sigma'^{(0)}_{xx} - \sigma^0_{xx}\frac{\partial u}{\partial x}\right] + \frac{\partial}{\partial y}\left[\sigma'^{(0)}_{xy} - \sigma^0_{xx} e_{xy}\right] + \frac{\partial}{\partial z}\left[\sigma'^{(0)}_{xz} - \sigma^0_{xx} e_{xz}\right] &= 0 \\ \frac{\partial}{\partial x}\left[\sigma'^{(0)}_{xy} - \sigma^0_{xx}\omega'_z\right] + \frac{\partial \sigma'^{(0)}_{yy}}{\partial y} + \frac{\partial \sigma'^{(0)}_{zy}}{\partial z} &= 0 \\ \frac{\partial}{\partial x}\left[\sigma'^{(0)}_{xz} - \omega'_y \sigma^0_{xx}\right] + \frac{\partial \sigma'^{(0)}_{yz}}{\partial y} + \frac{\partial \sigma'^{(0)}_{zz}}{\partial z} &= 0 \end{aligned} \tag{3.7}$$

Case 4:

$$\begin{aligned} \frac{\partial}{\partial x}\left[\sigma'^{(2)}_{xx} + \sigma^0_{xx}\frac{\partial u}{\partial x}\right] + \frac{\partial \sigma'^{(2)}_{xy}}{\partial y} + \frac{\partial \sigma'^{(2)}_{xz}}{\partial z} &= 0 \\ \frac{\partial}{\partial y}\left[\sigma'^{(2)}_{xy} + \sigma^0_{xx}\frac{\partial v}{\partial x}\right] + \frac{\partial \sigma'^{(2)}_{yy}}{\partial y} + \frac{\partial \sigma'^{(2)}_{zy}}{\partial z} &= 0 \\ \frac{\partial}{\partial x}\left[\sigma'^{(2)}_{xz} + \sigma^0_{xx}\frac{\partial w}{\partial x}\right] + \frac{\partial \sigma'^{(2)}_{yz}}{\partial y} + \frac{\partial \sigma'^{(2)}_{zz}}{\partial z} &= 0 \end{aligned} \tag{3.8}$$

Application of the appropriate constitutive models, Eq. (3.4), to each case yields the governing equations for each case expressed in terms of displacements;

Case 1:

$$\begin{aligned} (\lambda_i + 2G_i)\frac{\partial^2 u_i}{\partial x_i^2} + G_i\frac{\partial^2 u_i}{\partial z_i^2} + (\lambda_i + G_i)\frac{\partial^2 w_i}{\partial x_i \partial z_i} &= 0 \\ (\lambda_i + 2G_i)\frac{\partial^2 w_i}{\partial z_i^2} + \left(G_i - \frac{\sigma_i}{2}\right)\frac{\partial^2 w_i}{\partial x_i^2} + \left(\lambda_i + G_i + \frac{\sigma_i}{2}\right)\frac{\partial^2 u_i}{\partial x_i \partial z_i} &= 0 \end{aligned} \tag{3.9}$$

Case 2:

$$\begin{aligned} (\lambda_i + 2G_i - 2\sigma_i)\frac{\partial^2 u}{\partial x^2} + \left(G_i - \frac{\sigma_i}{2}\right)\frac{\partial^2 u}{\partial z^2} + \left(\lambda_i + G_i - \frac{\sigma}{2}\right)\frac{\partial^2 w}{\partial x \partial z} &= 0 \\ (\lambda_i + 2G_i)\frac{\partial^2 w}{\partial z^2} + (G_i - \sigma_i)\frac{\partial^2 w}{\partial x^2} + (\lambda_i + G_i)\frac{\partial^2 u}{\partial x \partial z} &= 0 \end{aligned} \tag{3.10}$$

Case 3 and Case 4:

$$
\begin{aligned}
(\lambda_i + 2G_i - \sigma_i)\,\frac{\partial^2 u}{\partial x^2} + G_i\frac{\partial^2 u}{\partial z^2} + (\lambda_i + G_i)\,\frac{\partial^2 w}{\partial x \partial z} &= 0 \\
(\lambda_i + 2G_i)\,\frac{\partial^2 w}{\partial z^2} + (G_i - \sigma_i)\,\frac{\partial^2 w}{\partial x^2} + (\lambda_i + G_i)\,\frac{\partial^2 u}{\partial x \partial z} &= 0
\end{aligned}
\tag{3.11}
$$

It is worthwhile noting that the final forms of the governing equations for Case 3 and Case 4 are the same. Bažant [5] has already shown that a problem described by one formulation (or by Eq. (3.2), Eq. (3.3), and Eq. (3.4), with a particular value of m) is mutually equivalent with another mathematical formulation. Therefore, it is no surprise that Eq. (3.11) results for both Case 3 and Case 4.

The nontrivial solution to the governing equations for all the cases can be obtained by seeking the presence of nonuniform states of adjacent equilibrium of the uniformly strained sandwich. Here we exclude edge buckling and limit discussion to the case of periodic buckling in the x–direction. Then, the perturbed shape of each layer of the sandwich beam may be assumed as

$$
\begin{aligned}
u_i(x_i,\ z_i) &= \psi(z_i)\cos(\alpha x_i) \\
w_i(x_i,\ z_i) &= \phi(z_i)\sin(\alpha x_i)
\end{aligned}
\tag{3.12}
$$

Assuming that the sandwich beam is symmetrical, i.e., the top and the bottom face sheet have identical material and geometrical properties, only one half of the beam need to be considered in this analysis. Using (3.12) in Eq. (3.9) or Eq. (3.10) or Eq. (3.11) and solving for $\psi(y_i)$ and $\phi(y_i)$, the following solutions to the field equations are obtained for each case;

Case 1:

$$
\begin{aligned}
u_i(x_i,\ z_i) =& \big[B_i\sinh(\alpha z_i) + A_i\cosh(\alpha z_i) + k_i D_i\sinh(\mu_i\alpha z_i) \\
&+ k_i C_i\cosh(\mu_i\alpha z_i)\big]\cos(\alpha x_i) \\
w_i(x_i,\ z_i) =& \big[A_i\sinh(\alpha z_i) + B_i\cosh(\alpha z_i) + C_i\sinh(\mu_i\alpha z_i) \\
&+ D_i\cosh(\mu_i\alpha z_i)\big]\sin(\alpha x_i),
\end{aligned}
$$

where

$$k_i = \frac{\mu_i(1+2\beta_i)}{2-\mu_i^2+2\beta_i} \tag{3.13}$$

Case 2:

$$\begin{aligned} u_i(x_i,\ z_i) =& \big[k_1 B_i \sinh(\mu_1\alpha z_i) + k_1 A_i \cosh(\mu_1\alpha z_i) + k_2 D_i \sinh(\mu_2\alpha z_i) \\ &+ k_2 C_i \cosh(\mu_2\alpha z_i)\big] \cos(\alpha x_i) \\ w_i(x_i,\ z_i) =& \big[A_i \sinh(\mu_1\alpha z_i) + B_i \cosh(\mu_1\alpha z_i) + C_i \sinh(\mu_2\alpha z_i) \\ &+ D_i \cosh(\mu_2\alpha z_i)\big] \sin(\alpha x_i), \end{aligned} \tag{3.14}$$

where

$$\begin{aligned} \mu_1 &= \sqrt{\frac{2-3s_i}{2-s_i}} \\ \mu_2 &= \sqrt{\frac{1-s_i+\beta_i}{1+\beta_i}} \end{aligned} \tag{3.15}$$

$$\begin{aligned} k_1 &= \frac{2-3s_i-4(1+\beta_i)\mu_1^2}{(2+s_i+4\beta_i)\mu_1} \\ k_2 &= \frac{2-3s_i-4(1+\beta_i)\mu_2^2}{(2+s_i+4\beta_i)\mu_2} \end{aligned} \tag{3.16}$$

Case 3 and Case 4:

$$\begin{aligned} u_i(x_i,\ z_i) =& \big[k_1 B_i \sinh(\mu_1\alpha z_i) + k_1 A_i \cosh(\mu_1\alpha z_i) + k_2 D_i \sinh(\mu_2\alpha z_i) \\ &+ k_2 C_i \cosh(\mu_2\alpha z_i)\big] \cos(\alpha x_i) \\ w_i(x_i,\ z_i) =& \big[A_i \sinh(\mu_1\alpha z_i) + B_i \cosh(\mu_1\alpha z_i) + C_i \sinh(\mu_2\alpha z_i) \\ &+ D_i \cosh(\mu_2\alpha z_i)\big] \sin(\alpha x_i), \end{aligned} \tag{3.17}$$

where

$$\begin{aligned} \mu_1 &= \sqrt{\frac{2-3s_i}{2-s_i}} \\ \mu_2 &= \sqrt{\frac{1-s_i+\beta_i}{1+\beta_i}} \end{aligned} \tag{3.18}$$

$$k_1 = \frac{2 - 3s_i - 4(1+\beta_i)\mu_1^2}{(2 + s_i + 4\beta_i)\mu_1}$$
$$k_2 = \frac{2 - 3s_i - 4(1+\beta_i)\mu_2^2}{(2 + s_i + 4\beta_i)\mu_2} \tag{3.19}$$

For all cases, $\beta_i = \lambda_i/2G_i$, $\alpha = 2\pi/\lambda$ and λ =wavelength of the deformation mode. A_i, B_i, C_i, and D_i are arbitrary unknown constants associated with the above solutions.

In view of symmetry, the solutions obtained above are subject to traction and displacement continuity conditions at the interface of the top face sheet and the core, and traction free conditions at the external surface of the top face sheet. These equations are:

$$\begin{aligned} u_t - u_c &= 0 \\ w_t - w_c &= 0 \\ \Delta f_{x_t} - \Delta f_{x_c} &= 0 \\ \Delta f_{z_t} - \Delta f_{z_c} &= 0 \quad \text{at} \quad z_t = -h_t/2,\ z_c = h_c/2 \end{aligned} \tag{3.20}$$

$$\begin{aligned} \Delta f_{x_t} &= 0 \\ \Delta f_{z_t} &= 0 \quad \text{at} \quad z_t = h_t/2 \end{aligned} \tag{3.21}$$

In addition to the conditions, Eqs. (3.20) and (3.21), the displacement fields $u_c(x_c, z_c)$ and $w_c(x_c,\ z_c)$ are subjected to the restrictions to an antisymmetrical deformation or a symmetrical deformation.

Substitution of the displacement fields corresponding to different sets of boundary conditions in (3.20) and (3.21) results in a system of eight linear algebraic homogeneous equations for eight arbitrary unknown constants A_t, B_t, ...etc. for each of the cases and within each case for either symmetric or antisymmetric deformation. Vanishing of the determinant associated with this system gives an equation implicit

in ϵ of the form

$$f(\epsilon,\, \eta) = 0 \tag{3.22}$$

where ϵ ($\epsilon = \sigma/E_t$) is a normalized buckling stress and η ($\eta = \lambda/t_t$) is a non-dimensional half wavelength, where λ is the buckle wavelength. The solution of Eq. (3.22) for a specified η is the value of buckling stress associated with the transition to an adjacent state of equilibrium. Once this stress is found, the constants A_t, B_t,... etc. can be determined up to an arbitrary constant. This enables to characterize the buckle mode shapes associated with a given value of buckling stress. In the following sections, the theoretical predictions from different cases will be discussed and compared with each other.

3.2.2 Simplification of the differential equations

Before comparing the theoretical predictions for the buckling stress of a sandwich beam, Eq. (3.6), Eq. (3.7), and Eq. (3.8) are applied to a monolithic structure and simplified to the case of a slender beam. The differential field equations for a three-dimensional (3D) body under uniaxial compressive loading, Eq. (3.6), Eq. (3.7), and Eq. (3.8) can be reduced for the buckling problem of a one-dimensional (1D) column. The formulations of Case 1 and Case 4 will be discussed here for the simplification of the full equilibrium equations from a 3D solid to the Euler-Bernoulli Navier beam [14]. This discussion is intended to examine the differences in the formulations more clearly in a simple setting.

The problem considered here is a slender beam under uniaxial compression as shown in Fig. 3.2. Neglecting the effect of shear deformation, the kinematics of the

displacement fields are

$$U(x,\ z) = u(x) - z\frac{dw}{dz}$$
$$W(x,\ z) = w(x) \tag{3.23}$$

where U and W are the displacements of the beam in x and z directions, respectively, and u and w are the displacements of the centerline in x and z directions, respectively. The resultant forces of the beam are defined as

$$\int_A \sigma_{xx}\ dA = N_x$$
$$\int_A \sigma_{xz}\ dA = V_x \tag{3.24}$$
$$\int_A \sigma_{xx} z\ dA = M_x$$

where N_x=axial force, V_x=shear force, and M_x=moment due to the stress distribution. In addition to these definitions, a superscript '$\prime$' will be used to represent a perturbation quantity, and a superscript '0' designate the initial state. Similarly, a superscript '$*$' will be used for denoting quantities in the perturbed state.

The governing equation for the 1D beam proceeds by integration of the full differential equations and applying the kinematic relations. This procedure is followed for case 1, first. The first of Eq. (3.6) is associated with the axial force equilibrium. This equation is integrated over the cross-sectional area of the beam, to get,

$$\int_A \frac{\partial \sigma'_{xx}}{\partial x}\ dA + \int_A \frac{\partial \sigma'_{xy}}{\partial y}\ dA + \int_A \frac{\partial \sigma'_{xz}}{\partial z}\ dA = 0 \tag{3.25}$$

Using the integrated properties of the column over the cross-sectional area, as

$$\int_A dA = A, \quad \int_A z\ dA = 0, \quad \int_A z^2\ dA = I \tag{3.26}$$

where A=cross-sectional area and I=area moment of inertia, the equation for axial equilibrium is obtained as

$$\frac{dN'_x}{dx} = 0 \tag{3.27}$$

indicating that the perturbation to the axial force $N'_x = 0$. Since, $N^0_x = -P$=constant, where P is the applied end compression, the second of Eq. (3.6) is automatically satisfied under the restriction to a planar deformation state in the xz–plane. The third of Eq. (3.6), when integrated over the cross-sectional area of the beam, provides

$$\int_A \frac{\partial}{\partial x}\left[\sigma'_{xz} - \omega'_y \sigma^0_{xx}\right]\, dA + \int_A \frac{\partial \sigma'_{yz}}{\partial y}\, dA + \int_A \frac{\partial \sigma'_{zz}}{\partial z}\, dA = 0 \tag{3.28}$$

where

$$\omega'_y = \frac{1}{2}\left(\frac{\partial U'}{\partial z} - \frac{\partial W'}{\partial x}\right) \tag{3.29}$$

Using the kinematics of the beam, Eq. (3.23), Eq. (3.28) is rewritten in terms of the resultant forces,

$$\frac{dQ'_x}{dx} = 0 \tag{3.30}$$

where Q' is the shear force component of the column subjected to uniaxial load and can be written as

$$Q' = V'_x + N^0_x \frac{dw'}{dx} \tag{3.31}$$

The governing equation associated with moment equilibrium can be obtained by integrating the first equation over the cross-sectional area after multiplying by z throughout. Then,

$$\int_A \frac{\partial \sigma'_{xx}}{\partial x}\, z\, dA + \int_A \frac{\partial \sigma'_{xy}}{\partial y}\, z\, dA + \int_A \frac{\partial \sigma'_{xz}}{\partial z}\, z\, dA = 0 \tag{3.32}$$

This equation can be rewritten as,

$$\frac{\partial}{\partial x}\int_A \sigma'_{xx} z\, dA + \int_A \left[\frac{\partial (z\sigma'_{xz})}{\partial z} - \sigma'_{xz}\right]\, dA = 0 \tag{3.33}$$

or in terms of the resultant forces,

$$\frac{d^2 M'_x}{dx^2} + \frac{d}{dx}\left(N^0_x \frac{dw'}{dx}\right) = 0 \tag{3.34}$$

after differentiation with respect to x and using the shear force equilibrium relation, Eq. (3.30). The resultant moment in Eq. (3.34), can be written in terms of the displacement fields with the constitutive relation,

$$\begin{aligned} M'_x &= \int_A \sigma'_{xx} z \, dA \\ &= \int_A E^{(m)} \epsilon'_{xx} z \, dA \end{aligned} \tag{3.35}$$

where $E^{(m)}$=Young's modulus and ϵ'_{xx}=axial strain associated with the perturbation. The axial strain is expressed in the general form as

$$\epsilon'_{xx} = \frac{dU'}{dx} + \left(\frac{1}{2} - \alpha\right)\left(\frac{dU'}{dx}\right)^2 + \frac{1}{2}\left(\frac{dW'}{dx}\right)^2 \tag{3.36}$$

where $\alpha = 1 - m/2$ and m indicates the choice of the particular formulation. When the deformation is assumed to be very small, the second order perturbation quantities in Eq. (3.36) can be neglected compared to the first order quantities. Using the kinematic relations, Eq. (3.23), and Eq. (3.26), the resultant moment is expressed in terms of the transverse displacement field as,

$$M'_x = -E^{(m)} I \frac{d^2 w'}{dx^2} \tag{3.37}$$

Combining Eq. (3.34) and Eq. (3.37) results in the Euler-Bernoulli Navier beam equation, for the transverse buckling displacement,

$$E^{(m)} I \frac{d^4 w'}{dx^4} + P \frac{d^2 w'}{dx^2} = 0 \tag{3.38}$$

In a similar manner, the governing equation of equilibrium for a monolithic beam, corresponding to case 4 are,

$$\frac{dN^*_x}{dx} = 0 \tag{3.39}$$

$$\frac{d^2 M^*_x}{dx^2} + \frac{d}{dx}\left(N^0_x \frac{dw'}{dx}\right) = 0 \tag{3.40}$$

where

$$
\begin{aligned}
N_x^* &= N_x' + N_x^0 \frac{du'}{dx} \\
M_x^* &= \int_A \left(\sigma_{xx}' + \sigma_{xx}^0 \frac{\partial U'}{\partial x} \right) z \, dA = \int_A \sigma_{xx}^* z \, dA
\end{aligned} \tag{3.41}
$$

Note that the initial axial force effect appears in the axial force equilibrium equation and the moment equilibrium equation, which is not different than the case 1 formulation.

As before, the resultant moment can be expressed in terms of the displacement field as,

$$
\begin{aligned}
M_x^* &= \int_A \sigma_{xx}^* z \, dA \\
&= \int_A E^{(m)} \epsilon_{xx}^* z \, dA
\end{aligned} \tag{3.42}
$$

where $E^{(m)}$=Young's modulus. The axial strain ϵ_{xx}^* in the perturbed state can be written as

$$
\epsilon_{xx}^* = \frac{dU^*}{dx} + \left(\frac{1}{2} - \alpha \right) \left(\frac{dU^*}{dx} \right)^2 + \frac{1}{2} \left(\frac{dW^*}{dx} \right)^2 \tag{3.43}
$$

where $\alpha = 1 - m/2$. Since the displacement field in the current state $U^* = U_0 + U'$ and $W^* = W_0 + W'$, Eq. (3.43) can be rewritten as,

$$
\begin{aligned}
\epsilon_{xx}^* = & \frac{dU_0}{dx} + \left(\frac{1}{2} - \alpha \right) \left(\frac{dU_0}{dx} \right)^2 + \frac{1}{2} \left(\frac{dW_0}{dx} \right)^2 \\
& + \frac{dU'}{dx} + (1 - 2\alpha) \frac{dU_0}{dx} \frac{dU'}{dx} + \frac{dW_0}{dx} \frac{dW'}{dx} \\
& + \left(\frac{1}{2} - \alpha \right) \left(\frac{dU'}{dx} \right)^2 + \frac{1}{2} \left(\frac{dW'}{dx} \right)^2
\end{aligned} \tag{3.44}
$$

In addition to the approximation noted above, the out-of-plane displacement is regarded as zero in the initial flat state. Thus, Eq. (3.44) simplifies to,

$$
\epsilon_{xx}^* = \epsilon_{xx}^0 + \frac{dU'}{dx} \left[1 + (1 - 2\alpha) \frac{dU_0}{dx} \right] \tag{3.45}
$$

where

$$\epsilon^0_{xx} = \frac{dU_0}{dx} + \left(\frac{1}{2} - \alpha\right)\left(\frac{dU_0}{dx}\right)^2 + \frac{1}{2}\left(\frac{dW_0}{dx}\right)^2 \tag{3.46}$$

Using Eq. (3.23) and Eq. (3.26), the resultant moment is obtained in terms of the transverse displacement field as,

$$M^*_x = M^0_x - E^{(m)} I \frac{d^2 w'}{dx^2}\left[1 + (1-2\alpha)\frac{du_0}{dx}\right] \tag{3.47}$$

Since the rotation is also zero in the initial state, $M^0_x = 0$. Thus,

$$M^*_x = -E^{(m)} I \frac{d^2 w'}{dx^2}\left[1 + (1-2\alpha)\frac{du_0}{dx}\right] \tag{3.48}$$

Eq. (3.40) and Eq. (3.48) result in the general form of the governing equation for the Euler-Bernoulli beam subject to axial load, as

$$\frac{d^2}{dx^2}\left[E^{(m)} I \frac{d^2 w'}{dx^2}\left\{1 + (1-2\alpha)\frac{du_0}{dx}\right\}\right] + P\frac{d^2 w'}{dx^2} = 0 \tag{3.49}$$

In the initial flat state, the axial force is balanced by the applied force and the internal axial force may be written as,

$$N^0_x = E^{(m)} A \frac{du_0}{dx} \tag{3.50}$$

Therefore, since $N^0_x = \text{constant} = -P$, it follows that,

$$\frac{du_0}{dx} = -\frac{P}{E^{(m)} A} \tag{3.51}$$

Substitution of Eq. (3.51) into Eq. (3.49) yields

$$E^{(m)} I \frac{d^4 w'}{dx^4} + \frac{P}{1 - (1-2\alpha)P/E^{(m)}A}\frac{d^2 w'}{dx^2} = 0 \tag{3.52}$$

When the beam is simply supported and $m = 2$, for example, the critical buckling load is obtained from

$$\frac{P}{1 - P/(2EA)} = \frac{\pi^2 EI}{L^2} \tag{3.53}$$

which reduces to,

$$P_{cr} = \frac{P_E}{1 + \frac{\pi^2}{24}\left(\frac{t}{L}\right)^2} \tag{3.54}$$

where P_E=classical Euler buckling load for a simply-supported beam. Eq. (3.54) includes the effect of beam "compressibility", which is usually very small for a slender beam. As the beam slenderness increases, i.e., $t/L \to 0$, the critical buckling load converges to the classical Euler buckling load. Bažant and Cedolin [9] have derived the expression for a Timoshenko beam that corresponds to Eq. (3.54).

3.3 Results and discussions

3.3.1 Analytical models for the sandwich buckling load

Theoretical models predicting the global and the local instability of a sandwich beam under uniaxial compression has been developed. The results from different cases will be now compared with each other considering the effect of the conjugate relationship of the finite strain, the incremental stress, and the constitutive model. The material properties of Fagerberg [19] is adapted here for the numerical evaluation of the results. The same properties have been chosen for comparison of different cases. The material properties are listed in Table 3.2 for the lamina in the face sheet and Table 3.3 for the cores. The stacking sequence of the face sheet is [0/90]s, resulting in a total thickness of 1mm.

Ji and Waas [30] conducted a parametric study related to the instability of a sandwich beam. Various parameters such as the thickness ratio of the face sheet to the core and the ratio of moduli between face sheets and core were varied. Fig. 3.4 compares the results from various cases in the present study, producing inconsiderable differences between the different cases, for variation in the buckling stress as a function of wavelength. Fig. 3.5 shows the buckling stress variation with its corre-

sponding wavelength for all cases. The core properties are listed in Table 3.3. The core is assumed to undergo antisymmetrical deformation in these calculations. It is well known that the buckling stress profile of the antisymmetrical deformation of the core is more meaningful in predicting the global or local buckling of a sandwich beam in compression [29]. Therefore, only the antisymmetrical deformation mode of the core will be considered throughout this presentation. As can be seen in Fig. 3.5, the discrepancies between the different formulations appear to be insignificant overall. A distinction tends to develop when the wavelength becomes longer or the core becomes stiffer, yet the differences are small. Furthermore, the general shapes of the profile for all the cases resemble each other very closely.

In Fig. 3.6, the theoretical models presented here are compared with simplified buckling formula by Bažant and Beghini [8] and experimental results performed by Fleck and Sridhar [20]. Bažant and Beghini modeled a sandwich beam with face sheets as an Euler–Bernoulli Navier beam bonded to a 2D linear elastic core. They derived the critical buckling load with the $m = 2$ formulation. Finite element analysis was also performed and the results are shown in Fig. 3.6. The results between 2D elastic analyses are very close to each other regardless of the slenderness of the beam, and this may be caused by the very small thickness ratio between the face sheets and core (only 1/10 in experiments of [20]). However, the result from the simplified buckling formula by Bažant and Beghini is lower than the elastic solutions and the difference increases as the beam slenderness decreases. This is expected when the beam becomes thick because the face sheet is assumed to have no shear deformation in their analysis. In addition, the critical buckling load calculated by Bažant and Beghini is continuously lower than the experimental results, whereas the results from 2D elastic cases discussed in this chapter forms a lower bound bound for the

theoretical predictions.

Case 1 and Case 2 begin to depart from Case 3 and Case 4 when the core modulus becomes stiffer as illustrated in Fig. 3.7. Ji and Waas [30] revealed the transition of the instability mode from global buckling to wrinkling [30]. Although all the cases reproduce this alteration in the buckling modes at the same position, the disagreement between critical stresses among the cases grows as the core modulus increases. As shown in Fig. 3.5, the critical wavelength becomes shorter as the core becomes stiffer. When the wavelength becomes comparable with the characteristic beam thickness of the face sheet, the axial strains ϵ_{ij} cannot be ignored compared to the rotational components ω_{ij}. The critical stress of Case 1, which fails to use an appropriate constitutive model conjugate to the finite strain measure, differs more than the results of Case 2 from the predictions of Case 3 and Case 4.

3.3.2 Finite element analysis

Finite Element Analysis (FEA) is usually performed to simulate and validate the theoretical approach of determining the critical stress and its buckling behavior. The FEA results using the commercial software package ABAQUS are also illustrated in Fig. 3.7. It is interesting to note that the FE computations reproduce the results from Case 1 very closely. In the FEA, the face sheets and the core are modeled as linear elastic materials, equivalent to the two-dimensional elastic model presented here. The reason that the FEA results disagree with the buckling stress of Case 4 should be sought by closely examining the FE implementation of the eigenvalue buckling problem.

The general form of the equilibrium condition in the buckled state is expressed in

terms of the principle of virtual work, as

$$\int_V \Pi_{ij} \frac{\partial \delta v_i}{\partial X_j}\, dV = \int_S t_i \delta v_i\, dS + \int_V b_i \delta v_i\, dV \tag{3.55}$$

where Π_{ij}=nominal stress, δv_i=virtual velocity field, t_i=nominal traction on the boundary S of the initial state, b_i=body force per unit volume of the base state, and V=volume of the body in its reference configuration. The corresponding rate form of Eq. (3.55) is

$$\int_V \dot{\Pi}_{ij} \frac{\partial \delta v_i}{\partial X_j}\, dV = \int_S \dot{t}_i \delta v_i\, dS + \int_V \dot{b}_i \delta v_i\, dV \tag{3.56}$$

The left hand side of Eq. (3.56) can be expressed in terms of the Kirchhoff stress rate $\dot{\tau}$, so that Eq. (3.56) reduces to

$$\int_V \dot{\Pi}_{ij} \frac{\partial \delta v_i}{\partial X_j}\, dV = \int_V \dot{\tau}_{ij} \frac{\partial \delta v_i}{\partial x_j} - \left(\tau_{ik} \frac{\partial v_j}{\partial x_k} \right) \frac{\partial \delta v_i}{\partial x_j}\, dV \tag{3.57}$$

Eq. (3.57) is obtained from Eq. (3.56) using the relations

$$\begin{aligned} \Pi_{ij} &= \tau_{ik} \frac{\partial X_j}{\partial x_k} \\ \left(\frac{\partial \delta x_i}{\partial X_j} \right)^{\cdot} &= \frac{\partial \delta v_i}{\partial x_k} \frac{\partial x_k}{\partial X_j} \end{aligned} \tag{3.58}$$

Since the deformation is infinitesimal during the transition from the unbuckled to the buckled state, the Kirchhoff stress and its rate form can be approximated as

$$\begin{aligned} \tau_{ij} &= J\sigma_{ij} \simeq \sigma_{ij} \\ \dot{\tau}_{ij} &= J\dot{\sigma}_{ij} + \dot{J}\sigma_{ij} \simeq \dot{\sigma}_{ij} + v_{k,k}\sigma_{ij} \end{aligned} \tag{3.59}$$

where $J = 1 + u_{k,k}$ (Jacobian of the transformation).

As discussed earlier, if the elastic moduli are kept constant, the Green–Lagrange strain and its associated formulation, i.e., $m = 2$, should be used. Now, $\dot{\sigma}_{ij}$ can be rewritten using Truesdell's stress rate as,

$$\dot{\sigma}_{ij} = \hat{\sigma}_{ij} + \sigma_{kj} v_{i,k} + \sigma_{ki} v_{j,k} - \sigma_{ij} v_{k,k} \tag{3.60}$$

where the superscript '$\wedge$' denotes the stress rate. Note that Truesdell's stress rate has been chosen because it is work-conjugate to the Green–Lagrange strain measure. Substitution of Eq. (3.60) into Eq. (3.57) yields

$$\int_V \dot{\Pi}_{ij} \frac{\partial \delta v_i}{\partial X_j}\, dV = \int_V \hat{\sigma}_{ij} \delta v_{i,j}\, dV + \int_V \left(\sigma_{kj} v_{i,k} + \sigma_{ki} v_{j,k} - \sigma_{ik} v_{j,k}\right) \delta v_{i,j}\, dV \tag{3.61}$$

Using the symmetric properties of the stress, $\sigma_{ij} = \sigma_{ji}$, the above equation is simplified to

$$\int_V \dot{\Pi}_{ij} \frac{\partial \delta v_i}{\partial X_j}\, dV = \int_V \hat{\sigma}_{ij} \delta \dot{e}_{ij}\, dV + \int_V \sigma_{kj} v_{i,k} \delta v_{i,j}\, dV \tag{3.62}$$

where $\dot{e}_{ij} = (1/2)(v_{i,j} + v_{j,i})$, is the linearized small strain in terms of the velocity fields.

The rates of the surface traction t_i and the body force b_i in Eq. (3.56) can be expressed as

$$\begin{aligned} \dot{t}_i &= \frac{\partial t_i}{\partial F_{jk}} \dot{F}_{jk} \\ \dot{b}_i &= \frac{\partial b_i}{\partial F_{jk}} \dot{F}_{jk} \end{aligned} \tag{3.63}$$

since t_i and b_i are dependent on the change in geometry through F_{ij}, the latter being the deformation gradient. When the initial and the current configurations are assumed to be almost identical,

$$\begin{aligned} \frac{\partial t_i}{\partial F_{jk}} \dot{F}_{jk} &\simeq \frac{\partial t_i}{\partial F_{jk}} v_{j,k} \\ \frac{\partial b_i}{\partial F_{jk}} \dot{F}_{jk} &\simeq \frac{\partial b_i}{\partial F_{jk}} v_{j,k} \end{aligned} \tag{3.64}$$

Applying Eq. (3.62), Eq. (3.64), and the corresponding constitutive model for the Truesdell rate of the Cauchy stress,

$$\hat{\sigma}_{ij} = C_{ijkl}\, \dot{e}_{kl} \tag{3.65}$$

Eq. (3.56) now becomes,

$$\int_V \delta\dot{e}_{ij} C_{ijkl} \dot{e}_{kl}\, dV + \int_V \sigma_{kj} v_{i,k} \delta v_{i,j}\, dV - \int_S \delta v_i \frac{\partial t_i}{\partial F_{jk}} v_{j,k}\, dS - \int_V \delta v_i \frac{\partial b_i}{\partial F_{jk}} v_{j,k}\, dV = 0 \tag{3.66}$$

To formulate the eigenvalue buckling problem, the stress, the surface traction, and the body force in Eq. (3.66) are decomposed as initial and perturbed quantities, such that

$$\begin{aligned} \sigma_{ij} &= \sigma^0_{ij} + \lambda \sigma'_{ij} \\ t_i &= t^0_i + \lambda t'_i \\ b_i &= b^0_i + \lambda b'_i \end{aligned} \tag{3.67}$$

where λ is a constant multiplier to be determined. Substituting Eq. (3.67) into Eq. (3.66) and rearranging terms, the final equation for the buckling problem is obtained as,

$$\begin{aligned} &\int_V \delta\dot{e}_{ij} C_{ijkl} \dot{e}_{kl}\, dV + \int_V \sigma^0_{kj} v_{i,k} \delta v_{i,j}\, dV - \int_S \delta v_i \frac{\partial t^0_i}{\partial F_{jk}} v_{j,k}\, dS - \int_V \delta v_i \frac{\partial b^0_i}{\partial F_{jk}} v_{j,k}\, dV \\ &\quad - \lambda \Big[\int_V \sigma'_{kj} v_{i,k} \delta v_{i,j}\, dV - \int_S \delta v_i \frac{\partial t'_i}{\partial F_{jk}} v_{j,k}\, dS - \int_V \delta v_i \frac{\partial b'_i}{\partial F_{jk}} v_{j,k}\, dV \Big] = 0 \end{aligned} \tag{3.68}$$

When the velocity fields are discretized as

$$\mathbf{v} = \mathbf{N}\dot{\mathbf{q}} \tag{3.69}$$

with $\mathbf{N}$ being the assumed shape functions, each term of Eq. (3.68) is transformed into,

$$\int_V \delta\dot{e}_{ij} C_{ijkl} \dot{e}_{kl}\, dV = \delta\dot{\mathbf{q}}^{\mathrm{T}} \left[\int_V \mathbf{B}^{\mathrm{T}} \mathbf{C} \mathbf{B}\, dV \right] \dot{\mathbf{q}} \tag{3.70}$$

$$\int_V \sigma_{kj} v_{i,k} \delta v_{i,j}\, dV = \delta\dot{\mathbf{q}}^{\mathrm{T}} \left[\int_V \left(\frac{\partial \mathbf{N}}{\partial \mathbf{x}} \right)^{\mathrm{T}} \boldsymbol{\sigma}\, \frac{\partial \mathbf{N}}{\partial \mathbf{x}}\, dV \right] \dot{\mathbf{q}} \tag{3.71}$$

$$\int_S \delta v_i \frac{\partial t_i}{\partial F_{jk}} v_{j,k}\, dS = \delta\dot{\mathbf{q}}^{\mathrm{T}} \left[\int_S \mathbf{N}^{\mathrm{T}} \frac{\partial \mathbf{t}}{\partial \mathbf{q}}\, dS\right] \dot{\mathbf{q}} \tag{3.72}$$

$$\int_V \delta v_i \frac{\partial b_i}{\partial F_{jk}} v_{j,k}\, dS = \delta\dot{\mathbf{q}}^{\mathrm{T}} \left[\int_V \mathbf{N}^{\mathrm{T}} \frac{\partial \mathbf{b}}{\partial \mathbf{q}}\, dV\right] \dot{\mathbf{q}} \tag{3.73}$$

Here, $\mathbf{B}$ is the derivative of $\mathbf{N}$ with respect to $\mathbf{x}$. Thus, the FE formulation for the eigenvalue buckling problem reduces to,

$$\left[\mathbf{K}^0 + \lambda \mathbf{K}'\right] \dot{\mathbf{q}} = \mathbf{0} \tag{3.74}$$

where

$$\mathbf{K}^0 = \int_V \mathbf{B}^{\mathrm{T}}\mathbf{C}\mathbf{B}\, dV + \int_V \left(\frac{\partial \mathbf{N}}{\partial \mathbf{x}}\right)^{\mathrm{T}} \boldsymbol{\sigma}^{\mathbf{0}}\, \frac{\partial \mathbf{N}}{\partial \mathbf{x}}\, dV - \int_S \mathbf{N}^{\mathrm{T}} \frac{\partial \mathbf{t}^{\mathbf{0}}}{\partial \mathbf{q}}\, dS - \int_V \mathbf{N}^{\mathrm{T}} \frac{\partial \mathbf{b}^{\mathbf{0}}}{\partial \mathbf{q}}\, dV \tag{3.75}$$

$$\mathbf{K}' = \int_V \left(\frac{\partial \mathbf{N}}{\partial \mathbf{x}}\right)^{\mathrm{T}} \boldsymbol{\sigma}'\, \frac{\partial \mathbf{N}}{\partial \mathbf{x}}\, dV - \int_S \mathbf{N}^{\mathrm{T}} \frac{\partial \mathbf{t}'}{\partial \mathbf{q}}\, dS - \int_V \mathbf{N}^{\mathrm{T}} \frac{\partial \mathbf{b}'}{\partial \mathbf{q}}\, dV \tag{3.76}$$

The commercial code, ABAQUS, uses the Jaumann rate of Kirhhoff stress $\hat{\tau}_{ij}^{(J)}$ to fomulate the buckling problem. The relation between the Kirhhoff stress rate $\dot{\tau}_{ij}$ and $\hat{\tau}_{ij}^{(J)}$ is

$$\hat{\tau}_{ij}^{(J)} = \dot{\tau}_{ij} - \tau_{kj}\dot{\omega}_{ik} + \tau_{ik}\dot{\omega}_{kj} \tag{3.77}$$

where

$$\dot{\omega}_{ij} = \frac{1}{2}\left(\frac{\partial v_i}{\partial x_j} - \frac{\partial v_j}{\partial x_i}\right) \tag{3.78}$$

Therefore, the left hand side of Eq. (3.56) becomes,

$$\int_V \dot{\Pi}_{ij} \frac{\partial \delta v_i}{\partial X_j}\, dV = \int_V \hat{\tau}_{ij}^{(J)} \delta\dot{e}_{ij} + \tau_{ij}\left(\delta v_{i,k} v_{k,j} - 2\dot{e}_{ik}\delta\dot{e}_{kj}\right)\, dV \tag{3.79}$$

Now, with the right hand side of Eq. (3.56) and with Eq. (3.79), Eq. (3.56) is rewritten as

$$\int_V \hat{\tau}_{ij}^{(J)} \delta\dot{e}_{ij}\, dV + \int_V \tau_{ij}\left(\delta v_{i,k} v_{k,j} - 2\dot{e}_{ik}\delta\dot{e}_{kj}\right)\, dV - \int_S \frac{\partial t_i}{\partial F_{jk}} \dot{F}_{jk}\, dS - \int_V \frac{\partial b_i}{\partial F_{jk}} \dot{F}_{jk}\, dV = 0 \tag{3.80}$$

Following assumptions similar to before on the small perturbation, Eq. (3.80) becomes

(3.81)

$$\int_V \delta\dot{e}_{ij} C^{(J)}_{ijkl} \dot{e}_{kl}\, dV + \int_V \sigma_{ij} \left(\delta v_{i,k} v_{k,j} - 2\dot{e}_{ik}\delta\dot{e}_{kj}\right) dV - \int_S \frac{\partial t_i}{\partial F_{jk}} v_{j,k}\, dS - \int_V \frac{\partial b_i}{\partial F_{jk}} v_{j,k}\, dV = 0$$

where $C^{(J)}_{ijkl} = C^{(0)}_{ijkl} - \delta_{kl}\sigma_{ij}$ [5], which is the corresponding constitutive model for the Jaumann rate of the Cauchy stress. In fact, Eq. (3.81) is identical with Eq. (3.68), since a consistent problem formulation is independent of the choice of m.

As given in their theoretical manual, ABAQUS uses the $C^{(J)}_{ijkl} = C_{ijkl}$ for $C^{(J)}_{ijkl}$ appearing in the first term of Eq. (3.81), instead of $C^{(J)}_{ijkl} = C^{(0)}_{ijkl} - \delta_{kl}\sigma_{ij}$. Consequently, in the ABAQUS FE formulation, terms associated with the volume integral $\int_V \sigma^0_{ij}\dot{e}_{ik}\delta\dot{e}_{kj}\, dV$ and $\int_V \sigma'_{ij}\dot{e}_{ik}\delta\dot{e}_{kj}\, dV$ in $\mathbf{K}^0$ and $\mathbf{K}'$ of Eq. (3.74) are non-vanishing. These extra terms results in stiffer $\mathbf{K}^0$ and $\mathbf{K}'$ than the stiffness matrices in Eq. (3.74) when the body is in compression, and, consequently, causes the higher eigenbuckling loads as shown in Fig. 3.7. Since σ^0 and σ' of the core is not negligible for stiffer cores, the discrepancies in Fig. 3.7 becomes larger as the core stiffness becomes of the same order as the face sheet stiffness.

Fig. 3.8 shows the eigenbuckling load computed from Eq. (3.74) and Eq. (3.81) with $C^{(2)}_{ijkl}$ instead of $C^{(J)}_{ijkl}$. The only difference between Eq. (3.74) and Eq. (3.81) with $C^{(2)}_{ijkl}$ is the extra term $\int_V \sigma_{ij}\dot{e}_{ik}\delta\dot{e}_{kj}\, dV$. The buckling load obtained from ABAQUS and the present analysis in Chapter II are also shown to support the argument regarding the deficiency of the ABAQUS FE formulation. Fig. 3.8 clearly shows that FE formulation with the extra term overpredicts the buckling load since the extra term results in stiffer $\mathbf{K}$ matrix when the body is in compression. The discrepancy increases as the core becomes stiffer since the effect of σ in the extra term becomes significant for the stiff core material.

In addition to the extra terms, Bažant [5], has shown that the Jaumann rate of Cauchy stress is not energetically associated with any admissible finite strain measure. This deficiency results in the fact that the equilibrium equations expressed in terms of the Jaumann rate of Cauchy stress are not suitable for evaluating stability, unless the material is incompressible [5, 9]. The Jaumann rate of Cauchy stress can be regarded as a special case of the objective stress rate corresponding to the Biezeno–Hencky formulation, $m = 0$;

$$\hat{\sigma}_{ij}^{(0)} = \dot{\sigma}_{ij} - \sigma_{kj}\dot{\omega}_{ik} + \sigma_{ik}\dot{\omega}_{kj} + \sigma_{ij}v_{k,k} \tag{3.82}$$

without the last term $\sigma_{ij}v_{k,k}$. It seems that the Jaumann's stress rate considers the rotational deformation only, somewhat analogous to neglecting the axial strain compared to the rotational strain for thin-walled structures presented ealier in Case 1 and Case 2.

3.4 Conclusion

A two-dimensional linear elastic mechanical model for the exact solution to the sandwich column buckling problem is presented. In developing the elastic solution, the general equilibrium equations for the infinitesimal elastic stability of a solid are considered. It is shown that different mathematical formulations for the incremental deformation may be used, and they are mutually equivalent with each other if the proper work conjugate relations of finite strain and incremental stress, and the corresponding constitutive model is sustained. The analytical models developed from various formulations are compared against each other. It appears that the overall buckling behavior predicted by the theoretical models exhibits inconsiderable difference with the correct formulation for certain range of material and geometric properties. However, the discrepancies are likely to increase as the characteristic beam

length of the face sheet become comparable to the critical wavelength. The new theoretical model presented here should be used if an elastic solution needs verification with respect to simplifying assumptions. Corresponding FE formulation for the eigenvalue buckling problem is proposed considering the work-conjugate relationship when the strains are small and constant elastic moduli are used.

Case 1	Case 2	Case 3	Case 4
$\sigma^*_{ij} = \sigma'^{(0)}_{ij} - \sigma^0_{kj}\omega_{ik} + \sigma^0_{ik}\omega_{kj}$	$\sigma^*_{ij} = \sigma'^{(0)}_{ij} - \sigma^0_{kj}\omega_{ik} + \sigma^0_{ik}\omega_{kj}$	$\sigma^*_{ij} = \sigma'^{(0)}_{ij} + \sigma^0_{kj}u_{i,k} - \left(\sigma^0_{kj}e_{kj} + \sigma^0_{jk}e_{k,i}\right)$	$\sigma^*_{ij} = \sigma'^{(2)}_{ij} + \sigma^0_{kj}u_{i,k}$
$\epsilon^{(0)}_{ij} = \frac{1}{2}\left(u_{i,j} + u_{j,i}\right)$	$\epsilon^{(0)}_{ij} = \frac{1}{2}\left(u_{i,j} + u_{j,i}\right)$	$\epsilon^{(0)}_{ij} = \frac{1}{2}\left(u_{i,j} + u_{j,i}\right)$	$\epsilon^{(0)}_{ij} = \frac{1}{2}\left(u_{i,j} + u_{j,i}\right)$
$C^{(0)}_{ijkl} = C_{ijkl}$	$C^{(0)}_{ijkl} = C_{ijkl}$ $+\frac{1}{2}\left(\sigma^0_{ik}\delta_{jl} + \sigma^0_{jk}\delta_{il} + \sigma^0_{il}\delta_{jk} + \sigma^0_{jl}\delta_{ik}\right)$	$C^{(0)}_{ijkl} = C_{ijkl}$ $+\frac{1}{2}\left(\sigma^0_{ik}\delta_{jl} + \sigma^0_{jk}\delta_{il} + \sigma^0_{il}\delta_{jk} + \sigma^0_{jl}\delta_{ik}\right)$	$C^{(2)}_{ijkl} = C_{ijkl}$

Table 3.1: Summary of the formulations for each case

Material Property	Value
E_1	107 GPa
E_2	15 GPa
G_{12}	4.3 GPa
ν_{12}	0.3
ν_{21}	0.043
t	0.25 mm

Table 3.2: Material properties of the lamina in the face sheets

Core	Young's Modulus(MPa)	Shear Modulus(MPa)
H30	20	13
H45	40	18
H60	56	22
H80	80	31
H100	105	40
H130	140	52
H200	230	85

Table 3.3: Material properties of the core material from the experiment of Fagerberg

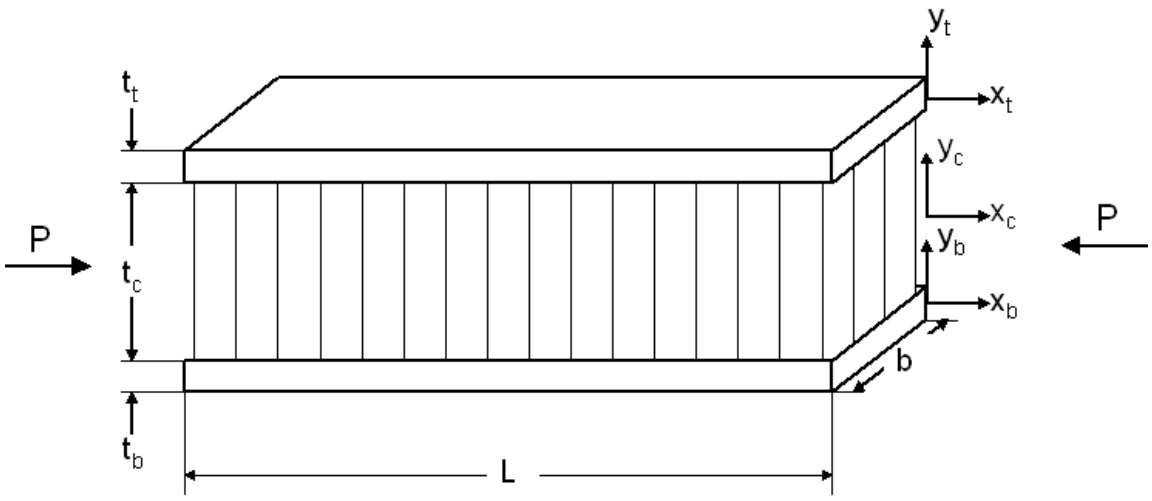

Figure 3.1: Configuration of a sandwich panel

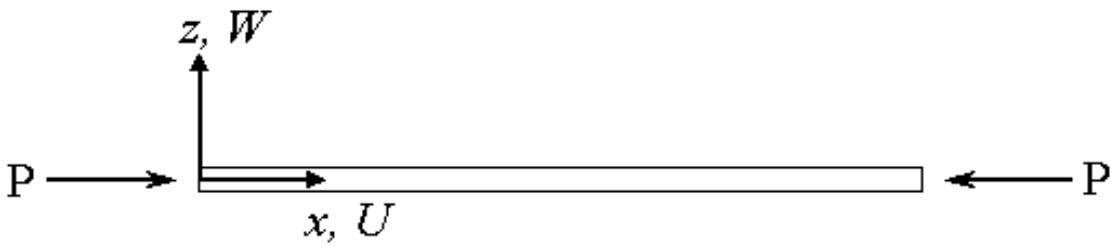

Figure 3.2: Slender beam under uniaxial compressive load

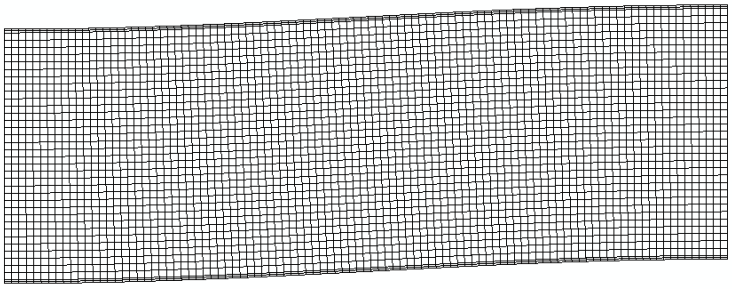

(a)

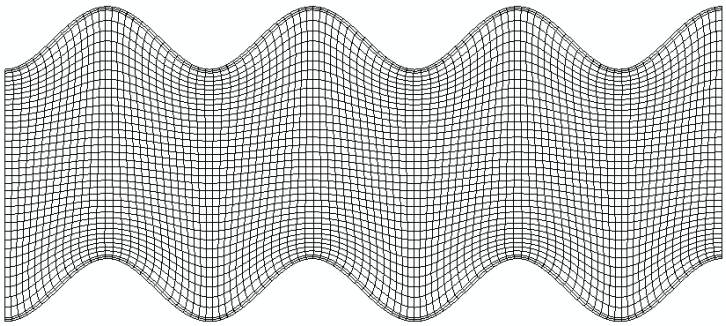

(b)

Figure 3.3: (a) Global buckling deformation (b) Local buckling deformation

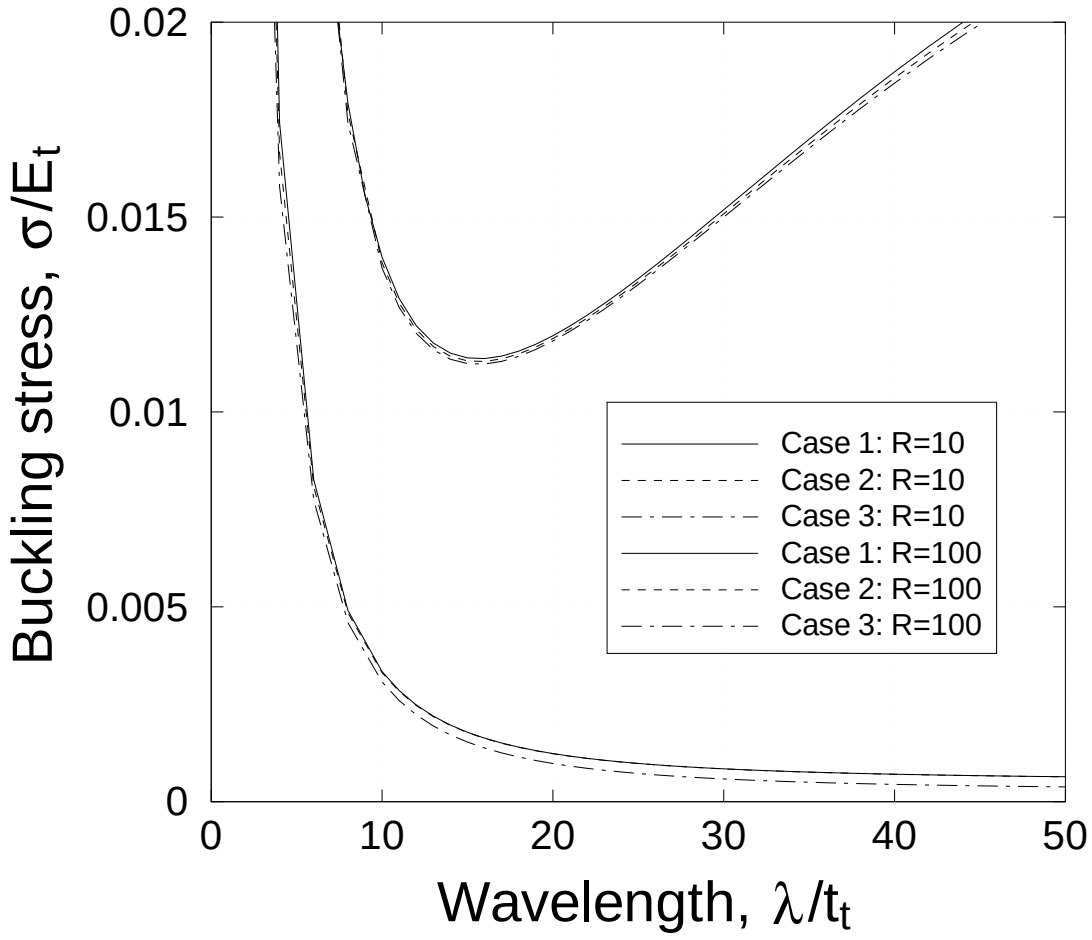

Figure 3.4: Buckling stress variation with different thickness ratio for a fixed core properties

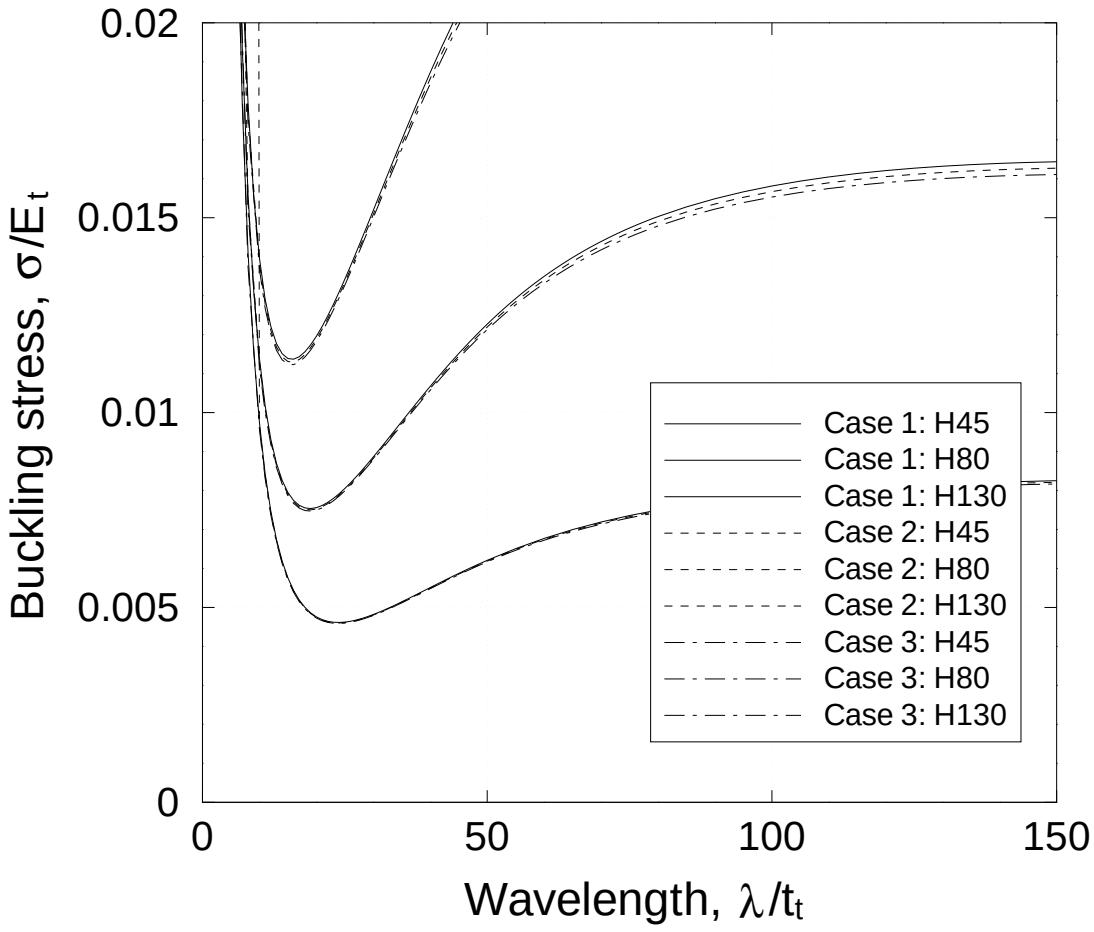

Figure 3.5: Variance of buckling stress with its associated wavelength

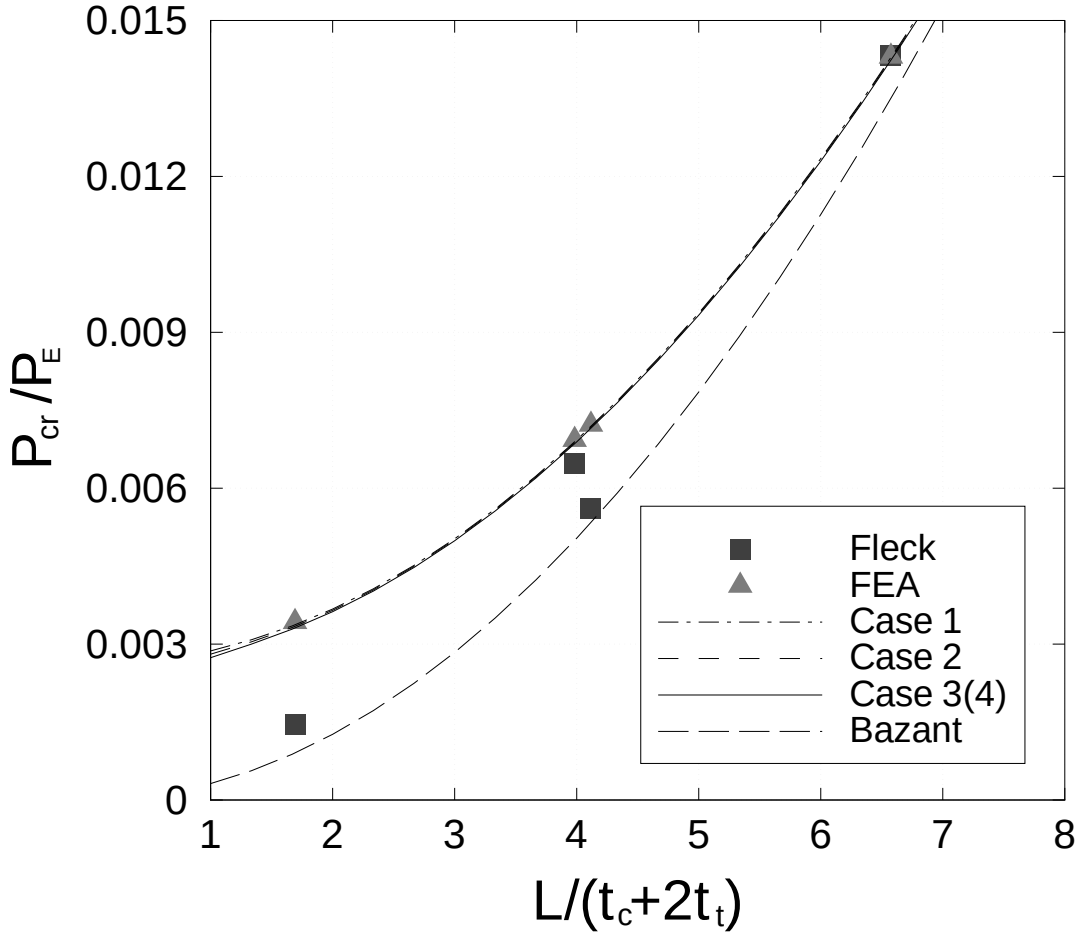

Figure 3.6: Comparison of the prediction for sandwich beam buckling using various formulae and experimental results of Fleck and Sridhar

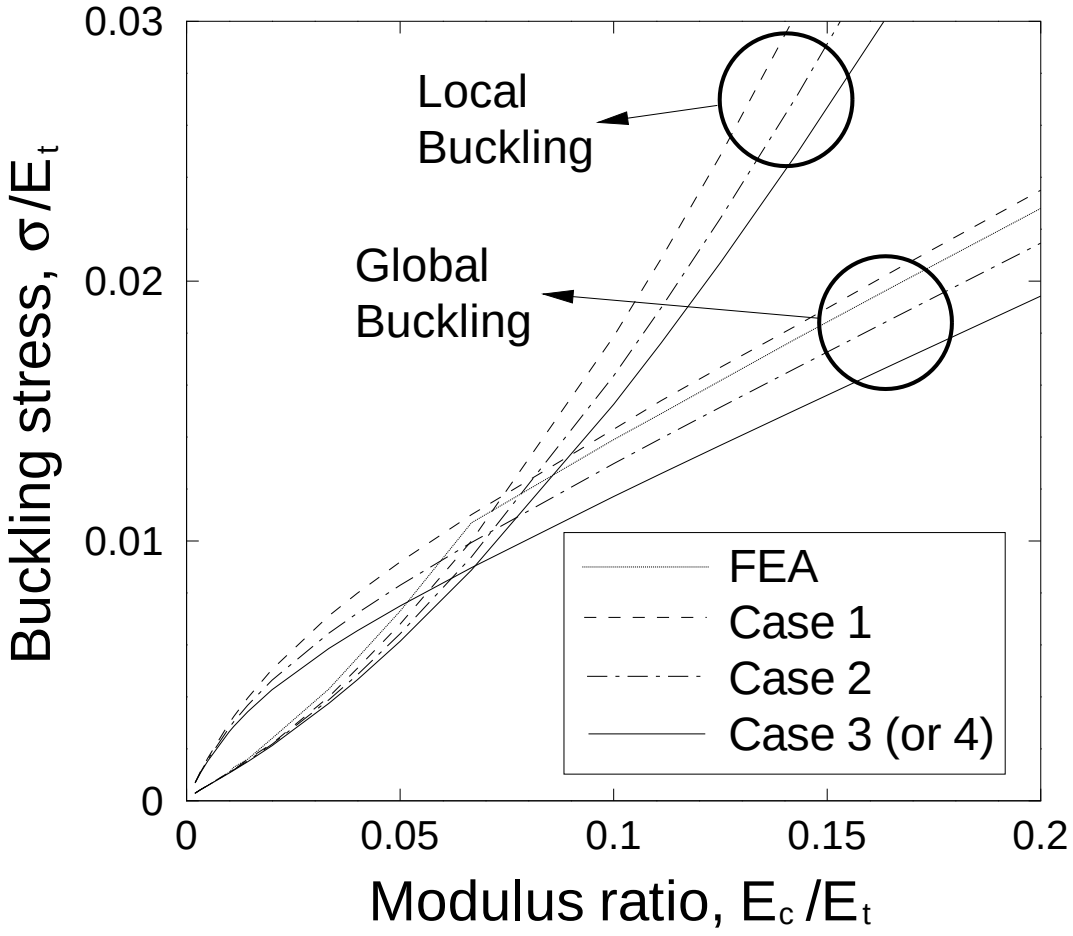

Figure 3.7: Critical buckling stress transition with the core modulus

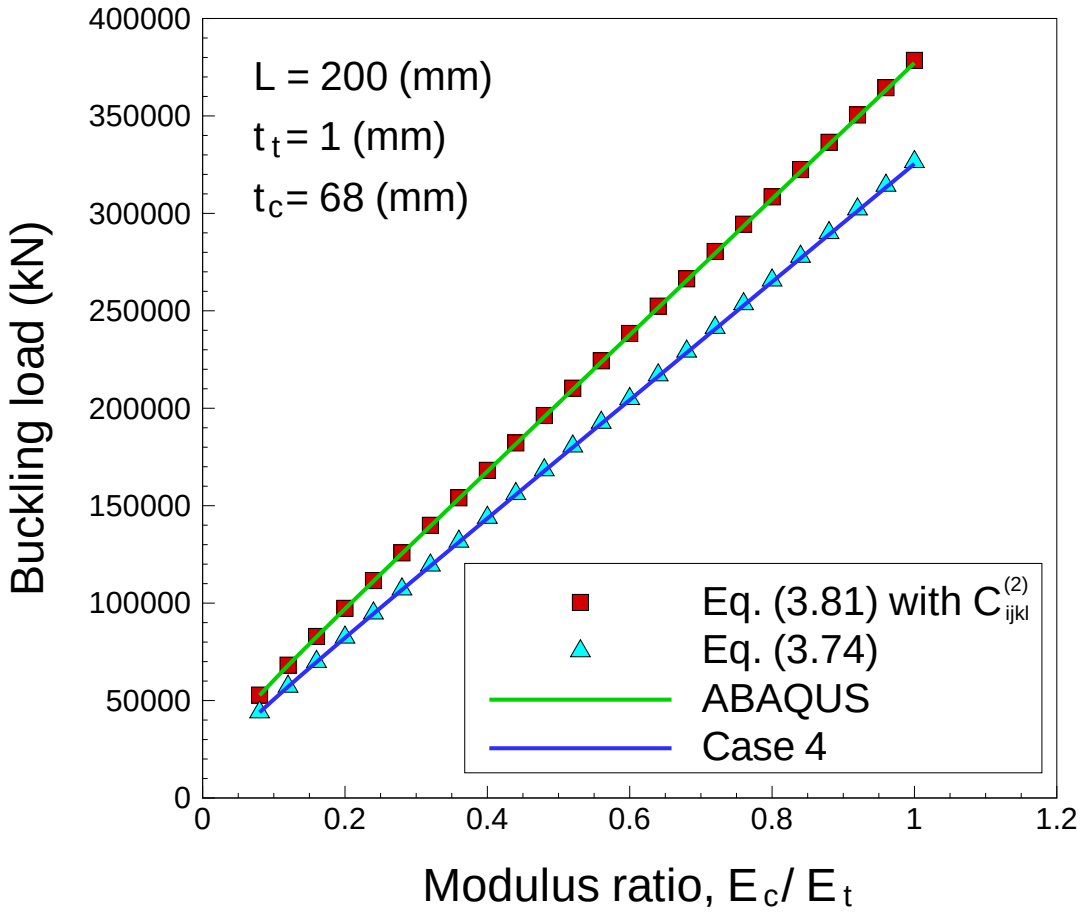

Figure 3.8: Evaluation of the FE formulation Eq.(3.74) and Eq.(3.81) with the constant moduli. Results from ABAQUS and the present analysis are also compared.

CHAPTER IV

Dynamic bifurcation buckling of an impacted column and the temporal evolution of buckling in a dynamically impacted imperfect column[1]

4.1 Introduction

The oldest problem in the literature on structural stability is the celebrated work of Euler who considered the buckling of a slender rod when subjected to axial end compression loads that are slowly applied at one end of a simply supported column [41]. Subsequently, many researchers expanded and extended the notions of buckling, post-buckling and failure, with considerations ranging from the buckling and post-buckling of beam-columns, to plates and shells. A comprehensive treatise on the subject of structural stability is given in [9] and [48].

Long and slender load bearing structural objects are ubiquitous in nature, ranging from mammalian bones to aerospace fuselages to slender and sleek submarines [55]. They are all susceptible to failing by buckling due to excessive destabilizing axial loads. Buckling need not to be catastrophic if the effects it induces are reversible, such as in carbon nanotubes [4], however, in most instances buckling induces large strains that drive material failure leading to structural collapse [9]. The collapse of structures due to buckling has received much attention in the past [48], however,

[1]Parts of this chapter have been published in Ref. [31] in the bibliography. The imperfect column problem is currently being prepared for submission to the International Journal of Solids and Structures.

buckling of structures subjected to loads that are suddenly applied has not received as much attention as their static counterpart [32, 40].

When a long slender beam is subjected to a suddenly applied compressive load at one end, a compressive stress pulse is initiated at the impacted end and travels along the length of the beam at the longitudinal wave velocity given by $c_0 = \sqrt{E/\rho}$, where E is the Young's modulus of the beam and ρ is mass density. If a sufficiently long portion of the beam experiences an axial stress above a certain threshold, then that portion of the beam can buckle, inducing large out-of-plane, transverse displacements. The pattern of displacements is not uniform as shown in Fig. 4.1 and is localized at the impacted end leading to a modulated wave pattern associated with the out-of-plane beam displacement. If the material of the beam is brittle, the buckling can lead to fragmentation [24].

The dynamic buckling of a beam has a rich history having first received attention in [36] and [50]. Many analytical and experimental studies on the dynamic buckling of a beam have been performed since then [3, 13, 15, 17, 24, 26, 27, 28, 35, 42, 46, 47, 56]. In most studies, the effects of the axial stress wave propagation is unaccounted for by assuming that the strain distribution along the beam length is uniform after the impact event, a situation that arises at a much later time after the initiation of impact. In addition to this assumption, dynamic buckling has been typically defined by observing a sudden change or a transition in a system response to values of an appropriately defined load parameter, such as in [15]. This definition of dynamic buckling depends strongly on the particular characteristics of the impacted structure that are being studied. Furthermore, a transition in the system response is usually observed in the post-buckling regime, which may be long after the initiation of the dynamic buckling event. In order to arrive at a more broad but precise definition of

dynamic buckling, it is necessary to capture the physics of how the initial compression wave interacts with the beam deformation, leading to the possibility of investigating the temporal evolution of the beam response, thus leading to a definition of dynamic buckling and the notion of a "critical time" to buckle.

In this chapter, conditions for dynamic bifurcation buckling of an impacted rod is derived. The paper is organized as follows; the equations of motion that govern the problem of a beam impacted by a falling mass is first provided. Next, these equations are simultaneously solved to show the conditions that are necessary for dynamic bifurcation buckling. In doing so, it is identified that the ratio of the impactor mass to beam mass has a strong influence on the time to buckle (t^*), whereas the impactor velocity is found to have a very slight effect. However, for the contact duration, the impactor velocity is a non-factor whereas this duration increases with increasing impactor mass. Our derivations are next applied to available experimental data in [24]. It is to be noted that the notion of dynamic bifurcation buckling used here corresponds to one adopted by Wineman [58], who studied the emergence of multiple equilibrium solutions in a slowly pressurized thin inertialess viscoelastic membrane using the concepts that we have utilized here.

4.2 Problem formulation

4.2.1 Bifurcation analysis: dynamic buckling of a straight beam

The dynamic buckling problem studied here is illustrated in Fig. 4.2 (a). An elastic beam of length L is clamped at one end, while the other end is simply supported. The initially straight and vertical beam is impacted at $x = L$ by a rigid mass M with a velocity of V_0 at time $t = 0$. Employing classical Euler-Bernoulli beam theory [9], and denoting the longitudinal and the transverse displacements, by u and w respectively, in the x and y directions, respectively, the two coupled governing equations of motion

are;

$$\frac{\partial^2 u}{\partial x^2} = \frac{1}{c_0^2}\frac{\partial^2 u}{\partial t^2} \tag{4.1a}$$

$$EI\frac{\partial^4 w}{\partial x^4} + \frac{\partial}{\partial x}\left[F(x,\, t)\frac{\partial w}{\partial x}\right] + \rho A\frac{\partial^2 w}{\partial t^2} = 0 \tag{4.1b}$$

where $c_0 = \sqrt{E/\rho}$, E=Young's modulus, ρ=density, I=second moment of inertia, A=cross sectional area, and $F(x,\, t)$=resultant axial load due to the impact which can be expressed using the wave solution $u(x,\, t)$ as

$$F(x,\, t) = EA\frac{\partial u}{\partial x} \tag{4.2}$$

The initial conditions for the governing equations, Eq. (4.1), are

$$\begin{aligned} u(x,\, 0) &= 0 \\ \frac{\partial u(x,\, 0)}{\partial t} &= 0 \quad \text{for} \quad 0 \leq x < L \\ \frac{\partial u(x,\, 0)}{\partial t} &= -V \quad \text{at} \quad x = L \end{aligned} \tag{4.3}$$

for the axial motion, and

$$\begin{aligned} w(x,\, 0) &= 0 \\ \frac{\partial w(x,\, 0)}{\partial t} &= 0 \end{aligned} \tag{4.4}$$

for the out-of-plane motion, respectively. The beam is considered to be fixed at $x = 0$, and simply supported at the impacted end, $x = L$. Consequently, the boundary conditions are

$$\begin{aligned} u(0,\, t) &= 0 \\ M\frac{\partial^2 u(L,\, t)}{\partial t^2} &= Mg - EA\frac{\partial u(L,\, t)}{\partial x} \end{aligned} \tag{4.5}$$

for the longitudinal displacement, and

$$\begin{aligned} w(0,\, t) = 0 \quad \text{and} \quad \frac{\partial w(0,\, t)}{\partial x} \\ w(L,\, t) = 0 \quad \text{and} \quad \frac{\partial^2 w(L,\, t)}{\partial x^2} = 0 \end{aligned} \tag{4.6}$$

for the transverse displacement. Note that the boundary condition at $x = L$ for the axial motion in Eq. (4.5) is valid as long as the impactor mass is in contact with the impacted end of the beam.

The axial motion is first considered to obtain the wave propagation as a result of impulsive axial compression. Once the stress distribution, which is non-uniform in time and space, is obtained from the wave solution, it can be applied to Eq. (4.1b) to investigate the existence of dynamic bifurcation. In order to obtain the full wave solution, Laplace transform of Eq. (4.1a) is taken, considering the initial conditions Eq. (4.3),

$$\frac{\partial^2 \bar{u}(x,\, s)}{\partial x^2} - \left(\frac{s}{c_0}\right)^2 \bar{u}(x,\, s) = \frac{V_0}{c_0^2} H(x - L) \tag{4.7}$$

where $\bar{u}(x,\, s)$ is the transformed axial displacement, $u(x,\, t)$ and H is the heaviside step function. Then, $\bar{u}(x,\, s)$ is subjected to the transformed boundary conditions of Eq. (4.5)

$$\begin{gathered} \bar{u}(0,\, s) = 0 \\ M\left[s^2 \bar{u}(L,\, s) + V_0\right] = Mg\,\frac{1}{s} - EA\,\frac{\partial \bar{u}(L,\, s)}{\partial x} \end{gathered} \tag{4.8}$$

The general solution to the second order ordinary differential equation Eq. (4.7) can be written as

$$\bar{u}(x,\, s) = C_1\, e^{(s/c_0)x} + C_2\, e^{-(s/c_0)x} + \frac{e^{-\frac{s}{c_0}(L+x)}}{2s^2}\left\{\, e^{(s/c_0)L} - e^{(s/c_0)x}\right\}\, {}^2V_0 H(x - L) \tag{4.9}$$

where C_1 and C_2 are unknown constants. The unknown constants can be determined

from the boundary conditions, Eq. (4.8). Therefore, $\bar{u}(x,\, s)$ is obtained as

(4.10)
$$\begin{aligned}\bar{u}(x,\, s) &= \frac{M(g - sV_0)}{s^2\left\{\left(\frac{EA}{c_0} + Ms\right)e^{(s/c_0)L} + \left(\frac{EA}{c_0} - Ms\right)e^{-(s/c_0)L}\right\}} \times \left(e^{\frac{s}{c_0}x} - e^{-\frac{s}{c_0}x}\right) \\ &= \frac{M(g - sV_0)}{s^2}\frac{1}{EA/c_0 + Ms}\left[e^{\frac{s}{c_0}(x-L)} - e^{-\frac{s}{c_0}(x+L)}\right] \\ &\quad - \frac{M(g - sV_0)}{s^2}\frac{EA/c_0 - Ms}{(EA/c_0 + Ms)^2}\left[e^{\frac{s}{c_0}(x-3L)} - e^{-\frac{s}{c_0}(x+3L)}\right] \\ &\quad + \frac{M(g - sV_0)}{s^2}\frac{(EA/c_0 - Ms)^2}{(EA/c_0 + Ms)^3}\left[e^{\frac{s}{c_0}(x-5L)} - e^{-\frac{s}{c_0}(x+5L)}\right] - \cdots\end{aligned}$$

Now we take inverse Laplace transform of Eq. (4.10) to obtain the axial displacement in the time domain, which is,

(4.11)
$$\begin{aligned}&u(x,\, t) \\ &= f_1(x,\, t)H\left(t - \frac{L+x}{c_0}\right) + f_2(x,\, t)H\left(t - \frac{L-x}{c_0}\right) \\ &\quad + f_3(x,\, t)H\left(t - \frac{3L+x}{c_0}\right) + f_4(x,\, t)H\left(t - \frac{3L-x}{c_0}\right) \\ &\quad + f_5(x,\, t)H\left(t - \frac{5L+x}{c_0}\right) + f_6(x,\, t)H\left(t - \frac{5L-x}{c_0}\right)\end{aligned}$$

where H is the Heaviside step function and $f_i(x,\, t)$ $(i = 1, 2, 3, \cdots)$ are coefficient functions as a result of the inverse transform. The first two coefficient functions are written, for example,

(4.12)
$$\begin{aligned}f_1(x,\, t) &= -\frac{c_0 M}{EA}g\left(t - \frac{L+x}{c_0}\right) + \left(\frac{c_0 M}{EA}g + V_0\right)\frac{c_0 M}{EA}\left[1 - e^{-\frac{EA}{c_0 M}\left(t - \frac{L+x}{c_0}\right)}\right] \\ f_2(x,\, t) &= -\frac{c_0 M}{EA}g\left(t - \frac{L-x}{c_0}\right) - \left(\frac{c_0 M}{EA}g + V_0\right)\frac{c_0 M}{EA}\left[1 - e^{\frac{EA}{c_0 M}\left(t - \frac{L-x}{c_0}\right)}\right]\end{aligned}$$

and so on. Eq. (4.11) can be used to describe the non-uniform strain distribution in time and space, considering the wave propagation effect in the beam of finite length.

Next, the out-of-plane equation of motion, Eq. (4.1b), is considered. Obviously, $w_0(x,\, t) = 0$ is the trivial solution to Eq. (4.1b) irrespective of time t and axial force $F(x,\, t)$. We are seeking to find the critical time t^* corresponding to the emergence

of a non-trivial solution $w_1(x,\, t) \neq 0$ satisfying Eq. (4.1b). If $w_1(x,\, t) \neq 0$ is another solution to Eq. (4.1b), along a bifurcated path, then, $w_1(x,\, t^* + \Delta t)$ must also satisfy Eq. (4.1b), when Δt is infinitesimally small. It follows that,

$$\frac{\partial^4 w_1(x,\, t^*)}{\partial x^4} + \frac{1}{\kappa^2}\frac{\partial}{\partial x}\left[\frac{\partial u(x,\, t^*)}{\partial x}\frac{\partial w_1(x,\, t^*)}{\partial x}\right] + \beta^4 \frac{\partial^2 w_1(x,\, t^*)}{\partial t^2} = 0 \tag{4.13a}$$

(4.13b)

$$\frac{\partial^4 w_1(x,\, t^* + \Delta t)}{\partial x^4} + \frac{1}{\kappa^2}\frac{\partial}{\partial x}\left[\frac{\partial u(x,\, t^* + \Delta t)}{\partial x}\frac{\partial w_1(x,\, t^* + \Delta t)}{\partial x}\right] + \beta^4 \frac{\partial^2 w_1(x,\, t^* + \Delta t)}{\partial t^2} = 0$$

where κ=radius of gyration and $\beta^4 = \rho A/EI$. Using the Taylor series for expanding terms in Eq. (4.13b) and neglecting higher order terms after the expansion, Eq. (4.13b) can be reduced to

$$\frac{\partial}{\partial t}\left[\frac{\partial^4 w_1(x,\, t^*)}{\partial x^4} + \frac{1}{\kappa^2}\frac{\partial}{\partial x}\left\{\frac{\partial u(x,\, t^*)}{\partial x}\frac{\partial w_1(x,\, t^*)}{\partial x}\right\} + \beta^4 \frac{\partial^2 w_1(x,\, t^*)}{\partial t^2}\right]\Delta t = 0 \tag{4.14}$$

with the aid of Eq. (4.13a). Since $\Delta t \neq 0$, it follows that,

$$\frac{\partial}{\partial t}\left[\frac{\partial^4 w_1}{\partial x^4} + \frac{1}{\kappa^2}\frac{\partial}{\partial x}\left\{\frac{\partial u}{\partial x}\frac{\partial w_1}{\partial x}\right\} + \beta^4 \frac{\partial^2 w_1}{\partial t^2}\right] = 0 \quad \text{at} \quad t = t^* \tag{4.15}$$

Eq. (4.15) provides the condition to determine t^*. Eq. (4.15) can be further simplified in view of Eq. (4.13a) to finally yield,

$$\frac{\partial^4 w_1}{\partial x^4} + \frac{1}{\kappa^2}\frac{\partial}{\partial x}\left[\frac{\partial u}{\partial x}\frac{\partial w_1}{\partial x}\right] + \beta^4 \frac{\partial^2 w_1}{\partial t^2} = 0 \quad \text{at} \quad t = t^* \tag{4.16}$$

as the final condition to determine $t = t^*$.

Following the exposition in [9], a non-trivial solution to Eq. (4.16) is assumed in the form

$$w_1(x,\, t) = f(t)W(x), \tag{4.17}$$

with the D'Alembert substitution $f(t) = e^{i\Omega t}$, so that

$$w_1(x,\, t) = e^{i\Omega t}W(x) \tag{4.18}$$

Substituting Eq. (4.18) into Eq. (4.16) results in,

$$\frac{d^4W}{dx^4} + \frac{1}{\kappa^2}\frac{\partial}{\partial x}\left(\frac{\partial u}{\partial x}\frac{dW}{dx}\right) = \Omega^2\beta^4 W \quad \text{at} \quad t = t^* \tag{4.19}$$

which is subjected to the clamped-simply supported boundary conditions,

$$\begin{aligned} W = 0 \quad \text{and} \quad \frac{dW}{dx} = 0 \quad \text{at} \quad x = 0 \\ W = 0 \quad \text{and} \quad \frac{d^2W}{dx^2} = 0 \quad \text{at} \quad x = L \end{aligned} \tag{4.20}$$

The solution to Eq. (4.19) is assumed to be

$$W(x) = \sum_{i=1}^{N} A_i \phi_i(x) \tag{4.21}$$

where A_i=constant and $\phi_i(x)$ are the eigenfunctions of a clamped-simply supported beam undergoing free vibration. Consequently, $\phi_i(x)$ satisfies the geometric and natural boundary conditions prescribed by Eq. (4.20). Using Eq. (4.21), the problem posed by Eq. (4.19) and Eq. (4.20) can be rewritten as,

$$[k_{ij} - P_{ij}]\{A_j\} = \Omega^2 [m_{ij}]\{A_j\} \tag{4.22}$$

where A_i=column vector consisting of the coefficients, and the k_{ij}, P_{ij}, and m_{ij} are defined as

$$k_{ij} = k_{ji} = \int_0^L \frac{d^2\phi_i}{dx^2}\frac{d^2\phi_j}{dx^2}dx \tag{4.23}$$

$$P_{ij} = P_{ji} = \frac{1}{\kappa^2}\int_0^L \frac{\partial u}{\partial x}\frac{d\phi_i}{dx}\frac{d\phi_j}{dx}dx \tag{4.24}$$

$$m_{ij} = m_{ji} = \beta^4 \int_0^L \phi_i\phi_j dx \tag{4.25}$$

It should be noted that P_{ij} is a function of time. The system, Eq. (4.22), admits a non-trivial solution when the determinant,

$$\left|k_{ij} - P_{ij} - \Omega^2 m_{ij}\right| = 0 \tag{4.26}$$

The solution, Eq. (4.18), is always bounded when all the eigenvalues, Ω, are real. When one or more of the eigenvalues Ω becomes complex with a negative imaginary part, the solution becomes unbounded and an instability is indicated. The first instance at which this occurs, denoted as $t = t^*$, is called the *critical time to buckle*. Once this time is determined, the corresponding mode shape and buckling load can be obtained.

4.2.2 Response analysis: beam with a initial deflection

When the beam is initially crooked such as in Fig. 4.2 (b), Eq. (4.1b) should be rewritten as, [18],

$$EI\frac{\partial^4 w}{\partial x^4} + \frac{\partial}{\partial x}\left[F(x,\,t)\frac{\partial w}{\partial x}\right] + \rho A\frac{\partial^2 w}{\partial t^2} = EI\frac{\partial^4 w_0}{\partial x^4} \tag{4.27}$$

considering the geometric initial curvature. The initial conditions for the governing equation, Eq. (4.27), are

$$\begin{aligned} w(x,\,0) &= w_0(x) \\ \frac{\partial w(x,\,0)}{\partial t} &= 0 \end{aligned} \tag{4.28}$$

The axial solution obtained earlier enters as an axial force term in the out-of-plane equation of motion, Eq. (4.27). Here, we are assuming that

$$\frac{\parallel w_0(x) \parallel}{t} \ll 1 \tag{4.29}$$

, so that the axial wave propagation solution developed earlier for the perfect straight beam is still valid. The solution to Eq. (4.27) can be assumed as

$$w(x,\,t) = \sum_{i=1}^{N} \eta_i(t)\phi_i(x) \tag{4.30}$$

where $\eta_i(t)$ are unknown time functions to be solved and $\phi_i(x)$ are the eigenfunctions of a clamped-simply supported beam undergoing free vibration. Substitution of the

assumed solution Eq. (4.30) to Eq. (4.27) yields

$$EI\sum_{i=1}^{N}\eta_i(t)\phi_i''''(x)+\Big\{F\sum_{i=1}^{N}\eta_i(t)\phi_i'(x)\Big\}'+\rho A\sum_{i=1}^{N}\ddot{\eta}_i(t)\phi_i(x)=EIw_0''''(x) \tag{4.31}$$

where $'$ denotes differentiation with respect to x and $\cdot$ denotes differentiation with respect to t. In order to take advantage of orthogonality, Eq. (4.31) is multiplied by $\phi_j(x)$ and integrated over the beam length. Eq. (4.31) can be rewritten as

$$\Big[\rho A\int_0^L\phi_j(x)^2\Big]\ddot{\eta}_j(t)+\Big[EI\int_0^L\phi_j''(x)^2dx\Big]\eta_j(t)+\Big[F\Big\{\sum_{i=1}^{N}\eta_i(t)\phi_i'(x)\Big\}\phi_j(x)\Big]_0^L - \int_0^L F\Big\{\sum_{i=1}^{N}\eta_i(t)\phi_i'(x)\Big\}\phi_j'(x)dx=EI\int_0^L w_0''(x)\phi_j''(x)dx \tag{4.32}$$

The initial displacements can be expressed

$$w_0(x)=\sum_{i=1}^{N}a_i\phi_i(x) \tag{4.33}$$

where

$$a_n=\rho AL\int_0^L w_0(x)\phi_n(x)dx \tag{4.34}$$

Here, the orthogonality condition

$$\rho AL\int_0^L\phi_i(x)\phi_j(x)dx=\delta_{ij} \tag{4.35}$$

has been used, where δ_{ij} is the Kronecker's delta. Suppose that the initial imperfection shape corresponds to the first mode shape, which is

$$w_0(x)=w(x,\,0)=\sum_{i=1}^{N}a_i\phi_i(x)=a_1\phi_1(x) \tag{4.36}$$

then, a series of coupled linear differential equations are obtained

$$\Big[\rho A\int_0^L\phi_1(x)^2\Big]\ddot{\eta}_1(t)+\Big[EI\int_0^L\phi_1''(x)^2dx\Big]\eta_1(t)-\Big[\int_0^L F\phi_1'(x)^2dx\Big]\eta_1(t) -\Big[\int_0^L F\phi_2'(x)\phi_1'(x)dx\Big]\eta_2(t)-\Big[\int_0^L F\phi_3'(x)\phi_1'(x)dx\Big]\eta_3(t)\cdots=\Big[EI\int_0^L\phi_1''(x)^2dx\Big]a_1 \tag{4.37}$$

(4.38)

$$\left[\rho A\int_0^L \phi_2(x)^2\right]\ddot{\eta}_2(t)+\left[EI\int_0^L \phi_2''(x)^2dx\right]\eta_2(t)-\left[\int_0^L F\phi_1'(x)\phi_2'(x)dx\right]\eta_1(t)$$
$$-\left[\int_0^L F\phi_2'(x)^2dx\right]\eta_2(t)-\left[\int_0^L F\phi_3'(x)\phi_2'(x)dx\right]\eta_3(t)\cdots=\left[EI\int_0^L \phi_2''(x)^2dx\right]a_2$$

(4.39)

$$\left[\rho A\int_0^L \phi_3(x)^2\right]\ddot{\eta}_3(t)+\left[EI\int_0^L \phi_3''(x)^2dx\right]\eta_3(t)-\left[\int_0^L F\phi_1'(x)\phi_3'(x)dx\right]\eta_1(t)$$
$$-\left[\int_0^L F\phi_2'(x)\phi_3'(x)dx\right]\eta_2(t)-\left[\int_0^L F\phi_3'(x)^2dx\right]\eta_3(t)\cdots=\left[EI\int_0^L \phi_3''(x)^2dx\right]a_3$$

This system of linear differential equations can be solved numerically. The solution will be used to study the effects of an initial geometric imperfection on the critical time and other critical parameters obtained from the bifurcation analysis.

4.3 Results and discussion

4.3.1 Bifurcation analysis: critical time, critical wavelength, and dynamic buckling load

The conditions derived earlier for dynamic buckling also finds interpretation from an energetic view point. We find that when the kinetic energy of the impactor, defined by its mass and velocity, is high enough, and the mass and the beam are in contact for a sufficiently long time, then the condition for dynamic buckling is met. If the momentum of the falling mass is not sufficient to overcome the elastic resistance to buckling (lack of flexural rigidity), then the mass and the beam will lose contact prior to meeting the condition for dynamic buckling. Once the impacting mass looses contact, the beam will undergo free vibrational response, limited to axial motion, since there is not sufficient energy to excite dynamic buckling. This is because the compressive strain along the beam after the impact is negated due to the reflected stress wave from the fixed end, which is tensile. Therefore, for dynamic buckling to occur, the beam must be in contact with the falling mass of a sufficiently

large kinetic energy, for a sufficiently long duration. A stiffer material such as steel will require much higher kinetic energy for a longer contact duration in order to initiate dynamic buckling than for a soft material such as teflon.

The contact duration of the striking mass at the impacted beam end can be obtained by using the wave solution for the axial motion presented earlier (see Eq. (4.11)). At the instance when the mass looses contact with the beam, i.e., when the impacted end becomes free, the boundary condition for the axial motion at $x = L$ is altered to

$$\frac{\partial u(L,\, t)}{\partial x} = 0 \tag{4.40}$$

By substituting the axial wave solution, Eq. (4.11), to Eq. (4.40), the time corresponding to the loss of contact, $\hat{t}$, can be obtained. Again, the buckling time, t^*, can be obtained from Eq. (4.26).

Fig. 4.3 shows the contact duration and the buckling time, t^*, for, (a) a fixed impactor velocity and as a function of impactor mass, and, (b) a fixed impactor mass and as a function of impactor velocity. As can be seen in Fig. 4.3, the contact duration is independent of the impact velocity, while it increases as the impactor mass increases. A critical time to buckle, t^*, does not exist for low impactor velocities and masses, as shown in Fig. 4.3 (a) and (b), indicating axial free vibration of the beam after the contact duration $\hat{t}$. The dynamic buckling is initiated at time t^* and this time is also indicated in these figures.

When the beam dynamically bifurcates at, $t = t^*$, the buckling mode shapes show modulations over the entire length of beam, which is characteristic of a *dynamic* buckling event. In a *static*, progressive buckling event, the localized pattern is confined to the end where the load is applied. It is to be noted that in a real experiment, small unintended deviations in the initial straightness of the beam or slight eccen-

tricity in the direction of the falling mass will result in observed dynamic buckling initiating earlier than that predicted by the analysis here. The effect of small initial imperfections on the dynamic buckling of a beam is addressed elsewhere (Ji and Waas 2008). Fig. 4.4 shows typical examples of the deformed beam shape with different impactor velocities. As illustrated in Fig. 4.4, the buckling wavelength is defined by dividing the entire beam length with the number of nodes at the undeformed original beam position. Since the buckle mode shape is localized at the impacted end and shows non-uniformity along the beam length, such an "averaging" procedure was implemented for comparing predictions against experiment. Fig. 4.5, Fig. 4.6, and Fig. 4.7 shows comparisons of the present theoretical normalized wavelengths, (λ/d), with experimental results for a variety of materials with a wide range of values of elastic properties. These properties are listed in Table 4.1. In the experiments reported in [24], the buckling event and buckle mode shapes were recorded with the aid of a high-speed camera. Using the definition of an averaged wavelength as described here, we have compared our predictions against the experimental data. However, there is no mention of how the "wavelength" reported in [24], was obtained. As can be seen from the figures, the analytical "average" wavelengths from the present analysis are in very good agreement with the all the experimental results. At shorter wavelengths, it is likely that a better model of the beam (such as a Timoshenko beam model) would provide even better agreement, and this is a subject of current study. The present results show that the dependence of dynamic buckling on the relative properties of the impactor and the beam as depicted in Fig. 4.3 has been captured accurately by the present analysis.

When the material is brittle (like pasta rods), experimental results indicate that the rod fragments. Images of the buckling event (see Figure 1 of [24]) show that

the modulated buckle shape leads to distinct points along the beam length where the curvature is a maximum. These are also the locations where the strains at buckling exceed the maximum strain limit of the material leading to fragmentation. The fragments appear to be of different lengths because the spacing between the maximum curvature locations is not constant, gradually increasing away from the impacted end. Because the modulated buckle mode shape has been computed in the present work, these shapes can be used to obtain statistics associated with the fragment lengths, thus shedding more insight into the process of fragmentation that is due to the dynamic buckling event.

Because the internal axial force resultant, $N(x,t)$, is spatially non-uniform, the dynamic buckling load can be defined as

$$P = \frac{1}{L^*}\int_0^{L^*} N(x,t)dx \quad \text{at} \quad t = t^* \tag{4.41}$$

where $N(x,t)$=internal axial force of the beam at position, x, and time, t, and $L^* = c_0 t^*$. It is noted that $L^* = L$ after the axial strain distribution is fully developed over the entire beam length (i.e., for $t^* \geq L/c_0$). Fig. 4.8 shows the computed dynamic buckling loads as a function of the impact velocity for the different materials listed in Table 4.1. It appears that the ratio between the dynamic buckling load and the static Euler buckling load is very large for the softer material at the same impact mass and impact velocity. This shows that a larger kinetic energy is required to initiate dynamic buckling in the stiffer material. These physical attributes have been quantified accurately in the present paper through the solution of the coupled equations of motion (Eq. (4.1a) and Eq. (4.1b)), that govern the dynamic buckling event.

4.3.2 Dynamic responses of a beam with an initial imperfection

Dynamic buckling will occur earlier than that predicted for the straight beam if the beam has a geometric imperfection because the crooked beam will deflect immediately after impact. Fig. 4.9 shows an example of the response of a crooked beam to the axial impact as time develops. The column is of length 190mm, with circular cross-section of diameter, t = 1.6mm, impacted by masses of 10 g with a velocity of 0.3 m/s. The initial shape is assumed to be the first natural vibration mode of a clamped-simply supported beam. The time is normalized by the critical time, t^*, and the deflection is measured from the initial deflection. As shown in Fig. 4.9, the beam starts to deform immediately after impact and the deformation is localized at the impacted end. As time develops, the axial stress wave propagates to the other end and the out-of-plane deformation also grows. Notice that the scale of the magnitude axis when the time reaches the critical time t^* is much greater than the other figures.

Fig. 4.10 shows another example for the response of the crooked beam as a function of the impact velocity. The initial shape is assumed to be the first natural mode of a clamped-simply supported beam. The response of the crooked beam is measured by $\bar{w}$ which is defined by

$$\bar{w} = \frac{1}{L}\int_0^L \|w(x,\, t^*)\|dx \tag{4.42}$$

where L=beam length, w=out-of-plane displacement, and t^*=critical time obtained through the bifurcation analysis. Fig. 4.10 also shows the normalized critical time $T^* = t^*/(L/c_0)$ for each case. A general trend for the response of the crooked beam is clearly noticeable in Fig. 4.10. The out-of-plane deformation of the beam begins immediately after impact and it starts diverging after the critical time. Furthermore,

the deformation increases as the impactor velocity increases.

When defining the axial load of the beam with a geometric imperfection, the initial curvature should be accounted for in Eq. (4.43). Thus, for a beam with an initial geometric imperfection, Eq. (4.43) is altered to

$$P = \frac{1}{L^*}\int_0^{L^*} EA\Big[\frac{du}{dx} + \frac{1}{2}\Big(\frac{dw}{dx}\Big)^2 - \frac{1}{2}\Big(\frac{dw_0}{dx}\Big)^2\Big]dx \quad \text{at} \quad t = t^* \tag{4.43}$$

Fig. 4.11 shows the axial load of the crooked beam as a function of the maximum initial deflection, $\hat{w}_0$. The maximum deflection, $\hat{w}_0$, appears as a percentage of the beam length in Fig. 4.11. The shape of the initial deflection is assumed again to be the first natural vibration mode of a clamped-simply supported beam. The axial load is computed at the the critical time, t^*, since the beam will deform immediately after impact because of the initial deflection. The axial load in Fig. 4.11 is normalized by the static Euler buckling load. As shown in Fig. 4.11, the axial load decreases as the initial deflection increases.

The effect of the beam length on the dynamic response of the crooked beam is also studied in Fig. 4.12. The maximum initial deflection of the beam, $\hat{w}_0$, is fixed at 2mm. Again, $\bar{w}$, defined in Eq. (4.42) is used to measure the response of the beam as the length of the beam changes. The normalized critical time, T^*, for each case obtained from the bifurcation analysis is also indicated in Fig. 4.12. As shown in Fig. 4.12, the response of the beam decreases as the beam becomes longer. In fact, dynamic buckling occurs very fast according to the critical time in Fig. 4.12 as the beam length increases. During that short time duration, only a small portion of the beam will experience a significant deformation because the axial wave propagates as far as $c_0 t^*$.

4.4 Concluding remarks

The dynamic bifurcation buckling of an axially impacted column has been considered. A critical time to buckle, which is the dynamic counterpart of the critical load corresponding to the celebrated static Euler buckling problem has been derived and shown to be the first indicator that signals the onset of dynamic bifurcation. Unlike in the static problem, the dynamic buckling problem results in localized non-uniform buckle mode shapes associated with the interactions between the in-plane and out-of-plane deformation responses. The influences of the impactor mass and impactor velocity have been accurately captured and it is seen that the impactor mass has a substantial influence on the dynamic bifurcation buckling event. Extensions of the concept of a critical time to buckle has applications to other beam, plate and shell structures, including problems for which material rate effects are also important.

	E (GPa)	ρ (kg/m^3)
Steel	200	7900
Pasta	2.9	1500
Teflon	0.5	2200

Table 4.1: Properties of various beam materials

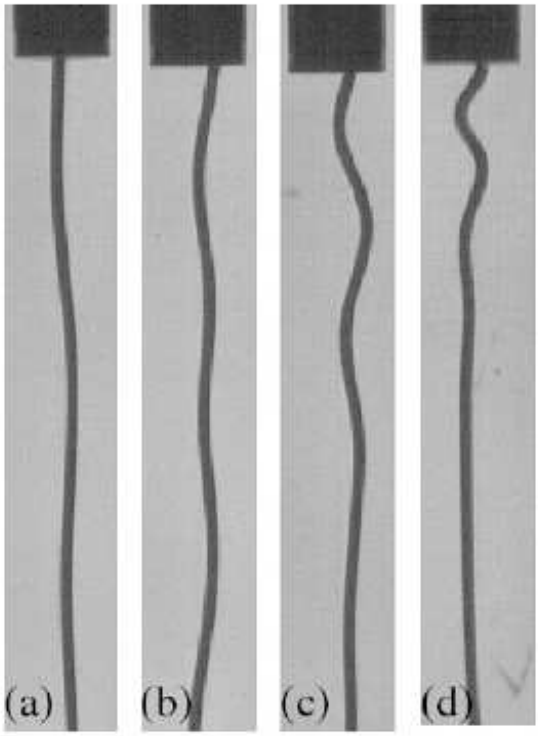

Figure 4.1: Localized buckled shape of a PTFE teflon rod after impact by a steel projectile with velocity of (a) 0.7 (m/s) (b) 4.6 (m/s) (c) 11.2 (m/s) (d) 26.0 (m/s) reproduced here from Gladden et al. (2005)

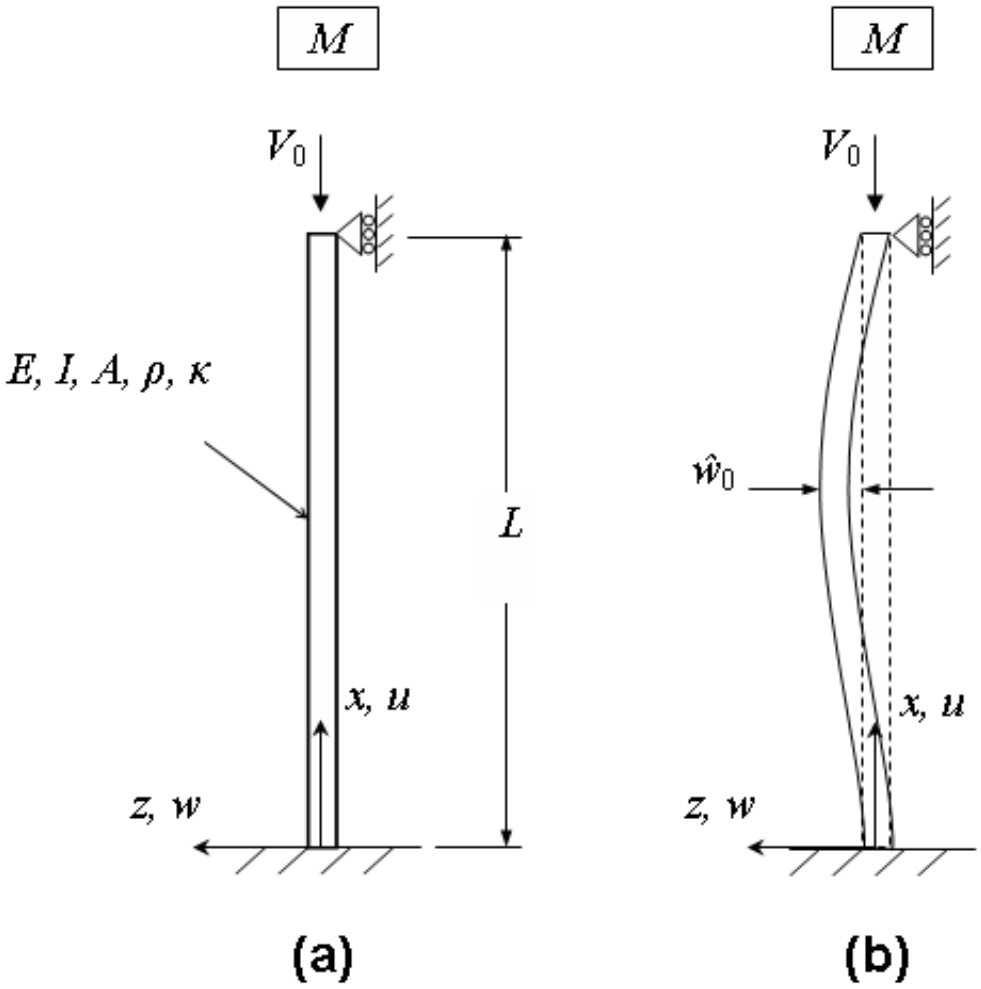

Figure 4.2: Configuration of a slender beam subjected to axial impact

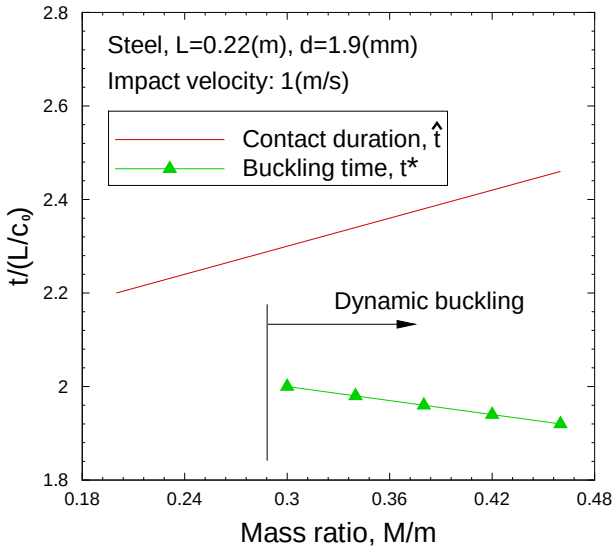

(a)

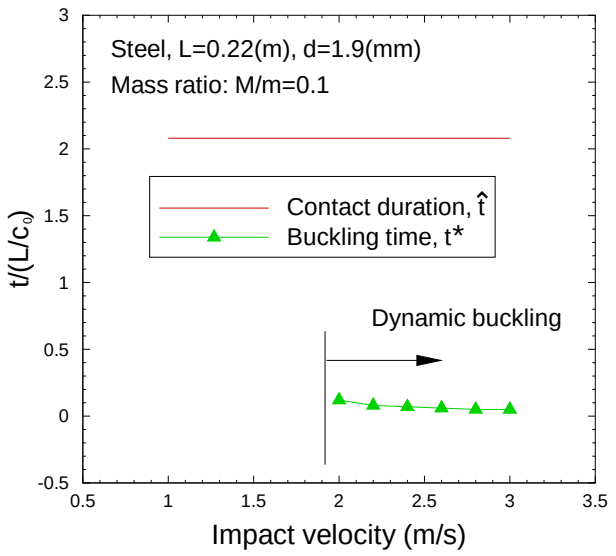

(b)

Figure 4.3: Contact duration and buckling time with variances of (a) impact mass and (b) impact velocity

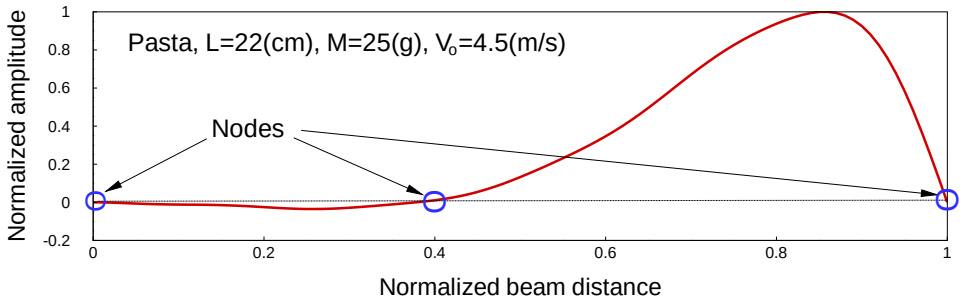

(a)

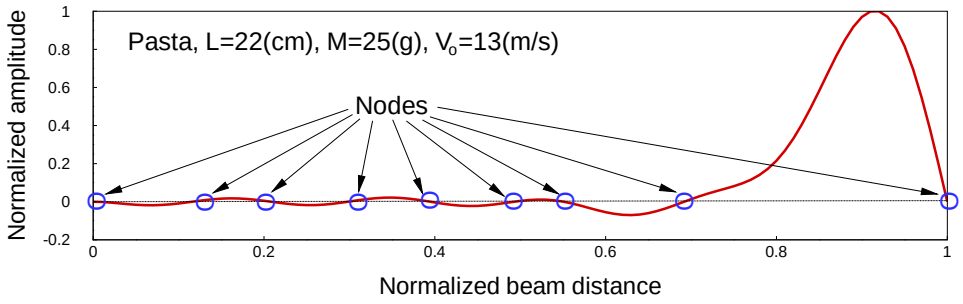

(b)

Figure 4.4: Dynamic buckling mode shapes corresponding to two different impactor velocities

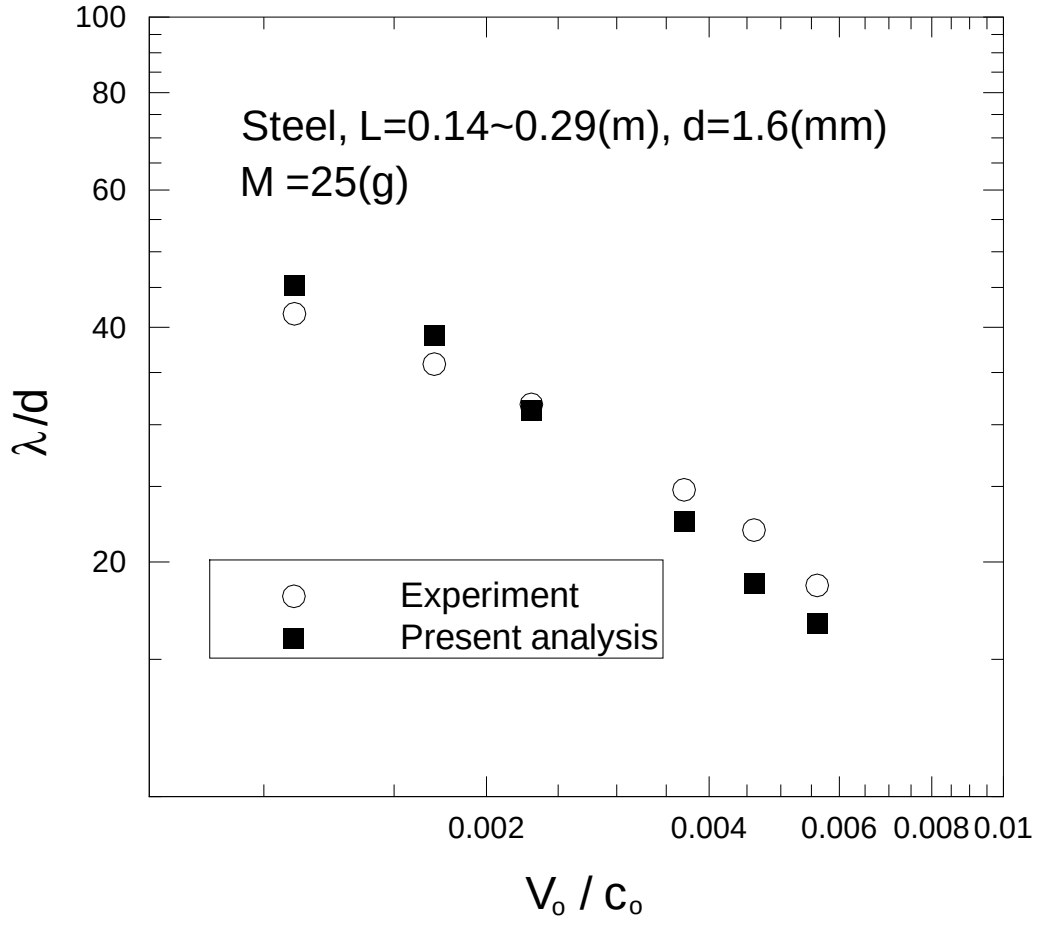

Figure 4.5: Comparison of the predicted critical wavelength from the present analysis against experimental results for a steel beam

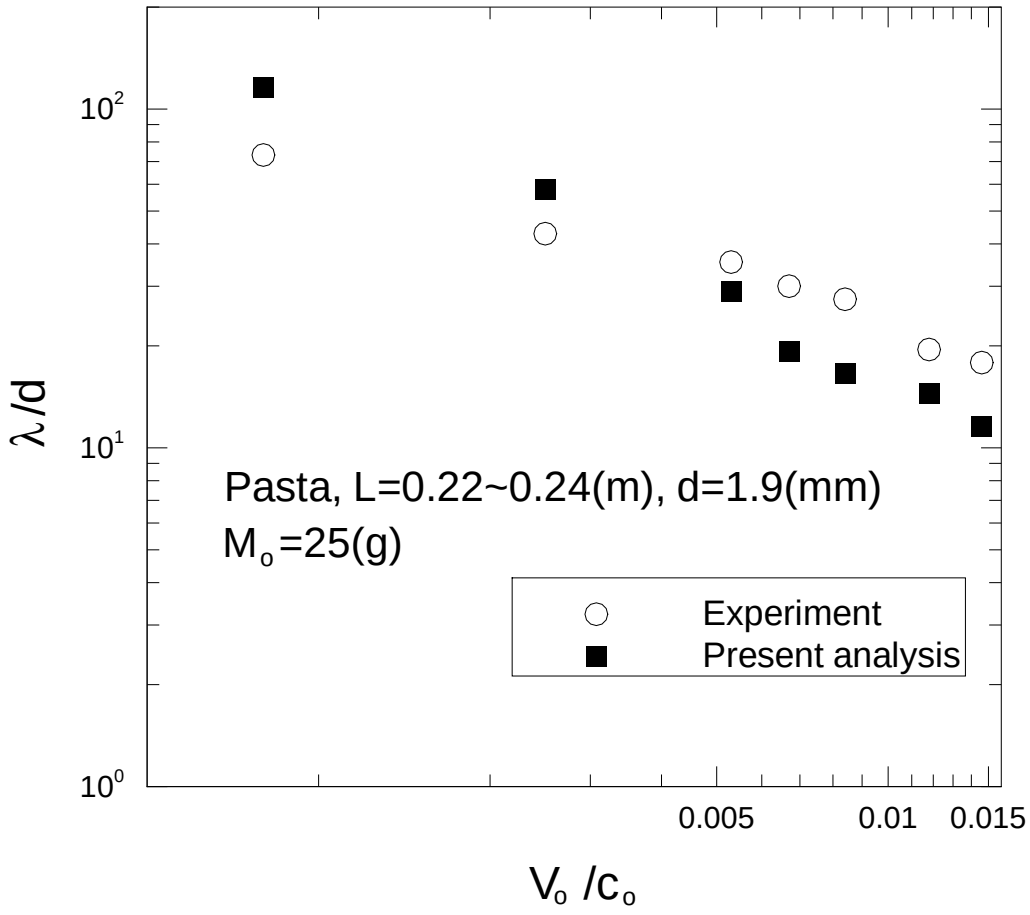

Figure 4.6: Comparison of the predicted critical wavelength from the present analysis against experimental results for a pasta beam

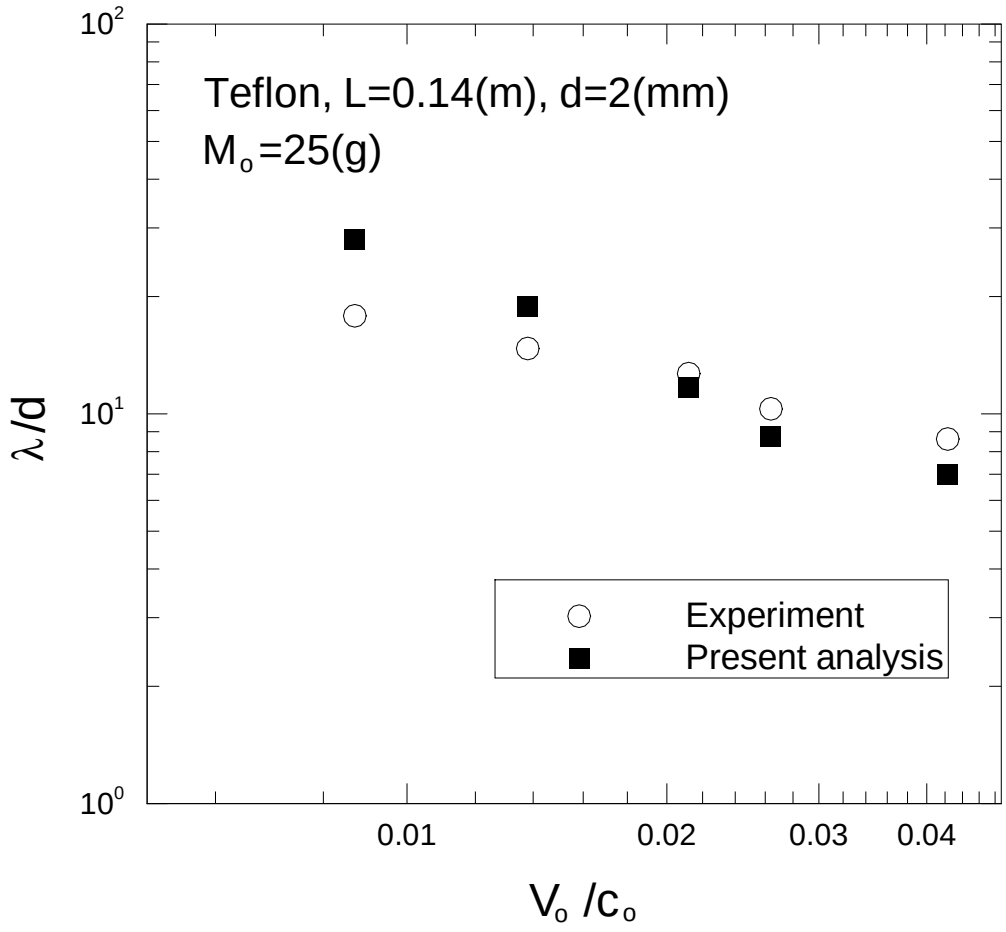

Figure 4.7: Comparison of the predicted critical wavelength from the present analysis against experimental results for a teflon beam

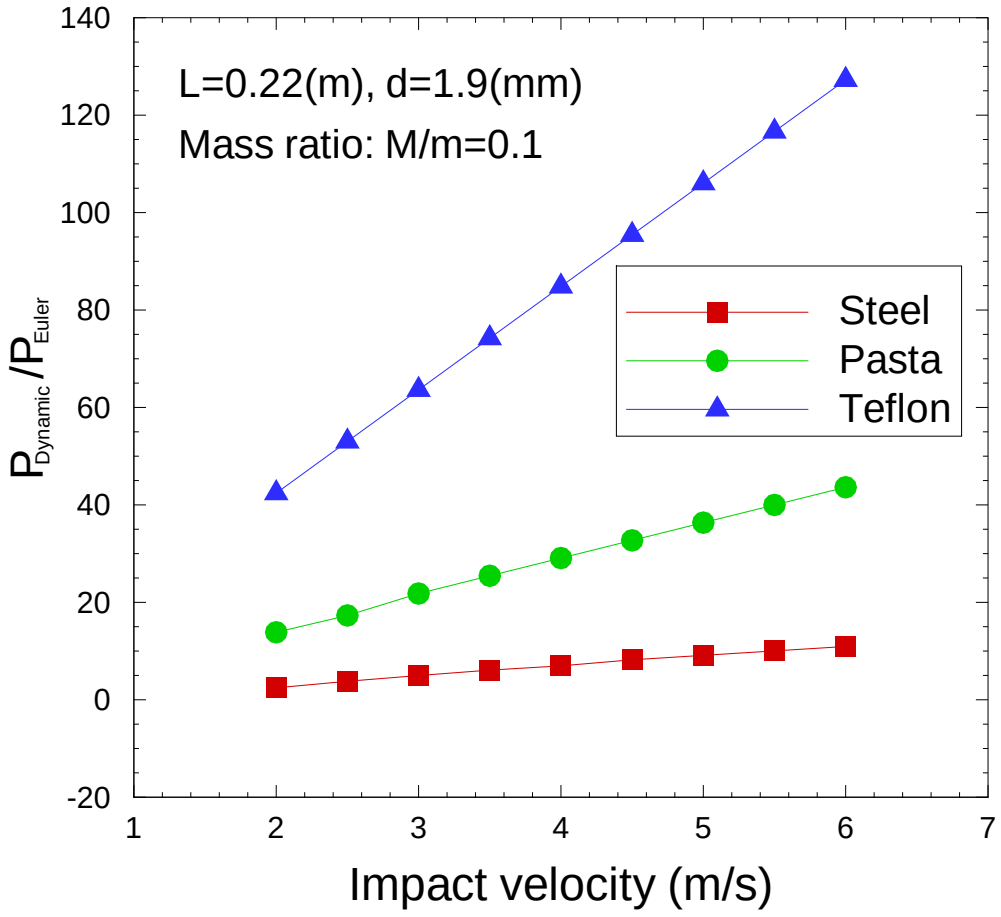

Figure 4.8: Dynamic buckling loads of various materials as a function of the impact velocity

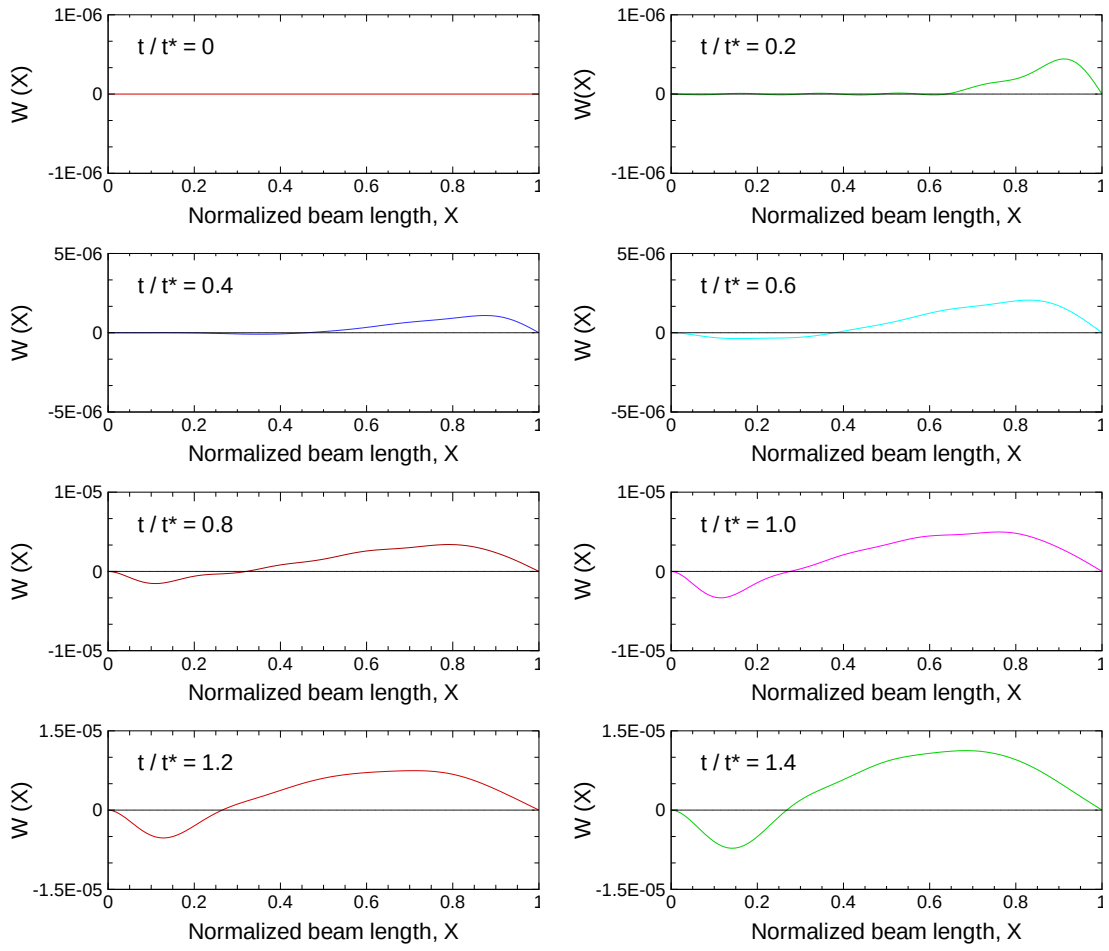

Figure 4.9: Growth of the beam deformation as time develops

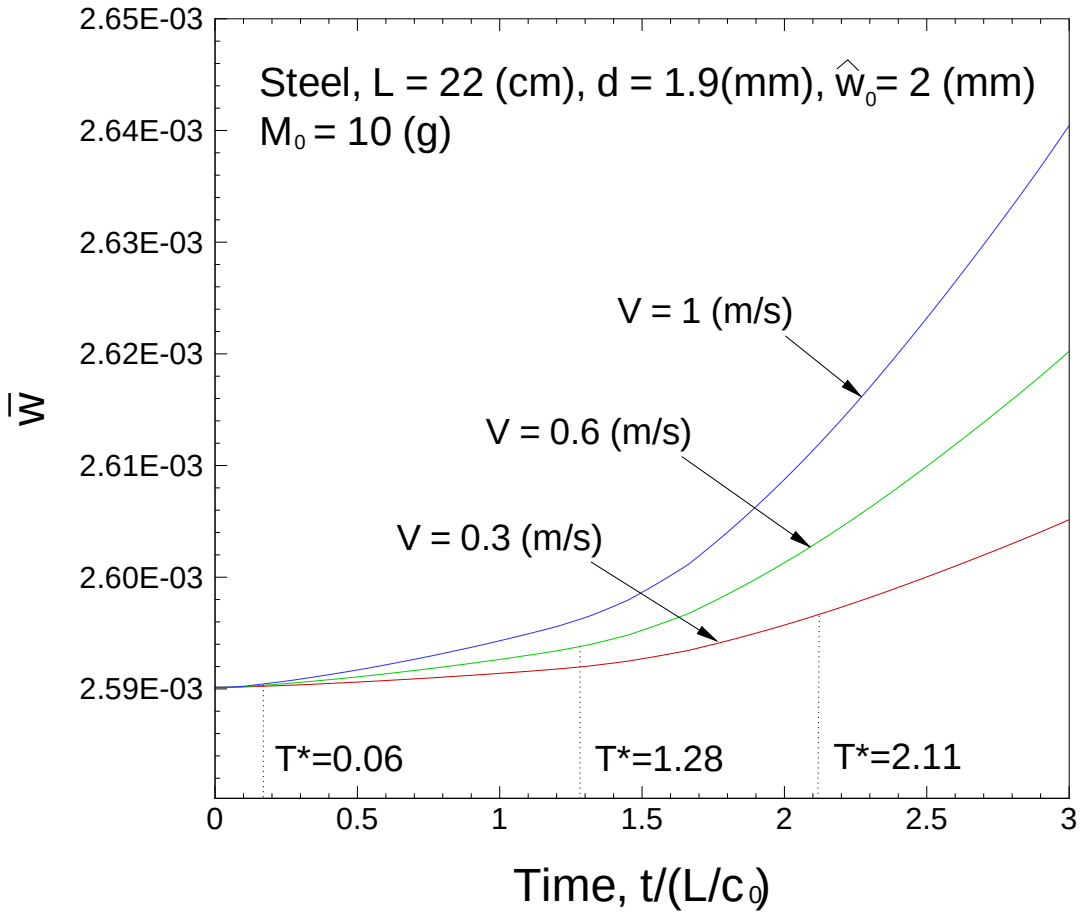

Figure 4.10: Deformation of the beam as a function of time with different impactor velocities

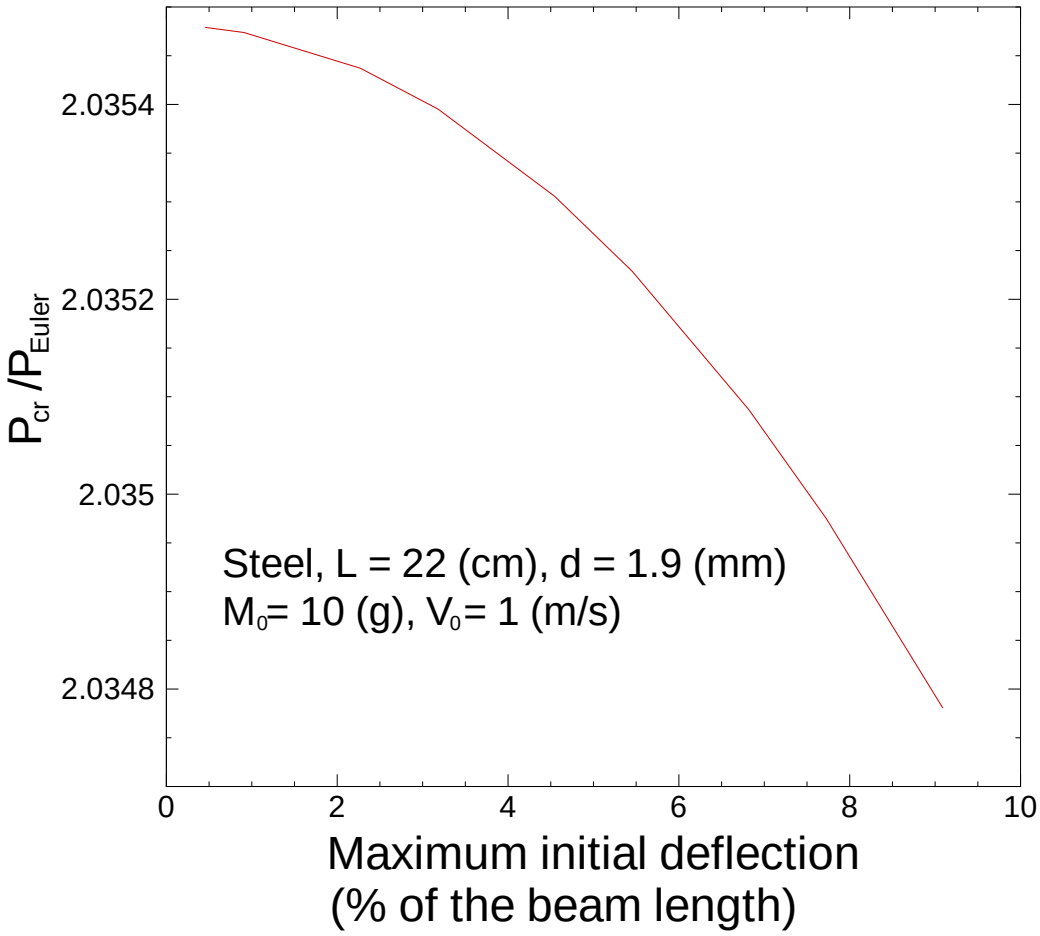

Figure 4.11: Dynamic buckling load as a function of the initial maximum deflection

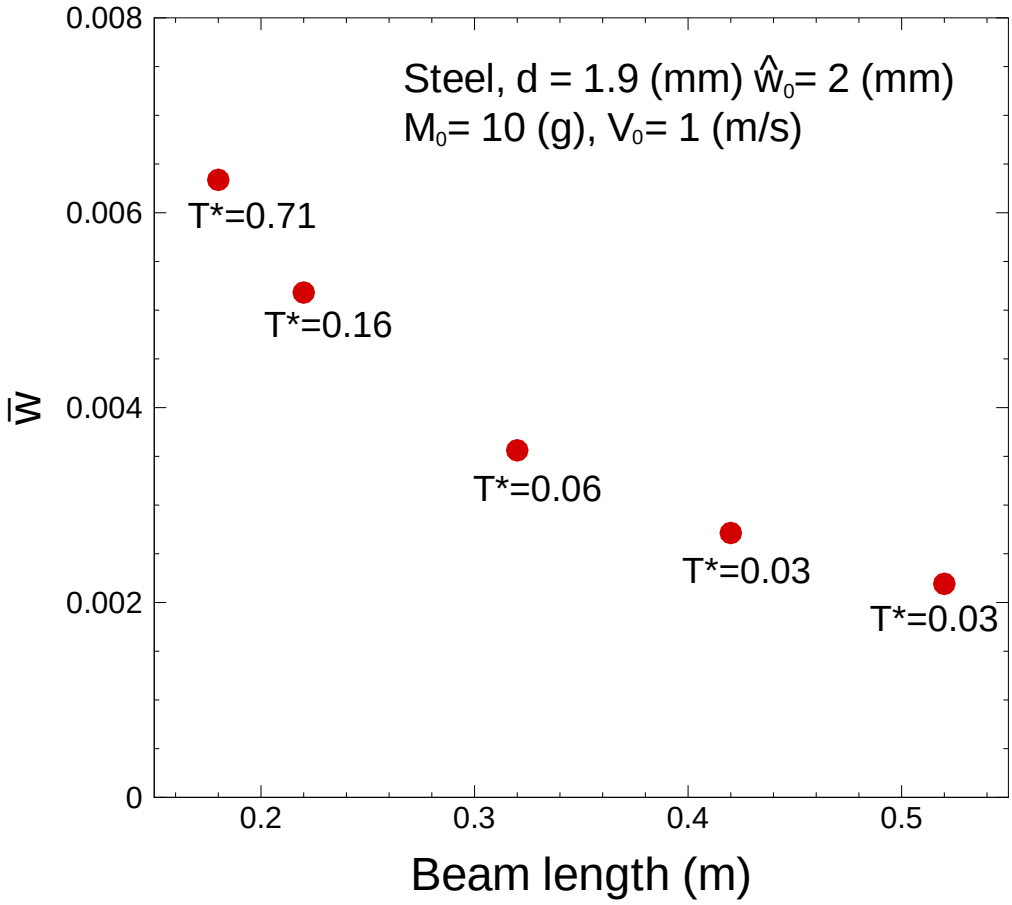

Figure 4.12: Deformation of the beam at the critical time as a function of the beam length

CHAPTER V

Experimental investigation of the static response of a sandwich structure under uniaxial compression

5.1 Introduction

The sandwich structure is composed of two thin, stiff, and strong face sheets covering a thick, light, and weaker core. The combination of the two different materials that are bonded to each other creates useful and unique structural advantages. The major advantage of the sandwich structure is very high stiffness and strength to weight ratios, due to the high axial stiffness of the face sheet separated by the light and relatively soft core. Since the core has typically lower density than metals, the sandwich structure can enhance the flexural rigidity of a structure without adding substantial weight to the structure. With various advantages given by this sandwich design, sandwich structures have been widely used in various applications specifically where the high stiffness per unit weight is greatly required.

The sandwich structure overcomes some drawbacks of the corresponding monolithic structure with the sandwich concept giving better structural performance for a specific application. However, load carrying sandwich structures show different response behavior due to the combination of multiple constituents. Especially, the sandwich structure under end compression exhibits peculiar failure behaviors, not encountered in homogeneous materials. Various failure modes may appear depend-

ing on the vast choices of material and geometric properties for the face sheet as well as the core. While the long and slender sandwich column is still susceptible to global instability, the sandwich structure can also fail by local instabilities in various ways. If the face sheets are made of laminated composites, a sandwich structure can also fail due to fiber microbuckling at the fiber/matrix scale.

The various failure modes of sandwich structures under end compression are examined experimentally in this chapter. The thickness of the core and the sandwich column length are the major variables for studying a collapse "map" of the sandwich structure subjected to uniaxial compressive loading. Theoretical analysis is also performed to predict the mechanical behaviors of the structure and compared against the experimental results. Finite element analysis is used to simulate the compression tests for comprehensive understanding of the sandwich structure failure mechanism.

5.2 Theoretical analysis of the sandwich column failure in uniaxial compression

Consider a sandwich column of gage length L with a face sheet thickness t^f and a core thickness t^c as shown in Fig. 5.1. The sandwich column is clamped at both ends and subjected to uniaxial compressive loading. The sandwich column may experience global or local instability due to the uniaxial load, resulting in the significant loss of load carrying capability of the structure. The sandwich column may also be collapsed by the failure in one of the constituents in micro mechanical scale before the macro instability develops. The mechanics of the compressive response of the sandwich structure is a consequence of competing multiple failure modes such as global buckling, local buckling, or face sheet micro buckling. This complex failure mechanism of the sandwich column are mainly caused by the combination of two different materials, unlike a corresponding monolithic column. The monolithic beam

is prone to be failed by Euler buckling mode under compression, while various failure modes are possible for the sandwich column as shown in Fig. 5.2.

Fig. 5.2(a) shows global buckling failure mode of a sandwich column, when the column is very long and slender. The global buckling mode can also be found for a very short sandwich column, and the instability is governed by the transverse shear deformation of the core. Local instability of the face sheet with short waves, known as wrinkling, is another candidate for the failure modes of the sandwich column as shown in Fig. 5.2(b). Wrinkling is usually found for a sandwich column with a thick core having lack of lateral support, since the large thickness of the core prevent the two face sheets from interacting each other for global deformation. In addition to the two macrobuckling modes, compression failure of the face sheet due to microbuckling of the fibers can occur when the axial stress in the face sheet reaches its maximum strength before the macrobuckling stresses develop. The compression failure of the face sheet should be considered carefully since the face sheets is much stiffer than the core and the compressive load is almost carried by the face sheets only.

The failure mechanism of the sandwich in compression is best described in Fig. 5.3, where the critical failure stresses are plotted against the sandwich column lengths. The theoretical buckling stress profiles are calculated by the analysis presented in Chapter II. The face sheet microbuckling stresses can be obtained from compression tests of the sandwich columns. Fig. 5.3(a) assumes that the face sheet microbuckling stress is smaller than theoretical wrinkling stress. Consequently, the sandwich column is susceptible to compression failure of the face sheet in a certain range of the column length, before global buckling becomes dominant collapse mode for the longer sandwich column. When the transverse normal stiffness of the core becomes weaker, the wrinkling stress may appear in a certain range of the column length as

shown in Fig. 5.3(b). The global buckling mode may occur when the column length is very large or shorter than the wrinkling wavelength as indicated in Fig. 5.3(b). The microbuckling failure is also expected for a very short sandwich column. Fig. 5.3(c) shows the failure map of a sandwich column with a thin core. The column behaves like a whole monolithic beam and the global buckling is dominant failure mode where the global buckling stress is smaller than the microbuckling stress.

In the following sections, sandwich columns subjected to uniaxial compressive loading will be experimentally examined with a variance of the column length and the core thickness. The various failure modes and corresponding critical stresses of the sandwich columns will be studied using the experimental data. The experimental results will be compared against the theoretical predictions from the present analysis.

5.3 Experimental setup

5.3.1 Material properties of the face sheet and the core

The sandwich panels experimentally examined here consisted of carbon/epoxy laminate face sheets over polyurethane foam cores. Two types of sandwich panels were manufactured with a 12.5 mm thick core and a 25 mm thick core, using resin transfer molding (RTM) at the University of Utah[1]. The geometrical and material properties of the face sheets are identical for the two types of sandwich panels.

The core material was made from a closed-cell polyurethane foam of density 160 kg/m^3. The product name of the core is LAST–A–FOAM FR–6710. Mechanical properties of the core are found in the published data sheet by the manufacturer [16]. The Young's modulus of the core is 89 MPa and the shear modulus is 19.5 MPa. Uniaxial compression test on the rectangular block of the core (25mm $\times$ 25mm $\times$ 38mm) was performed to obtain the inelastic behavior of the core. The

[1]We are grateful to Prof. Dan Adams of the Mechanical Engineering Department at the University of Utah for supplying they sandwich panels at a reasonable cost

stress-strain curve from the compression test is plotted in Fig. 5.4.

The core is covered by the face sheets comprising four plies of the T300B–3K plain weave carbon fiber fabric impregnated with the Epon 862 epoxy. The four layers were stacked in a [0/90/0/90] pattern. The measured average thickness of the face sheets removed from the sandwich panels was 1.0 mm. Tension tests were performed on three replicate specimens to obtain the uniaxial Young's modulus and the Poisson's ratio. Since the stacking sequence and the geometry of the woven fabric are balanced, the properties of the face sheet in the longitudinal and the transverse directions are the same. The measured Young's modulus of the face sheet was 48.1±4.0 GPa and the Poisson's ratio was 0.21.

5.3.2 Compression testing of sandwich specimens

The sandwich specimens were cut from the panels using a circular saw. Three groups of specimens with the gage length of 25 mm, 100 mm, 180–200 mm were tested. All specimens had a width of 61 mm. Both ends of the specimens were clamped by steel grips with plastic steel putty to constrain end rotations (effectively, clamped condition). While the epoxy adhesive was cured, the specimens were mounted on a fixture to keep the sandwich columns straight. Strain gages were bonded at the middle length of the front and back surfaces of the specimens. Parallel lines were marked on the core transversely as an indication of the specimen deformation during compression tests. The configuration of the prepared sandwich specimens is illustrated in Fig. 5.1.

The specimens were axially compressed by a hydraulically driven testing machine at the rate of 0.01 mm/s. The end displacement of the specimens during compression were measured by averaging the displacements from two linear voltage displacement transducers (LVDT) installed at the right and the left side of the specimens. The

strains of the specimens were measured by the strain gauges attached at the middle length of the front and the back surfaces of the specimens. The compressive load applied to the specimens was measured from a load cell mounted to the test machine. A high speed camera with a framing rate of 25 frames per second and a digital single–lens reflex camera were used to obtain deformation images of the specimen during the tests and post-mortem.

5.4 Results and discussion

The summary of end compression tests is reported in Table 5.1 and Table 5.2, for the sandwich specimens of the 12.5 mm thick core and the 25 mm thick core, respectively. The observed failure modes of the shortest specimens was the compression failure of the face sheet. Since the short column length restrains the evolution of global or local instability, and alleviates geometrical misalignment effects enhanced with a longer length, the shortest specimens can be considered to undergo axial compression with negligible bending deformation. Therefore, the failure loads of the 25 mm length specimens correspond to the ultimate (maximum) strength of the sandwich specimens. Since the load carried by the core is negligible, the compression failure load of the sandwich column can be written as

$$P_{fail} = 2X_C^f b t^f \tag{5.1}$$

where P_{fail}=failure load of the sandwich column, X_C^f=compressive strength of the face sheet, b=width of the sandwich column, and t^f=thickness of the face sheet. Thus, the ultimate compressive strength of the face sheet can be calculated from the average failure load of the shortest sandwich specimens. The compressive strength of the face sheet will be used as a microbuckling failure stress in the present analysis and the value of the strength is 250 MPa. Face sheet microbuckling failure was also

observed by Fagerberg [19] during his experimental study.

The responses of the 12.5 mm thick core sandwich specimens in the compression tests are shown in Fig. 5.5. The end-shortening displacements are normalized by the column length. All the specimens show linear load-displacement behaviors until the sandwich columns collapsed at the peak loads. The maximum loads decrease as the specimens become longer, that may be caused by the enhanced bending deformation effect since the longer specimen is more sensitive to the geometric imperfection.

In Fig. 5.5, the shortest specimens failed by face sheet compressive failure while the failures of two other specimens were triggered by global buckling. The growth of global buckling modes for the 100 mm and 180 mm long specimens are shown in Fig. 5.6 and Fig. 5.7, respectively, taken from the high speed camera. In the pictures, the specimens were initially straight and started to deform as the applied load increased. The deformed modes initiated the collapses of the whole sandwich specimens. The high speed camera were used because the energy release rate was too fast for a typical digital camera to take pictures sequentially from the global deformation to the collapse.

The global buckling failure mode is quantitatively illustrated in Fig. 5.8, showing the typical response of the bending strain of the specimen as the applied load increases. The bending strain is calculated by averaging the difference of two strain data obtained from the strain gages attached at the middle length of the front and the back surfaces of the specimen. The bending strain is initially negligible but starts to increase dramatically when the applied load reaches a certain value, where the specimen experiences global out-of-plane buckling deformation. Fig. 5.8 confirms once again that the failure of the 12.5 mm thick core sandwich specimen is induced by the global buckling.

The compressive responses of the 25 mm thick core sandwich specimens are shown in Fig. 5.9. Similarly, all the specimens show linear load-displacement behavior until the sandwich columns collapse at the peak loads. Decrease of the maximum load carrying capability along with the beam length resembles the results from the thin core sandwich specimens. However, all the specimens in Fig. 5.9 failed by the face sheet compressive failure at the peak loads. The typical failure sequences are shown in Fig. 5.10 and Fig. 5.11, for the 100 mm specimen and 200 mm specimen, respectively. In this image, one of the face sheets failed first when the maximum stress in the face sheet reached its ultimate strength. Since the broken face sheet lost its load carrying capability and the core was very weak in shear, the bending deformation progressed to the other face sheet, leading to its collapse. Fig. 5.12 describe the typical failure mechanism of the 25 mm thick core sandwich specimens in terms of the bending strain and the applied load. The bending strain shows negligible increase till the first face sheet fails. After the first face sheet fails, the bending strain shows dramatic change, that implies that the sandwich specimen experiences large rotational deformation because of the loss of balanced load carrying capability from the two face sheets and a weak core in shear.

5.5 Comparison with finite element analysis

Finite element (FE) analysis were performed using the commercial software package ABAQUS for comprehensive understanding of the failure mechanism of the sandwich specimens under edgewise compressive loading. The face sheets and the core were modeled as linear elastic 2D continua. Eight-noded quadratic plane strain elements (CPE8) were used for meshing both the face sheets and the core. The quadratic elements are preferred over four nodes linear elements since the higher order elements

are suitable for severe element distortions during the buckling deformation. Since the geometry and boundary conditions of sandwich column is symmetrical with respect to the normal surface at the middle length, only half length of the beam was modeled as shown in Fig. 5.13. A sufficiently fine mesh was used for the characteristic element lengths to be very small compared to the local buckling wavelength. The entire beam was uniformly strained from the left end, controlled by the axial displacement.

For the assessment of imperfection sensitivity on the compression response, the initial geometry of the sandwich model (25 mm long specimen) was perturbed by 0.6, 1.0, and 1.4 degrees in Fig. 5.14. The arc length method was used to perform the nonlinear geometric analysis to consider the possibility of an unstable equilibrium path. The inelastic material behavior of the core obtained in Fig. 5.4 was also employed for the nonlinear static analysis. Fig. 5.14 shows the load-end shortening responses with the peak loads indicated for each case. The load carrying capacity of the sandwich panel is weakened as the initial imperfection increases. Fig. 5.15 shows the result from the static FE analysis, compared against the experimental results. The FE computation with $\phi_0 = 0.75^\circ$ misalignment is agreeing very well with the experiential results. The peak load obtained in Fig. 5.15 will be compared with the experimental loads in Fig. 5.16. The linear eigenbuckling analysis was also performed for the 12.5 mm thick core sandwich columns to compare the predicted buckling loads against the experimental results. To estimate the reduction in the buckling load for the other two cases (100 mm and 180 mm length specimen), a similar imperfection sensitivity analyses were conducted. The results are indicated in Fig. 5.16 and they show that small misalignment ($\phi_0 = 0.2^\circ$ for L=100 mm, and $\phi_0 = 0.1^\circ$ for L=180 mm) reduces the buckling stress and brings it closer to the experimental value.

The critical stresses from the experiments, FE analysis, and the present analysis

are compared in Fig. 5.16. The experimental buckling stress is obtained when the bending strain experiences a dramatic escalation as shown in Fig. 5.8. The present analysis and the FE analysis ($\phi_0 = 0°$, perfect) overpredict the global buckling stresses compared to the experimental results. The present analysis computes the global buckling load assuming that the sandwich model is perfectly straight and linearly elastic. The geometric or material nonlinearity and the imperfections in specimens from manufacturing process may cause the discrepancies since the present analysis assumes that the materials are perfectly linear elastic, initially straight, and perfectly bonded to each other. Any perturbation to these factors will lead to the deterioration of the structural performances of the sandwich specimens, as was shown with respect to the initial misalignment ,ϕ_0, through the FE analyses. However, the computed buckling stresses are reasonably in good agreements with the experimental results. Furthermore, the present analysis successfully predicts the transition in the failure modes associated with the column length.

5.6 Concluding remarks

The compression failure mechanisms of sandwich specimens with various foam cores have been examined. The specimens were observed to display global buckling and face sheet microbuckling. The sandwich specimens with a thick core failed by microbuckling only since the stiffness from the thick core increased the resistance to global and local instabilities. The sandwich specimens with a thin core exhibited transition in the failure mode from microbuckling to global buckling as the column length becomes longer. The variables studied here, core thickness and column length, appears as important factors defining failure modes of the sandwich structures. The imperfection sensitivity on the prebuckling stiffness of the specimens were also ob-

served and verified by finite element analysis.

Length (mm)	Failure load(N)	Observed failure mode
25	31970	Face sheet failure
	30952	Face sheet failure
100	28232	Global buckling
	27929	Global buckling
180	24034	Global buckling
	24665	Global buckling

Table 5.1: Failure loads of the sandwich specimens with the 12.5 mm thick core from uniaxial end compression tests

Length (mm)	Failure load(N)	Observed failure mode
25	27692	Face sheet failure
	28995	Face sheet failure
100	24761	Face sheet failure
	26569	Face sheet failure
200	22045	Face sheet failure
	23782	Face sheet failure

Table 5.2: Failure loads of the sandwich specimens with the 25 mm thick core from uniaxial end compression tests

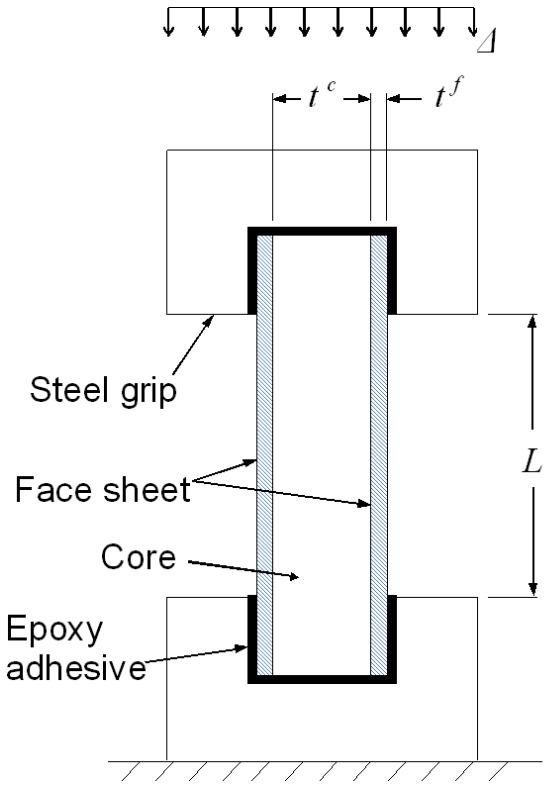

Figure 5.1: Configuration of a sandwich column uniaxially compressed at both ends

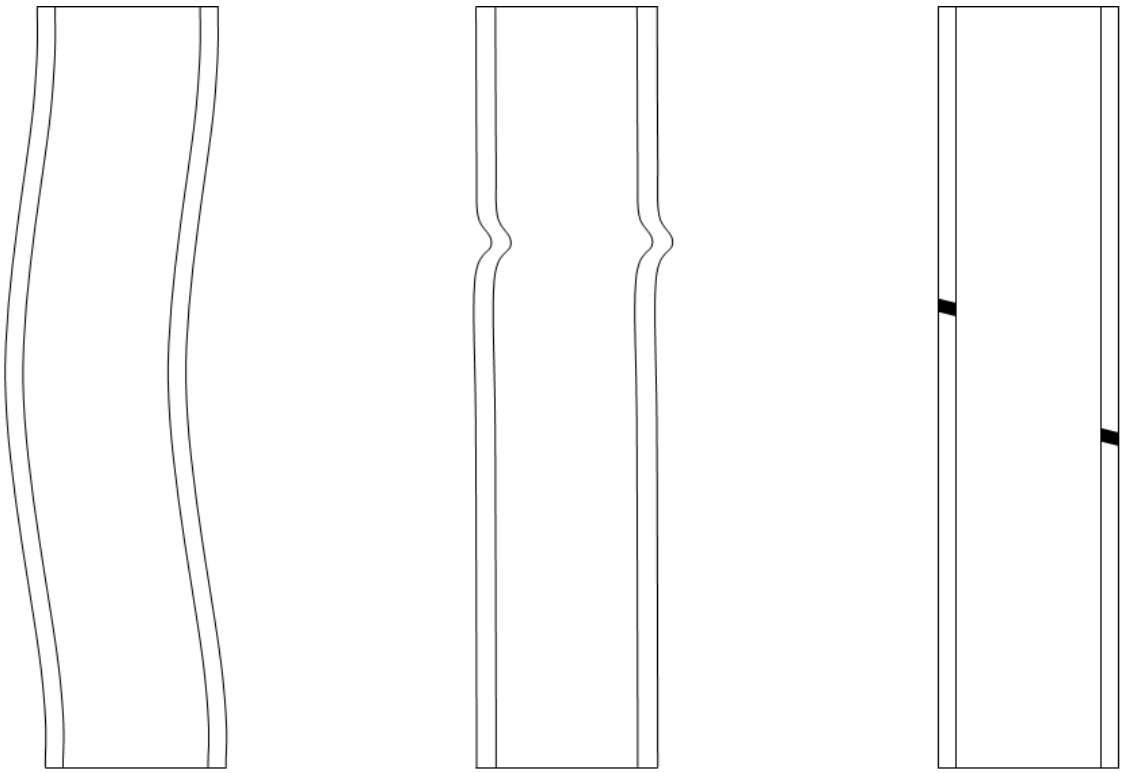

(a) Global buckling

(b) Wrinkling

(c) Face sheet microbuckling

Figure 5.2: Various possible compressive failure modes of a sandwich column under uniaxial compression

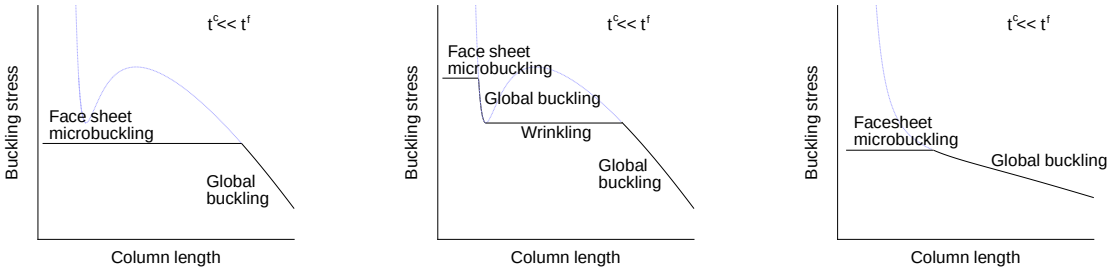

(a) microbuckling < wrinkling

(b) microbuckling > wrinkling

(c) thin core

Figure 5.3: Compressive failure mode maps of a sandwich column with a variance of the column length

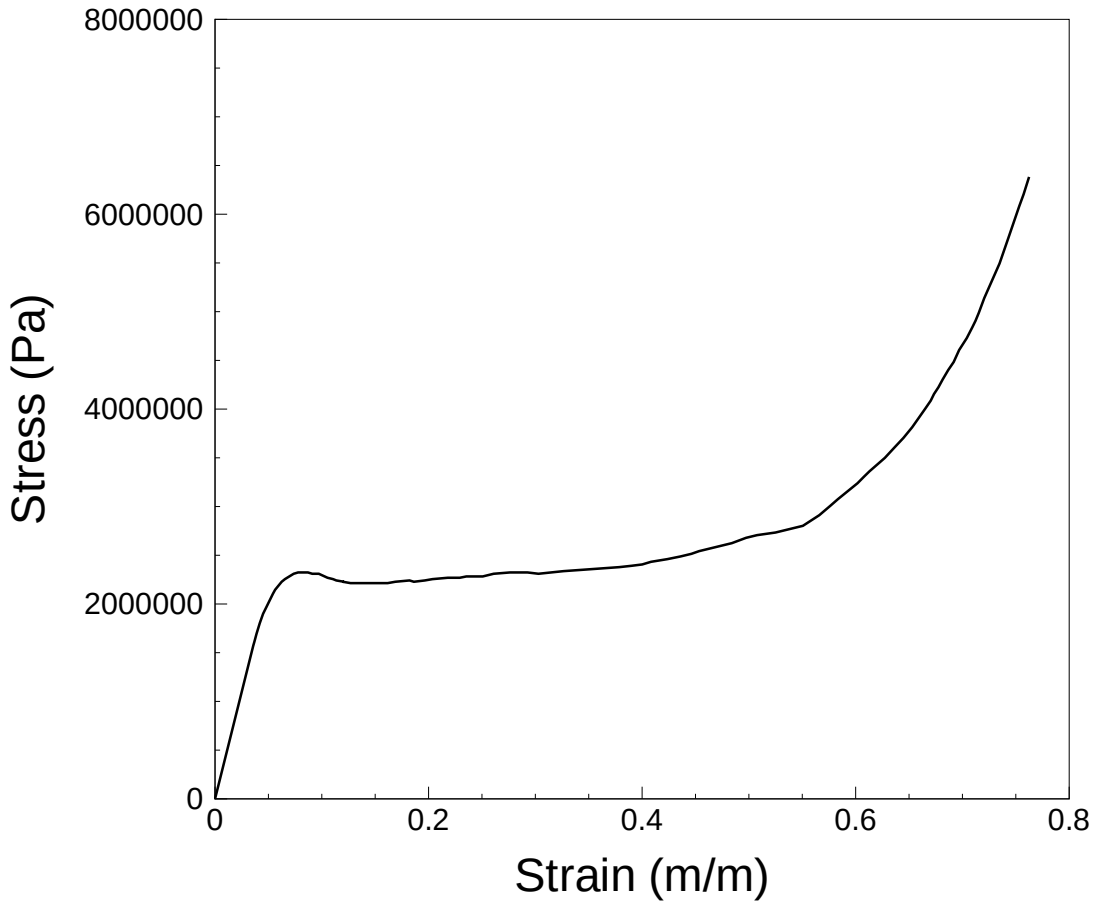

Figure 5.4: Nominal stress–strain curve from the compression test of the LAST–A–FOAM FR–6710 PVC foam core

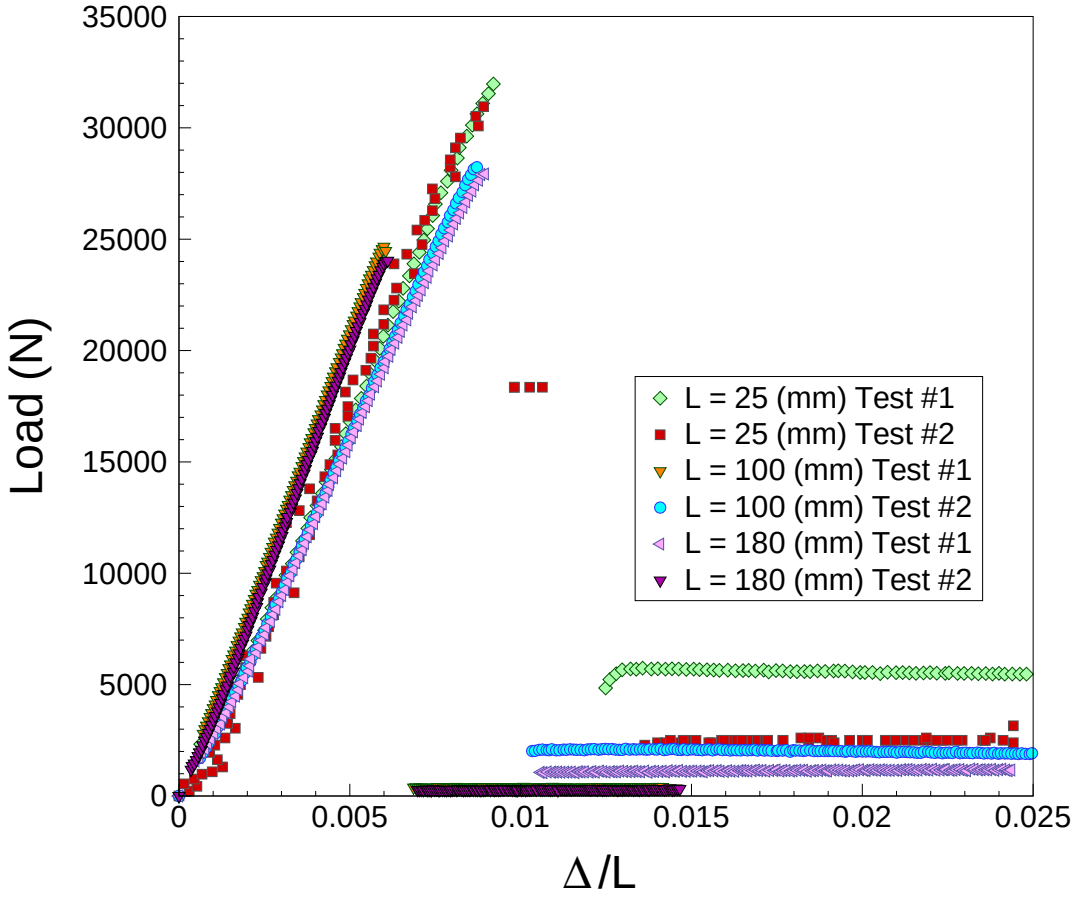

Figure 5.5: Response of sandwich specimens of a 12.5 mm thick core with a variance of the column length

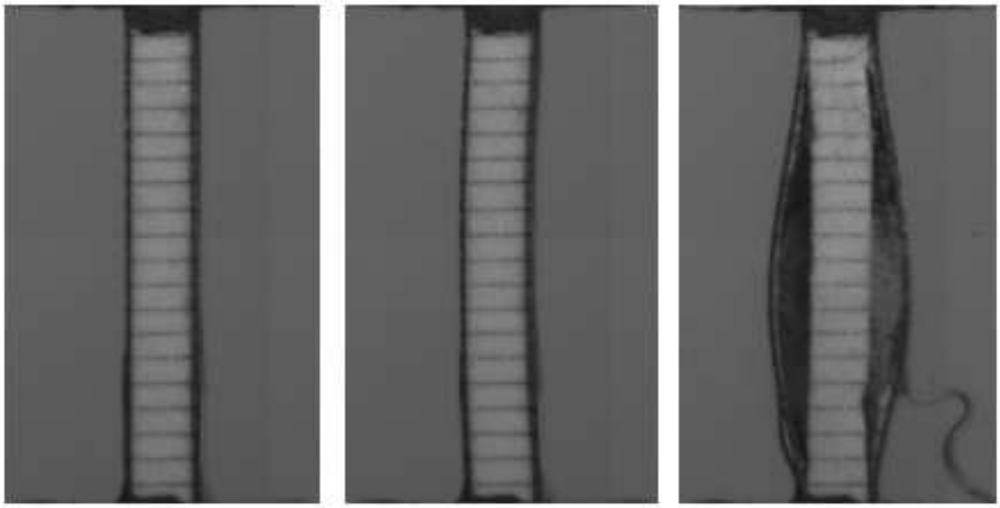

Figure 5.6: Buckling mode shape growth and failure of the 12.5 mm core sandwich specimen of L = 100 mm

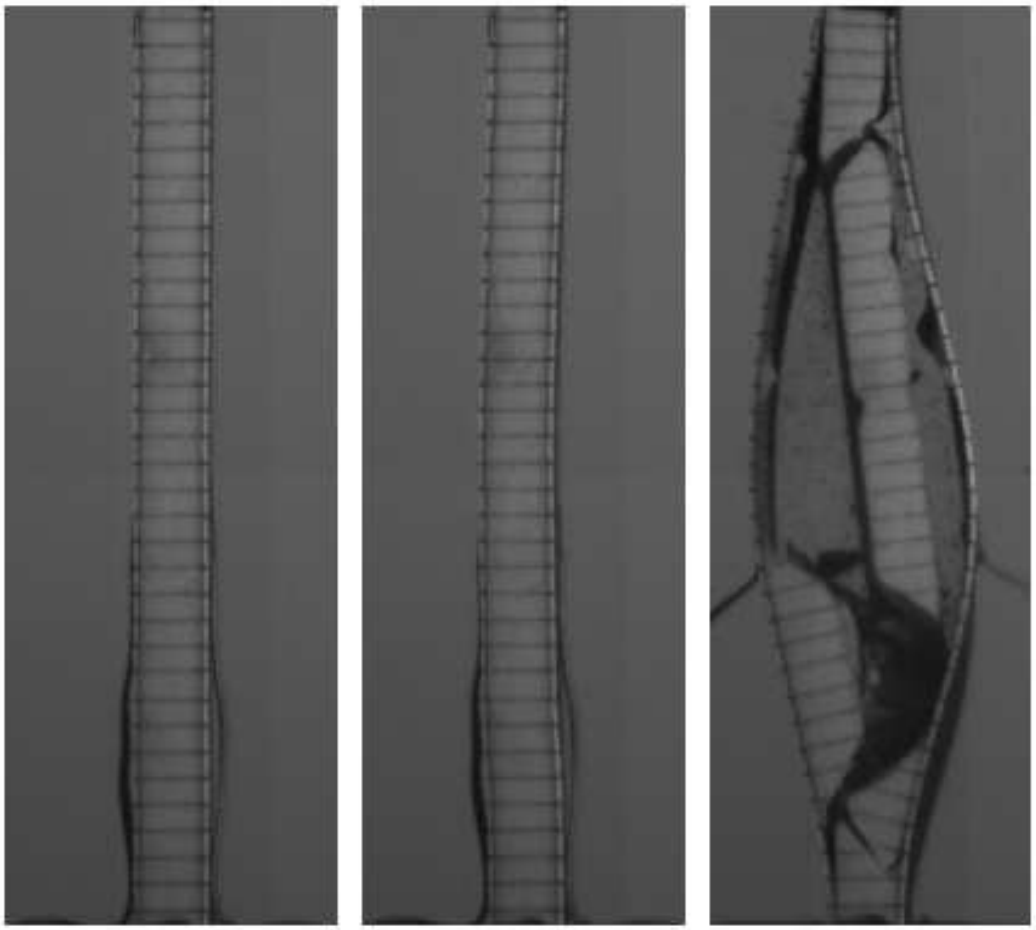

Figure 5.7: Buckling mode shape growth and failure of the 12.5 mm core sandwich specimen of L = 180 mm

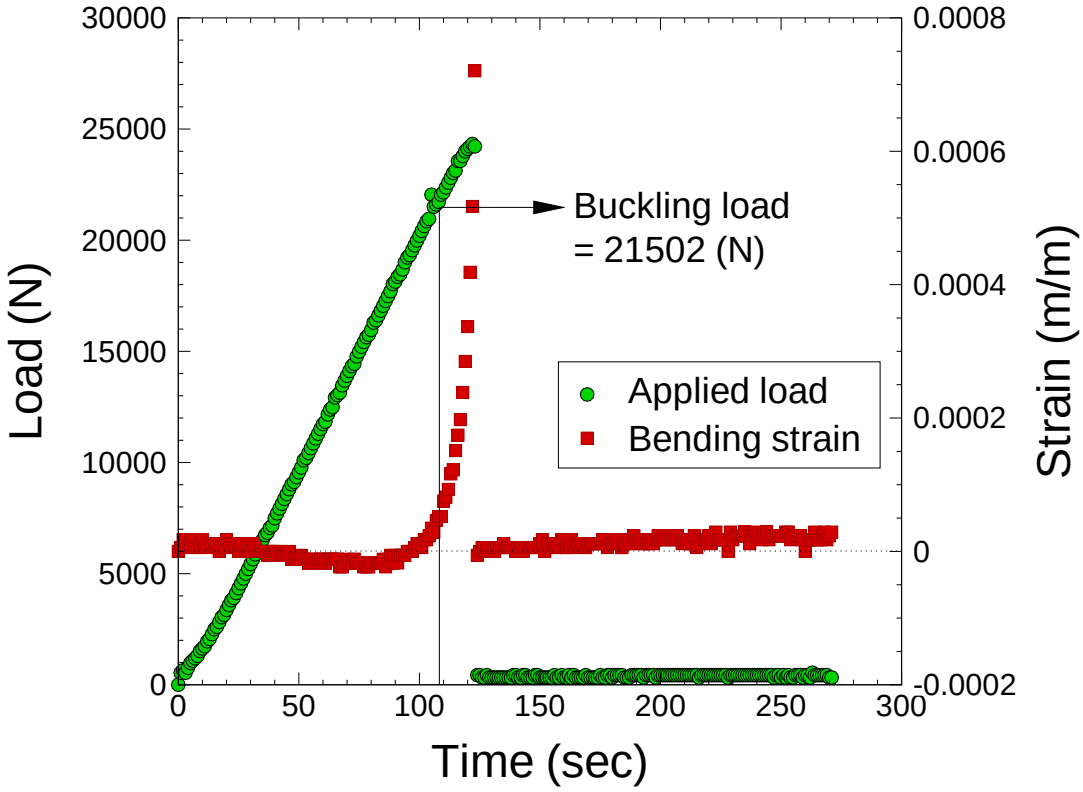

Figure 5.8: Applied load and the corresponding bending strain of the 12.5 mm thick core sandwich specimen. The buckling load is defined when the bending strain starts to diverge.

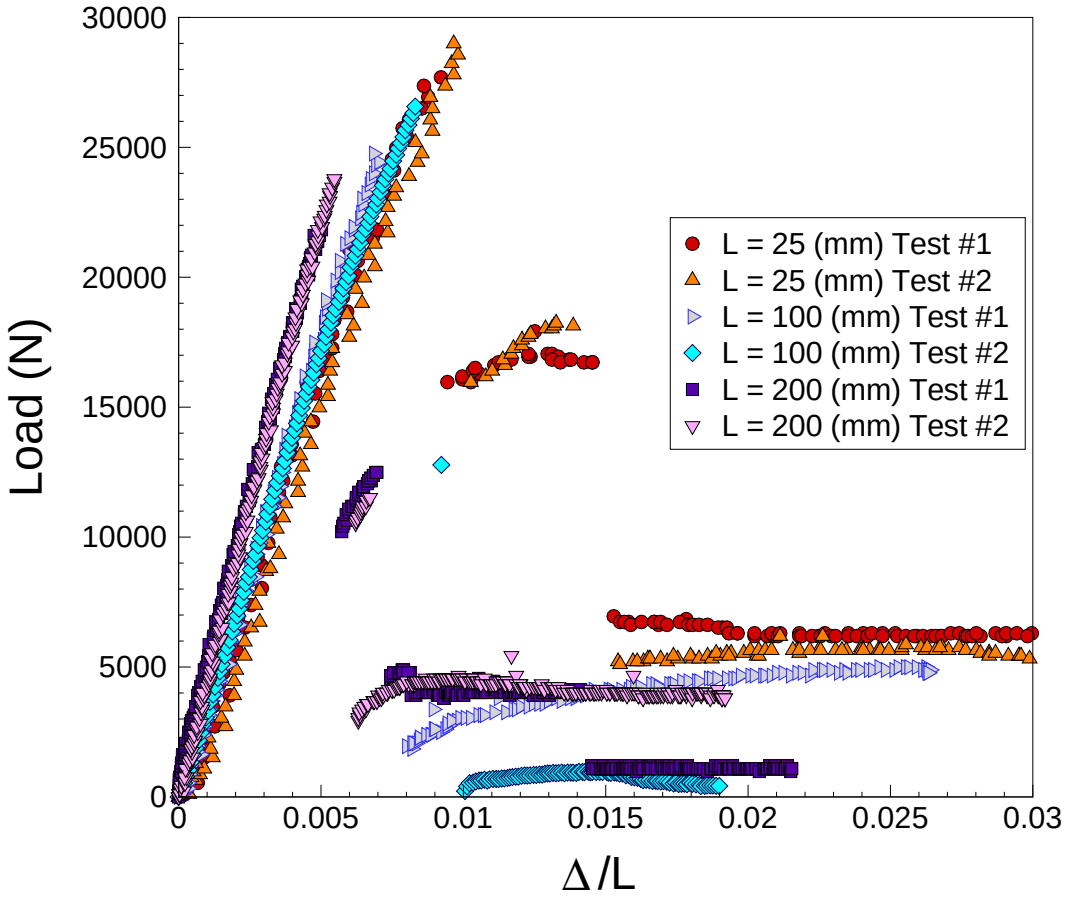

Figure 5.9: Response of sandwich specimens of a 25 mm thick core with a variance of the column length

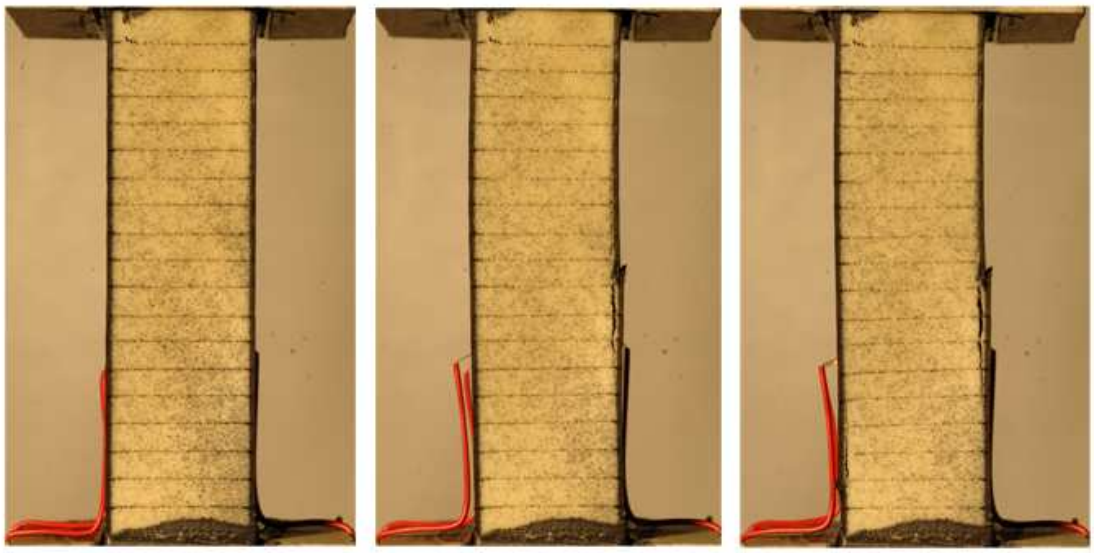

Figure 5.10: Face sheet failure of the 25 mm thick core sandwich specimen of L = 100 mm

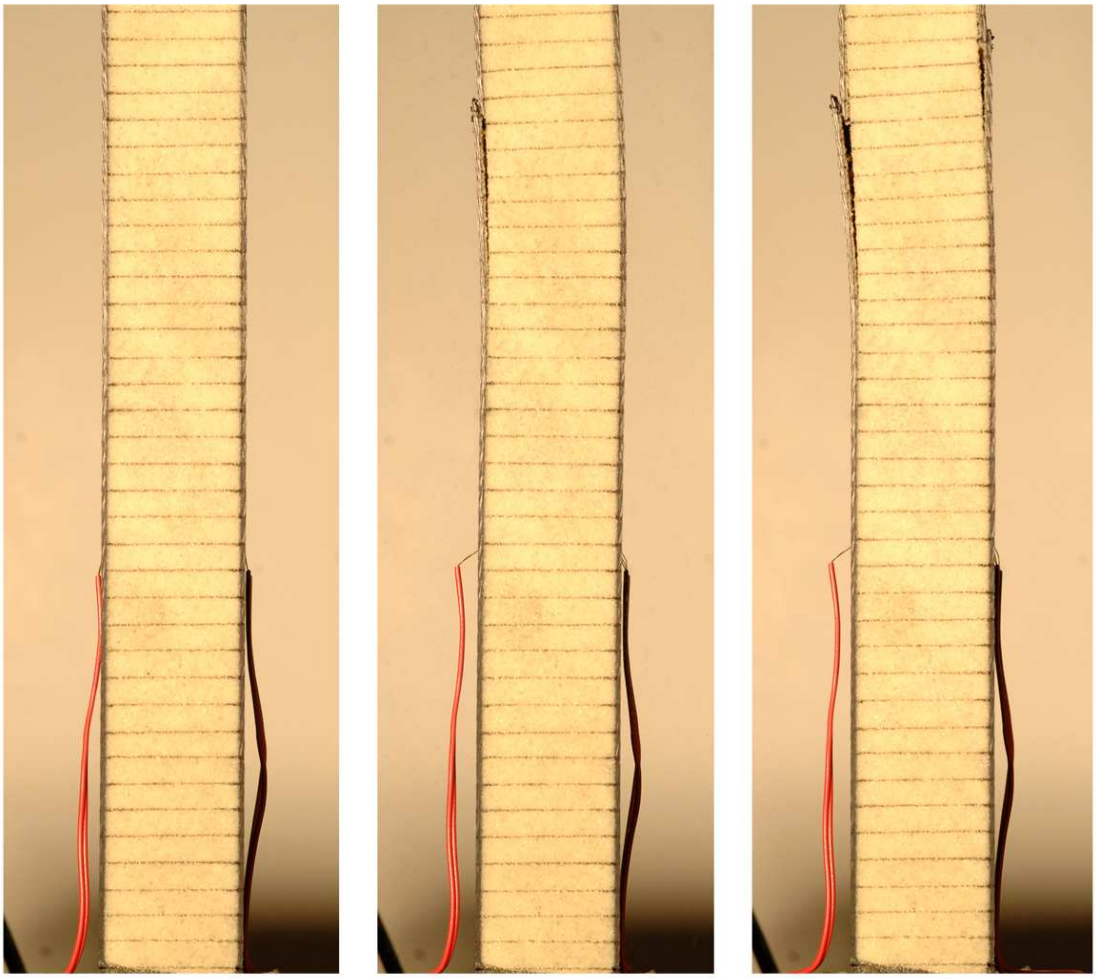

Figure 5.11: Face sheet failure of the 25 mm core sandwich specimen of L = 200 mm

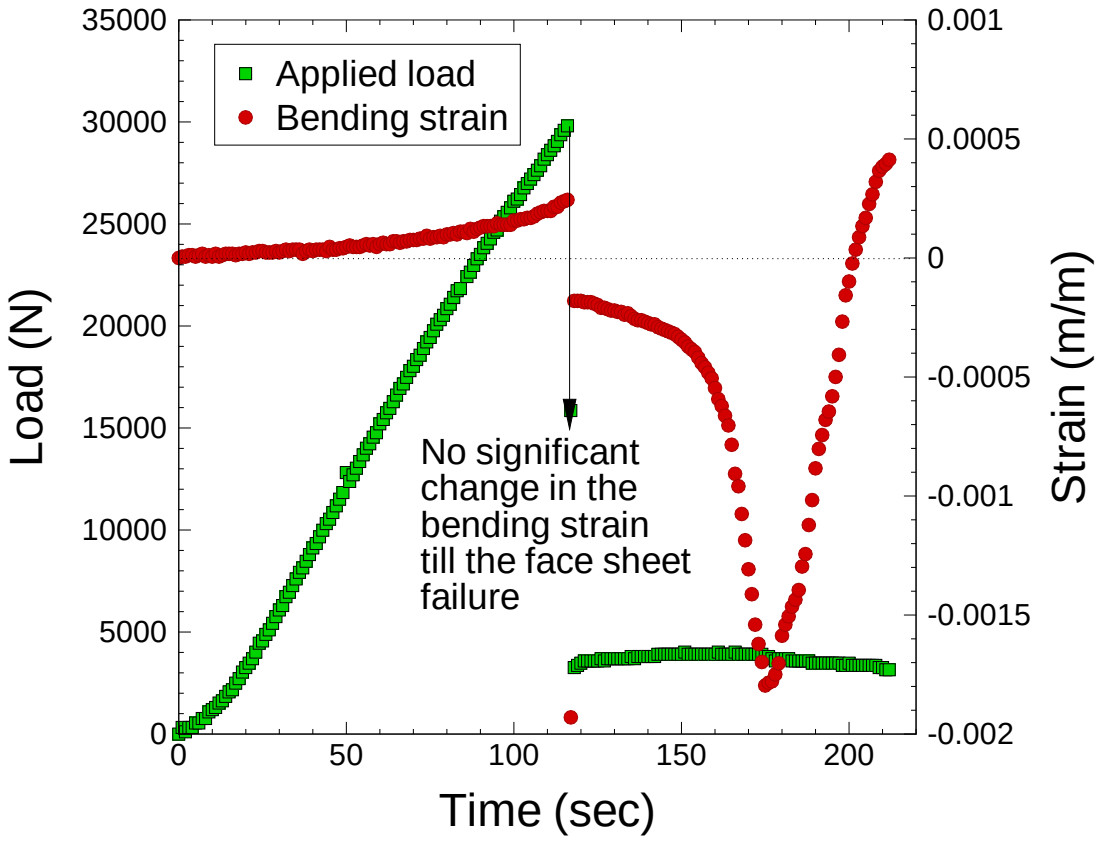

Figure 5.12: Applied load and the corresponding bending strain of the 25 mm thick core sandwich specimen. The bending strain shows insignificant increase until the first failure of the face sheet, implying that the sandwich specimen is failed by the compressive failure of the face sheet.

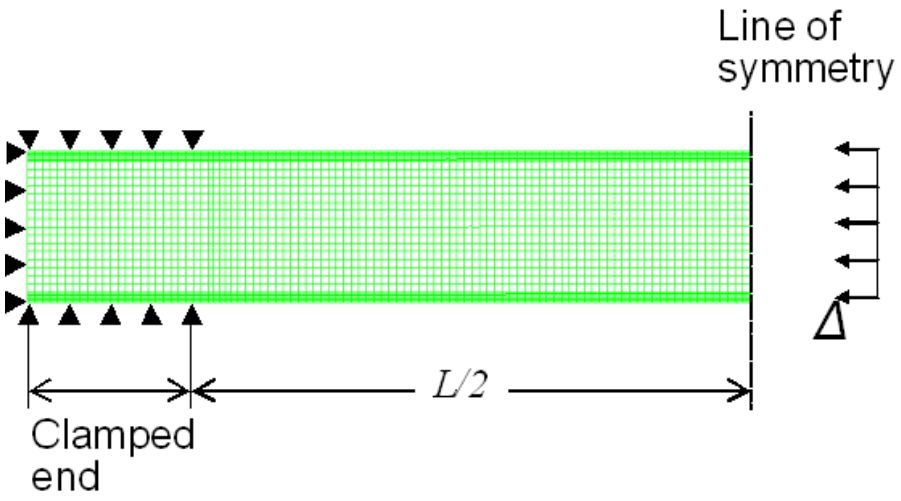

Figure 5.13: Configuration of the finite element analysis model

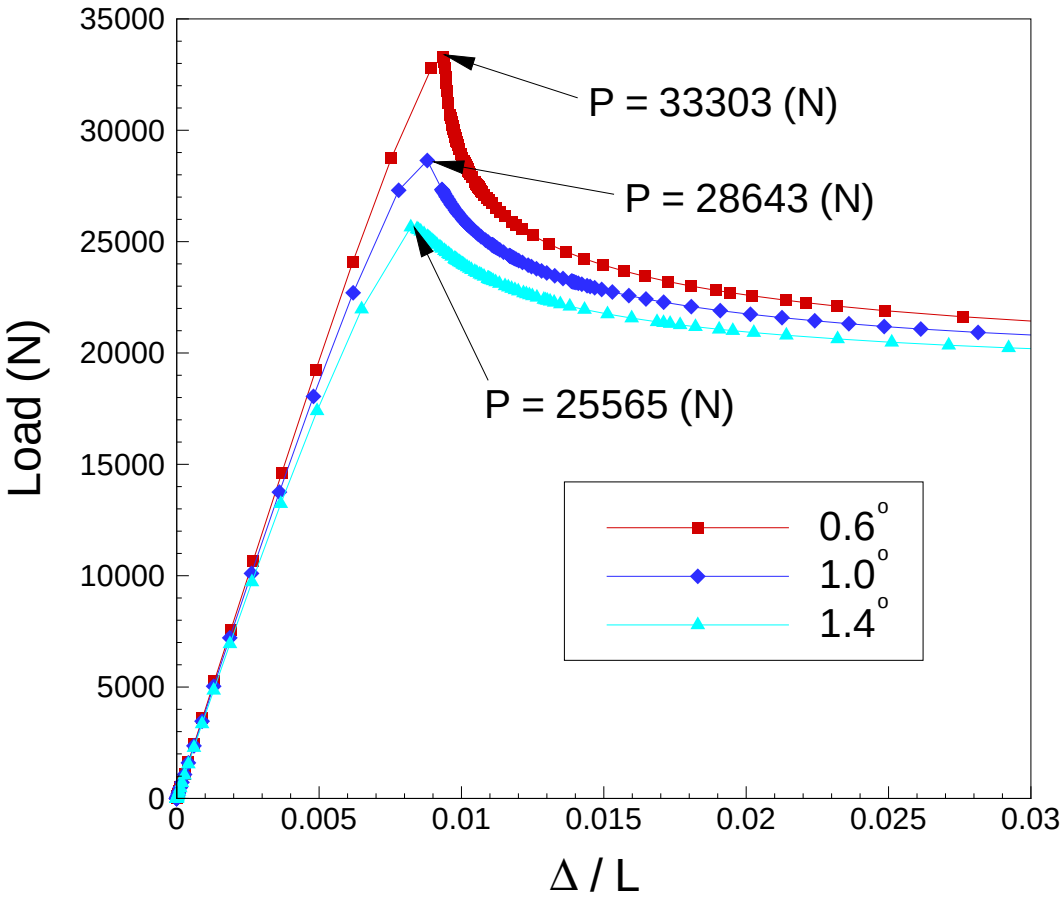

Figure 5.14: Weakened structural performance of the sandwich panel due to the initial imperfection

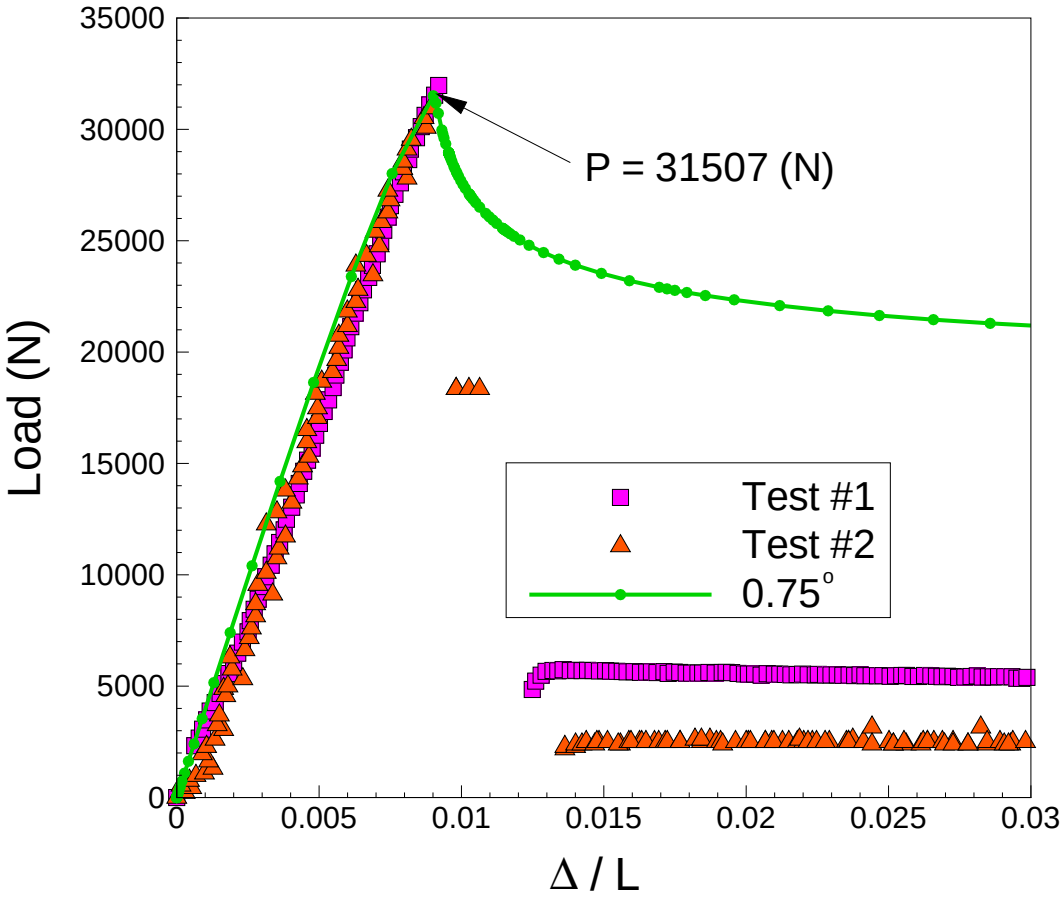

Figure 5.15: Compression responses of the 25 mm long sandwich column with the 12.5 mm thick core. FE computation with 0.75 degrees misalignment is in good agreement with the experimental results.

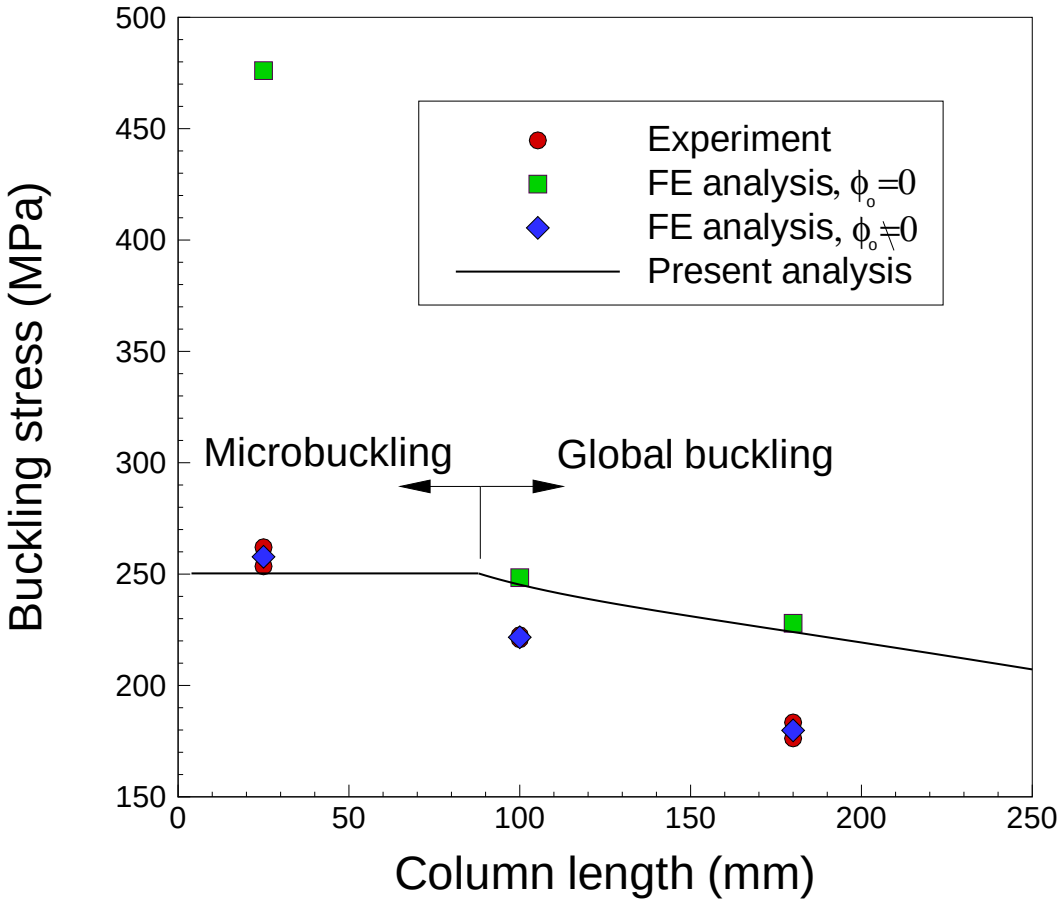

Figure 5.16: Comparison of the experimental critical loads against the results from the present analysis, FE analyses ($\phi_0 = 0$), and FE analyses ($\phi_0 \neq 0$)

CHAPTER VI

Dynamic failure of a sandwich structure subjected to an axial impact

6.1 Introduction

Sandwich structures in engineering applications are exposed to various loading configurations such as static, quasi-static, periodic, impulse, or a combination of two or three such loading scenarios. If the sandwich structure is compressively loaded, it is susceptible to global or local instability that may lead to the collapse of the structure. Static buckling problem of such structures has been studied theoretically and experimentally by many researchers. However, dynamic buckling or dynamic instability problem has not been received as much attention as the static counterpart.

Dynamic buckling problem of a simple Euler-Bernoulli beam has received the first attention by Koning and Taub [36]. They considered a initially crooked beam subjected to shock load. They assumed that the shock load is constant along the beam length neglecting the non-uniform axial strain distribution in time. The assumption of constant axial force along the beam length has been favorably accepted for investigation of dynamic buckling of a beam under axial impact loading [42, 17, 24]. The effect of the axial stress wave have been moderately studied [2, 32, 35, 56] while the beam is still assumed to have an initial geometric imperfection. Most of those theoretical studies defined dynamic buckling when a selective load parameter experience

a sudden change or transition in a response to the dynamic loading.

Dynamic buckling is an issue to any load-bearing structural elements such as beams, plates, and shells. When a slender beam is subjected to an impulsive compression load at one end, a compressive stress wave is generated and travels along the beam with a velocity of $c_0 = \sqrt{E/\rho}$, where E=Young's modulus of the beam and ρ=density of the beam. The stress wave becomes magnified by superposition of the incoming and reflecting waves. If the axial stress is developed sufficiently beyond a certain condition for dynamic buckling initiation, the beam starts out-of-plane deformation, which may lead to a significant mechanical failure.

Sandwich structures subjected to an axial impact is also susceptible to dynamic buckling. However, the development of the axial stress wave, that may cause dynamic buckling, is very different from that of the corresponding monolithic beam because of the combination of two different materials. If the sandwich beam has a large separation between the two face sheets, the face sheet can be modeled as a beam on an elastic foundation. If the core size is relatively small, the axial stress wave should be treated via finite element analysis, since the axial waves of each layer will not be separable and have interactions with each other.

In this chapter, conditions for dynamic bifurcation buckling are derived for a sandwich beam, considering the axial stress wave propagation along the beam length. The sandwich beam is modeled as a beam on an elastic foundation, assuming that the core provides large separation between the two face sheets and neglecting the interaction between the layers. In doing so, the axial wave propagation obtained in Chapter IV is employed to solve the transverse equation of motion. It appears that the equation of motion permits multiple non-trivial solutions at a critical time, similar to the result of the simple Euler-Bernoulli beam discussed in Chapter IV. When

there exists a critical time satisfying the bifurcation condition, dynamic buckling of an impacted beam is defined and the first instance at which this occurs is denoted as the buckling time of the sandwich beam.

Impact tests on the sandwich specimens are also performed with various configuration of the specimens. The experimental results are used to study the dynamic buckling growth of the sandwich beam. Finite element analysis is conducted to simulate the experimental impact responses of the sandwich specimens to the uniaxial compression. The experimental and numerical results will be compared in association with the analytical critical time.

6.2 Problem formulation

6.2.1 Bifurcation analysis: dynamic buckling of a sandwich beam

A sandwich beam studied here is modeled as a beam on an elastic foundation and is illustrated in Fig. 6.1. The elastic beam of length L is clamped at one end, while the other end is simply supported. The cartesian coordinate system in the xz–plane is assigned to the beam with u and w denoting displacements in the x and z directions, respectively. The beam is supported by a continuous series of springs that is analogous to the core material. The spring constant K_z is defined as

$$K_z = \frac{E^c b}{t^c/2} \tag{6.1}$$

where E^c=Young's modulus of the core, b=width of the beam, and t^c=thickness of the core. As pointed out in [9], the foundation constant K_z is a function of the wavelength of the deformation in x–direction. This aspect is considered for future work, since the assumption of a constant K_z on the predicted critical time to buckle requires further verification. At the time of submitting this thesis, the analysis with constant K_z was completed and these results are presented here.

The initially straight and vertical beam is impacted at $x = L$ by a rigid mass M with a velocity of V_0 at time $t = 0$. Neglecting the shear deformation effect of the beam, the two coupled governing equations of motion are written as

$$\frac{\partial^2 u}{\partial x^2} = \frac{1}{c_0^2}\frac{\partial^2 u}{\partial t^2} \tag{6.2a}$$

$$E^f I^f \frac{\partial^4 w}{\partial x^4} + \frac{\partial}{\partial x}\left[F(x,\, t)\frac{\partial w}{\partial x}\right] + K_z w + \rho^f A^f \frac{\partial^2 w}{\partial t^2} = 0 \tag{6.2b}$$

where $c_0 = \sqrt{E^f/\rho^f}$, E^f=Young's modulus of the beam, ρ^f=density of the face sheet, I^f=second moment of inertia of the beam, A^f=cross sectional area of the beam, and $F(x,\, t)$=resultant axial load due to the impact which can be expressed using the wave solution $u(x,\, t)$ as

$$F(x,\, t) = E^f A^f \frac{\partial u}{\partial x} \tag{6.3}$$

The initial conditions for the governing equations are

$$\begin{aligned} u(x,\, 0) &= 0 \\ \frac{\partial u(x,\, 0)}{\partial t} &= 0 \quad \text{for} \quad 0 \le x < L \\ \frac{\partial u(x,\, 0)}{\partial t} &= -V \quad \text{at} \quad x = L \end{aligned} \tag{6.4}$$

for the axial motion, and

$$\begin{aligned} w(x,\, 0) &= 0 \\ \frac{\partial w(x,\, 0)}{\partial t} &= 0 \end{aligned} \tag{6.5}$$

for the out-of-plane motion, respectively. The beam is considered to be fixed at $x = 0$, and simply supported at the impacted end, $x = L$. Consequently, the boundary conditions are

$$\begin{aligned} u(0,\, t) &= 0 \\ M\frac{\partial^2 u(L,\, t)}{\partial t^2} &= Mg - E^f A^f \frac{\partial u}{\partial x} \end{aligned} \tag{6.6}$$

where g=gravitational acceleration.

The solution to the equation of the axial motion is derived in Chapter IV and will be used to solve the out-of-plane equation of motion. Eq. (6.2b) can be solved following similar steps discussed in Chapter IV. The existence of the critical time, t^*, will be examined, associated with the emergence of a non-trivial solution $w_1(x,\, t) \neq 0$ satisfying Eq. (6.2b). If $w_0(x,\, t) \neq 0$ is the trivial solution to Eq. (6.2b) and $w_1(x,\, t) \neq 0$ is another solution along a bifurcated path, then, $w_1(x,\, t^* + \Delta t)$ must also satisfy Eq. (6.2b), when Δt is infinitesimally small. It follows that,

$$\frac{\partial^4 w_1(x,\, t^*)}{\partial x^4} + \frac{1}{\kappa^2}\frac{\partial}{\partial x}\left[\frac{\partial u(x,\, t^*)}{\partial x}\frac{\partial w_1(x,\, t^*)}{\partial x}\right] + \gamma^4 w_1(x,\, t^*) + \beta^4 \frac{\partial^2 w_1(x,\, t^*)}{\partial t^2} = 0 \tag{6.7a}$$

$$\frac{\partial^4 w_1(x,\, t^* + \Delta t)}{\partial x^4} + \frac{1}{\kappa^2}\frac{\partial}{\partial x}\left[\frac{\partial u(x,\, t^* + \Delta t)}{\partial x}\frac{\partial w_1(x,\, t^* + \Delta t)}{\partial x}\right] + \gamma^4 w_1(x,\, t^* + \Delta t) + \beta^4 \frac{\partial^2 w_1(x,\, t^* + \Delta t)}{\partial t^2} = 0 \tag{6.7b}$$

where κ=radius of gyration, $\gamma^4 = K_z/E^f I^f$ and $\beta^4 = \rho^f A^f/E^f I^f$. Using the Taylor series for expanding terms in Eq. (6.7b) and neglecting higher order terms after the expansion, Eq. (6.7b) can be reduced to

$$\frac{\partial}{\partial t}\Big[\frac{\partial^4 w_1(x,\, t^*)}{\partial x^4} + \frac{1}{\kappa^2}\frac{\partial}{\partial x}\left\{\frac{\partial u(x,\, t^*)}{\partial x}\frac{\partial w_1(x,\, t^*)}{\partial x}\right\} + \gamma^4 w_1(x,\, t^*) + \beta^4 \frac{\partial^2 w_1(x,\, t^*)}{\partial t^2}\Big]\Delta t = 0 \tag{6.8}$$

with the aid of Eq. (6.7a). Since $\Delta t \neq 0$, it follows that,

$$\frac{\partial}{\partial t}\left[\frac{\partial^4 w_1}{\partial x^4} + \frac{1}{\kappa^2}\frac{\partial}{\partial x}\left\{\frac{\partial u}{\partial x}\frac{\partial w_1}{\partial x}\right\} + \gamma^4 w_1 + \beta^4 \frac{\partial^2 w_1}{\partial t^2}\right] = 0 \quad \text{at} \quad t = t^* \tag{6.9}$$

Eq. (6.9) provides the condition to determine t^*. Eq. (6.9) can be further simplified in view of Eq. (6.7a) to finally yield,

$$\frac{\partial^4 w_1}{\partial x^4} + \frac{1}{\kappa^2}\frac{\partial}{\partial x}\left[\frac{\partial u}{\partial x}\frac{\partial w_1}{\partial x}\right] + \gamma^4 w_1 + \beta^4 \frac{\partial^2 w_1}{\partial t^2} = 0 \quad \text{at} \quad t = t^* \tag{6.10}$$

as the final condition to determine $t = t^*$.

Following the exposition in [9], a non-trivial solution to Eq. (6.10) is assumed in the form

$$w_1(x, t) = f(t)W(x), \tag{6.11}$$

with the D'Alembert substitution $f(t) = e^{i\Omega t}$, so that

$$w_1(x, t) = e^{i\Omega t}W(x) \tag{6.12}$$

Substituting Eq. (6.12) into Eq. (6.10) results in,

$$\frac{d^4W}{dx^4} + \frac{1}{\kappa^2}\frac{\partial}{\partial x}\left(\frac{\partial u}{\partial x}\frac{dW}{dx}\right) + \gamma^4 W = \Omega^2\beta^4 W \quad \text{at} \quad t = t^* \tag{6.13}$$

which is subjected to the clamped-simply supported boundary conditions,

$$\begin{aligned} W = 0 \quad \text{and} \quad \frac{dW}{dx} = 0 \quad \text{at} \quad x = 0 \\ W = 0 \quad \text{and} \quad \frac{d^2W}{dx^2} = 0 \quad \text{at} \quad x = L \end{aligned} \tag{6.14}$$

The solution to Eq. (6.13) is assumed to be

$$W(x) = \sum_{i=1}^{N} A_i\phi_i(x) \tag{6.15}$$

where A_i=constant and $\phi_i(x)$ are the eigenfunctions of a clamped-simply supported beam on the elastic foundation undergoing free vibration. Consequently, $\phi_i(x)$ satisfies the geometric and natural boundary conditions prescribed by Eq. (6.14). Using Eq. (6.15), the problem posed by Eq. (6.13) and Eq. (6.14) can be rewritten as,

$$\left[K_{ij} - P_{ij} + \Gamma_{ij}\right]\{A_j\} = \Omega^2\left[M_{ij}\right]\{A_j\} \tag{6.16}$$

where A_i=column vector consisting of the coefficients, and the K_{ij}, P_{ij}, and M_{ij} are defined as

$$K_{ij} = K_{ji} = \int_0^L \frac{d^2\phi_i}{dx^2}\frac{d^2\phi_j}{dx^2}dx \tag{6.17}$$

$$P_{ij} = P_{ji} = \frac{1}{\kappa^2} \int_0^L \frac{\partial u(x,t)}{\partial x} \frac{d\phi_i}{dx} \frac{d\phi_j}{dx} dx \tag{6.18}$$

$$\Gamma_{ij} = \gamma^4 \delta_{ij} \tag{6.19}$$

$$M_{ij} = M_{ji} = \beta^4 \int_0^L \phi_i \phi_j dx \tag{6.20}$$

where δ_{ij}=Kronecker's delta. It should be noted that P_{ij} is a function of time. The system, Eq. (6.16), admits a non-trivial solution when the determinant,

$$\left| K_{ij} - P_{ij} + \Gamma_{ij} - \Omega^2 M_{ij} \right| = 0 \tag{6.21}$$

The solution, Eq. (6.12), is always bounded when all the eigenvalues, Ω, are real. When one or more of the eigenvalues Ω becomes complex with a negative imaginary part, the solution becomes unbounded and an instability is indicated. The first instance at which this occurs denoted as $t = t^*$, is called the *critical time to buckle*. Once this time is determined, the corresponding mode shape and buckling load can be obtained.

6.2.2 Finite element analysis

When the core is not thick enough to prevent the two face sheets from communicating each other during the dynamic event, the bifurcation analysis based on the elastic foundation model loses its validity. The sandwich structure should be considered as a whole assembly to examine the dynamic response to the axial impact. In this case, the stress wave is combination of the incoming and reflecting waves as well as the stress waves from other constituents unlike a homogenized material. In addition, since the core is much softer than the face sheets, the core is likely to experience the plastic deformation while the face sheets is still in the elastic region. These complications due to the combination of two different materials are most

suitably handled through the finite element method. To this end, the commercial finite element analysis (FEA) package ABAQUS/Explicit is employed to simulate the dynamic response of an initially imperfect sandwich beam subjected to an axial impact. The face sheet is modeled with a three–node quadratic beam element to consider shear deformation and also to include effects of rotary inertia. The face sheet is assumed as an elastic material, while the core as an elastic–plastic continuum. The inelastic behavior of the core is obtained from Fig. 5.4 in Chapter V. The core is modeled with a CPS4R element, two-dimensional bilinear solid element with reduced integration. Perfect bonding is enforced to the interfaces between the face sheets and the core, and the top and the bottom face sheets are tied to the top and bottom core surfaces, respectively. The sandwich beam is meshed with a sufficient number of elements along the length, resulting in no significant change both qualitatively and quantitatively with further refinement. An initial clearance between the mass and beam is considered to simulate the drop impact. Since the material of the impactor mass is assumed to be much stiffer than the beam, the mass is modeled with a rigid body element. The FE modeling of the problem is illustrated in Fig. 6.2.

6.3 Experimental setup

The material properties of the face sheets and the core are summarized in Chapter V. Three groups of specimens with the gage length of 55 mm, 100 mm, and 200 mm were prepared for the 12.5 mm thick core sandwich beam. For the 25 mm thick core sandwich specimen, 100 mm and 200 mm beams were examined. All the specimens had the same width of 61 mm. The impacted end of the specimen was restrained from moving perpendicular to the loading direction by the steel wedges as shown in Fig. 6.1. The other end was clamped by steel grips with plastic steel

putty to constrain end rotations. Strain gages were attached on the front and back surfaces of the specimens at 1.5 cm below from the impacted end to obtain the localized buckling responses. The sandwich specimen was mounted on the fixture that held the top steel wedge block for the uniaxial movement of the impacted end. The entire assembly of the sandwich specimen was firmly fastened by a screw to the steel base to prevent bounce after the impact. Parallel lines were marked transversely to clarify the deformation during the impact event. The configuration of the prepared sandwich specimens is illustrated in Fig. 6.1.

The specimens were axially impacted by a falling weight guided by linear motion bearings installed in the drop tower apparatus. The impactor mass was 32.65 kg and the impact velocity was 2.1 m/s falling from 23 cm above the impact surface. The applied compressive load was measured from the load cell attached to the impactor. The responses of the specimens were measured by the strain gauges attached to the front and the back surfaces of the specimens. Oscilloscopes with high sampling rate of 4GHz were used for the data acquisition. Two high speed cameras with a speed of 1 millisecond and 100 microsecond were used to obtain the sequential evolution of the failure modes of the sandwich specimens for a very short duration.

6.4 Results and discussion

6.4.1 Results of sandwich specimens with 25 mm thick core

The test results of the sandwich specimens are summarized in Table 6.1. The peak loads of the specimens are similar to each other although they tend to decrease as the specimen becomes longer, which was observed from the static events in Chapter V. The gross-section strength, associated with the peak load, is based on the full cross section area, $b(t^c+2t^f)$, where b=width of the beam. The failure time, t_F, is shortened for the smaller specimen since it has lower capability of absorbing the impact energy

than the bigger size. The failure time is obtained when the load reaches its maximum value, ignoring the initial time delay region. The time delay, t_D, is defined as time duration before the load starts to increase fairly linearly. The initial time delay is unavoidable in the experiments since it is the time for the two surfaces between the impactor mass and the impacted end of the specimen to be in complete contact with each other. If the two contact surfaces are perfectly parallel to each other, the load profile will start without any time delay and follow the linear line indicated in Fig. 6.3. For example, Fig. 6.3 shows the initial time delay region and the failure time.

The impact response of the 100 mm long sandwich specimen with a 25 mm thick core is shown in Fig. 6.3. The load profile is acquired from the load cell attached to the impactor mass. Initially, there is a lag of the load before it starts to increase linearly until the sandwich specimen collapses at its ultimate strength. The time duration for the initial lag is defined as time delay, t_D, as addressed earlier. Four points from A to D indicated in Fig. 6.3 are associated with the deformation images taken by the high speed camera with a speed of 100 microsecond, listed in Fig. 6.4. Up to the point A, there is no predominant out-of-plane deformation, but the specimen is axially compressed. As the load increases, the face sheet at the impacted end undergoes localized deformation, leading to the failure of the sandwich specimen. As shown in Fig. 6.4 (d), the failure triggers the first delamination propagating to the other end of the specimen and then the delamination on the other side.

Fig. 6.5 shows the impact responses of the sandwich specimens of the length 200 mm with the same thickness of the core as in Fig. 6.3. The initial load profiles are very similar to that of the shorter specimen. However, it is interesting that there exist level-off regions for a very short time duration at around half of the maximum

load. The sequential deformation images of a specimen are shown in Fig 6.6, corresponding to the points A through D as indicated in Fig. 6.5. From the points A to B, the sandwich specimen experiences axial compression with no bending deformation as shown in Fig. 6.6(a) and Fig. 6.6(b). The sandwich specimen is failed by delamination initiated from the impacted end as shown in Fig. 6.6(c). For the finer examination of the failure growth between the points B and C, higher speed camera with 10,000 frames per second was used to obtain the images in Fig. 6.7. It appears that the sandwich specimen experiences axial compression with no predominant bending deformation before the inflated deformation at the impacted end occurs. Once the out-of-plane deformation initiates, the specimen experience buckling deformation which then drive the delamination over the interlaminar strength of the specimen. This is an important finding of the present study.

Fig. 6.8 shows the out-of-plane deformation of the face sheet with the length of 20 cm from FE analysis. Note that the FE analysis considers the initial imperfection and the response is obtained after the axial impact. The initial imperfection shape is obtained from the eigenbuckling analysis through FEA and the maximum amount of the initial deflection is 1% of the beam length. The time interval for the first four shapes is $4t_w$, where t_w is the time for the stress wave to travel along the face sheet from the impacted end to the other end. The normalized deformation, w/L, shows unsubstantial increase until the time reaches the critical time, t^*. The critical time will be discussed in detail later in association with the bifurcation analysis discussed earlier. After the critical time, even with the shorter time interval, $1.3t_w$, the out-of-plane deformation shows sudden growth. The deformation is intensified at the impacted end, that causes the delamination in the experiments. The corresponding sequential deformations of the whole sandwich beam is shown in Fig. 6.9. The

sandwich beam loses the load carrying capability after the inflated deformation at the impacted end.

The dynamic buckling shapes observed in Fig. 6.4 and Fig. 6.6 are the localized deformation, causing delamination from the impacted end. FEA also simulates the inflated deformation at the end as shown in Fig. 6.9 (f). The overall deformation of the sandwich specimens are not predominant throughout the dynamic buckling development. It can be concluded that the core is thick enough to paralyze the gross dynamic buckling of the sandwich beam, and the sandwich specimen is failed mainly by the individual deformation of the face sheet, not by the deformation of the entire assembly. Therefore, this sandwich beam can be modeled as a beam on an elastic foundation.

The bifurcation analysis finds the critical time, t^*, when the axial strain in the beam satisfy the emergence of dynamic buckling of the beam. The analytical critical times for the face sheet of the lengths 10 cm and 20 cm, obtained from the present analysis, are plotted in Fig. 6.10. As the core becomes stiffer, the critical time increases since the transverse normal stiffness of the core provides additional support for the face sheet to resist dynamic buckling deformation. The analytical critical time for the 200 mm long sandwich specimen is compared against the experimental result in Fig. 6.11. As shown in the figure, the dynamic buckling initiates well before the peak load and the beam is experiencing the temporal evolution of the out-of-plane deformation until it causes the collapse of the sandwich specimen. The bending strain response in Fig. 6.11 also indicates that a global deformation of the entire assembly is not observed for the thick sandwich specimen.

6.4.2 Results of sandwich specimens with 12.5 mm thick core

Fig. 6.12 shows the impact responses of the 55 mm long sandwich specimens with a 12.5 mm thick core. The load profiles are similar to other test results. The deformation growth along the load profile is shown in Fig. 6.13 at the points A, B, and C. The pictures in Fig. 6.13 were taken with the time interval of 1 millisecond. The sandwich specimen shows little deformation until it collapses at the point C. The deformation growth is shown in Fig. 6.14, that were taken between the point B and C with the time interval of 100 microsecond. The buckling deformation becomes apparent when the load reaches the maximum and it causes the failure of the sandwich specimens when the deformation exceeds the ultimate strength of the sandwich structure. The deformed shape for this thinner core sandwich specimens is different than the thicker one observed in Fig. 6.4 and Fig. 6.6. The face sheets can interact with each other due to the small thickness of the core and, as a result, the whole assembly of the structure deforms together unlike the thicker specimens that failed by the individual buckling of the face sheets.

Fig. 6.15 shows the load configuration as a function of time for the sandwich specimens of the length 100 mm with the 12.5 mm thick core. The typical deformed shape for this sandwich specimen is shown in Fig. 6.16 with the time interval of 1 millisecond. Similarly with the other test results, the sandwich beam is compressed with no bending deformation up to the point B and is seen to fail after the peak load. The out-of-plane deformation grows and is localized as shown in Fig. 6.17 (e). As can be seen in the sequential images in Fig. 6.17, the localized deformation triggers the collapse of the entire sandwich structure at its ultimate strength. Again, the buckling deformation is observed in the entire beam.

Fig. 6.18 shows the dynamic responses of the 200 mm long sandwich specimens

with the 12.5 mm thick core. From the points A to B indicated in Fig. 6.18, the images of Fig. 6.19 (a) and (b) shows that the specimen is axially compressed without obvious out-of-plane deformation. As the load increases, the specimens starts to deform as shown in Fig. 6.19(c) at the point C on the load profile. The enhanced deformation over the limit strength of the sandwich structure results in the gross failure as shown in Fig. 6.19(d). Fig. 6.20 shows the detailed buckling deformation growth with the finer time interval of 100 microsecond. The images were obtained from the point B on the load profile Fig. 6.18. The buckling deformation is not obvious in the beginning but is enhanced until the load reaches the maximum strength of the sandwich specimen.

The failure mechanisms of the sandwich specimens with the core of the 12.5 mm thickness exhibit the similar processes even with the different beam lengths. The specimens are initially compressed with no predominant bending deformation, and then fail by the buckling deformation clearly observed around the peak loads. In fact, the dynamic buckling initiates well before the peak loads even though the deformation is not apparent in the images. The dynamic event is well explained in Fig. 6.21 showing typical load and strain responses of the sandwich beam. The load axis is normalized by the analytical dynamic buckling load and the time axis is normalized by the critical time. The critical time in this case is obtained from FE analysis when the sandwich model loses its load carrying capability. The axial strains and the bending strains are obtained from the strain gages attached on the front and back surfaces of the face sheets at 15 mm below the impacted end. When the load increases and reaches the first level-off region, the bending strain starts to suddenly increase from being negligible, i.e., dynamic buckling initiates. However, the deformation is too small to be captured by the high speed camera images. The

sandwich specimens then enters a new equilibrium state and is stabilized with the growing buckling deformation. The sandwich beam can sustain the impact load after the onset of dynamic buckling until the ultimate strength of the structure is exceeded. The ultimate strength is dictated by delamination resistance between face sheets and core and the core shear capacity.

The dynamic buckling events are also examined using FE analysis. Since the core is not thick enough to apply the bifurcation analysis to this sandwich specimen, FE analysis is suitable to analyze the mechanism of the dynamic buckling growth. Fig. 6.22 shows the growing out-of-plane deformation as time increases, computed from the FE analysis for the 200 mm long sandwich specimen. As can be seen in the figure, the deformation reveals the sudden change after some point that is defined even with the short time duration. This point in time can be defined as the critical time, t^*. The corresponding deformation shapes of the whole assembly are shown in Fig. 6.23. FE analysis predicts the localized deformed shape around the impacted end, which is in reasonable agreement with the experimental results in Fig. 6.19. The associated loads are also in good agreement with the experimental data in Fig. 6.18. The buckling deformation causes the failure of the sandwich structure and, hence, the loss of load carrying capability as shown in Fig. 6.23 (h).

6.5 Conclusion

Dynamic bifurcation buckling analysis for the sandwich beam is presented based on an elastic foundation model for the core. The critical time is defined as a quantity to define the onset of the dynamic buckling of a sandwich beam. For the sandwich beam with a thinner core, FE analysis is performed to investigate the emergence of dynamic buckling of the beam subjected to an axial impact. Dynamic buckling is seen

to occur when the superposed axial strain waves satisfy a certain condition. Impact tests on sandwich specimens with various configuration were performed to study the dynamic buckling growth. It is observed that the buckling deformation occurs after the axial deformation. The sandwich specimens starts to buckle at some point and is stabilized in a new equilibrium state with the growing buckling deformation until the buckling deformation drives other failure mechanism (interlaminar shear failure between face sheets and core and core shear collapse). The critical time obtained from the bifurcation analysis is a good indicator of the start of deformation growth (buckling evolution), which the onset of the dynamic buckling well before the entire collapse of the structure.

Core thickness (mm)	Beam length (mm)	Peak load (N)	Gross-section strength (MPa)	Failure time, t_F (ms)
25	100	35409	21.2	1.003
25	200	30782	18.4	1.500
		31849	19.1	1.587
		30871	18.5	1.145
12.5	55	40301	45.6	0.820
		43415	49.1	0.848
12.5	100	37365	42.2	1.071
		37454	42.3	1.015
		37721	42.6	1.041
12.5	200	39589	44.8	1.925
		36386	41.1	1.869
		36387	41.1	1.922

Table 6.1: Summary of the impact tests.

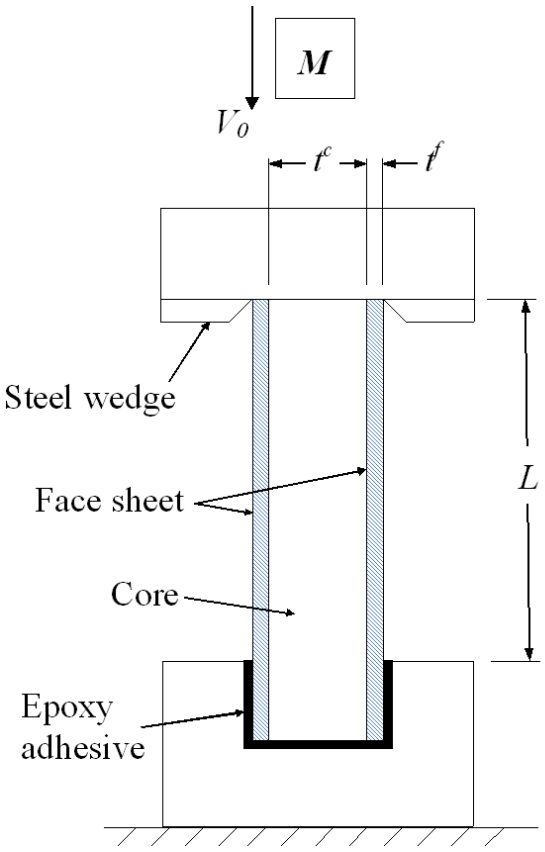

Figure 6.1: Configuration of a sandwich column uniaxially impacted from the top

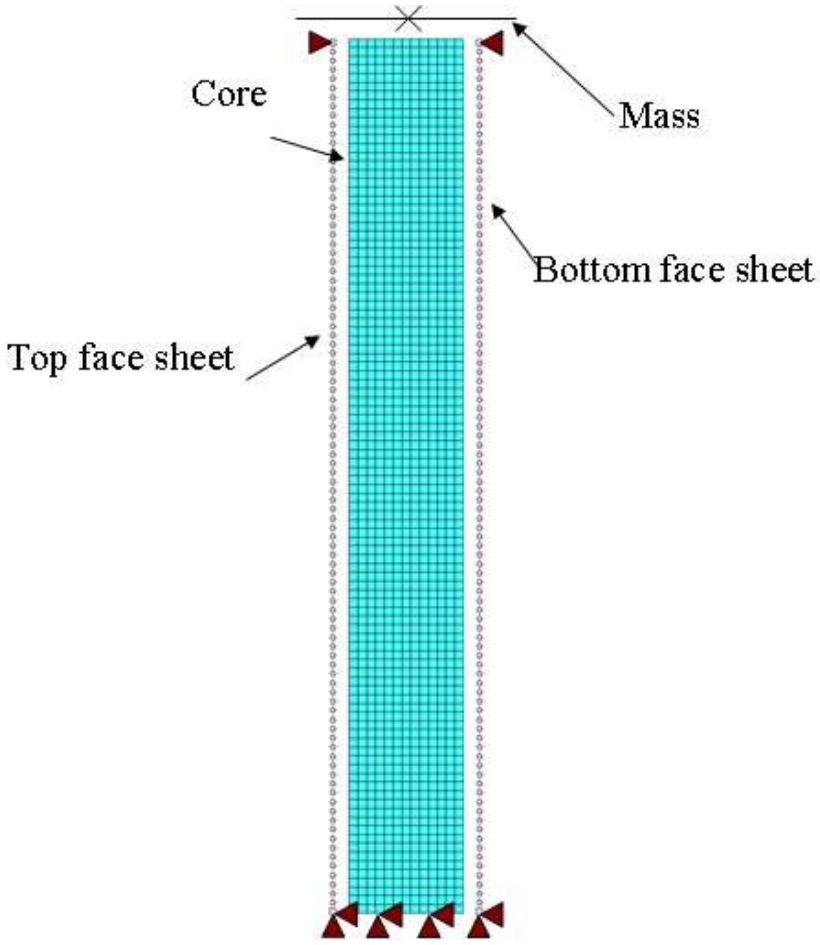

Figure 6.2: Model configuration for the Finite element analysis

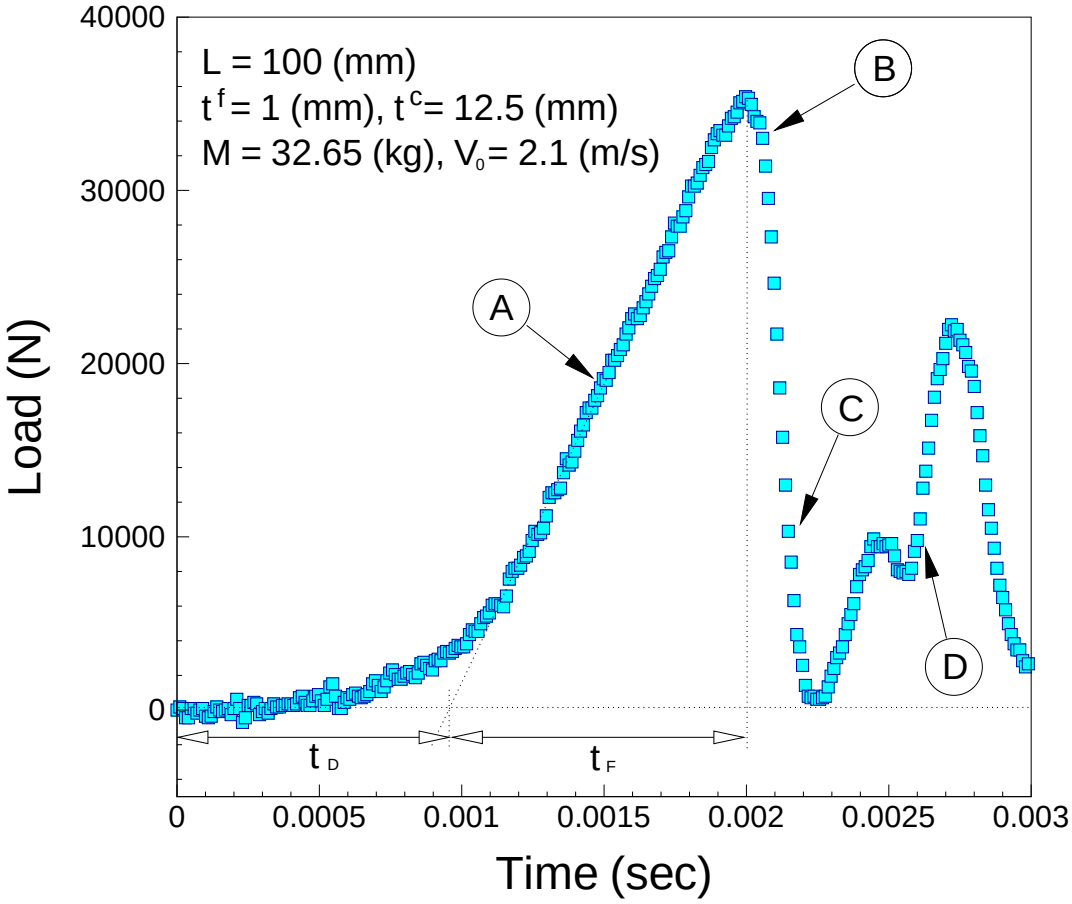

Figure 6.3: Load profile of the 10 cm long sandwich specimen with a 25 mm thick core

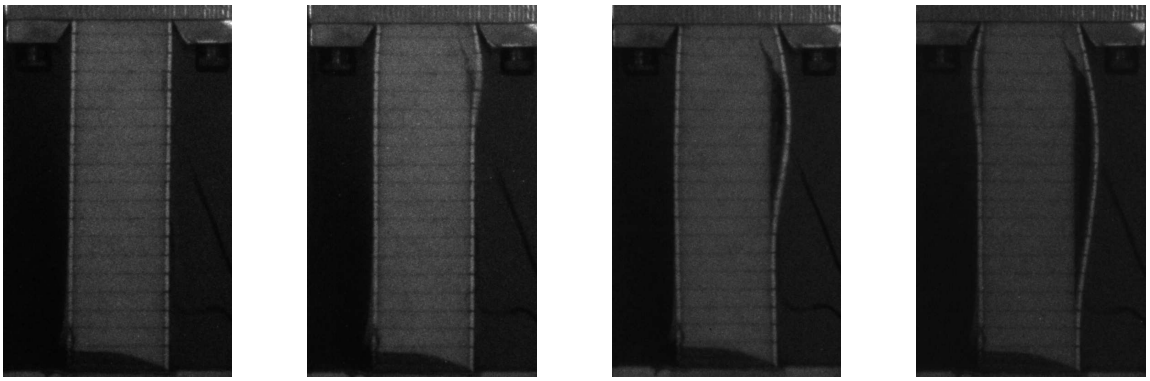

(a) Point A (b) Point B (c) Point C (d) Point D

Figure 6.4: Dynamic buckling evolution causing the collapse of the sandwich beam after the axial impact. The corresponding loads to the each deformation are indicated in Fig. 6.3 from the point A to the poind D. The time interval between the pictures is 100 microsecond.

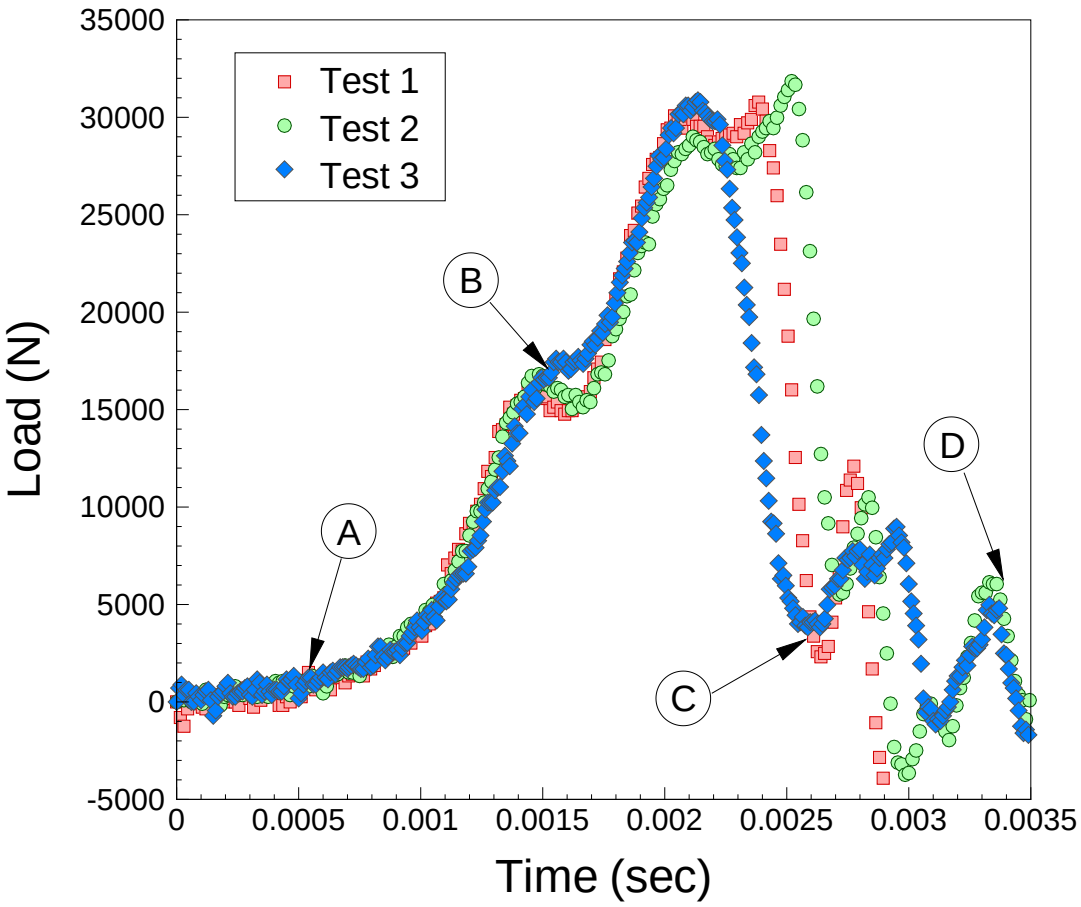

Figure 6.5: Load profiles of the 20 cm long sandwich beams with a 25 mm thick core

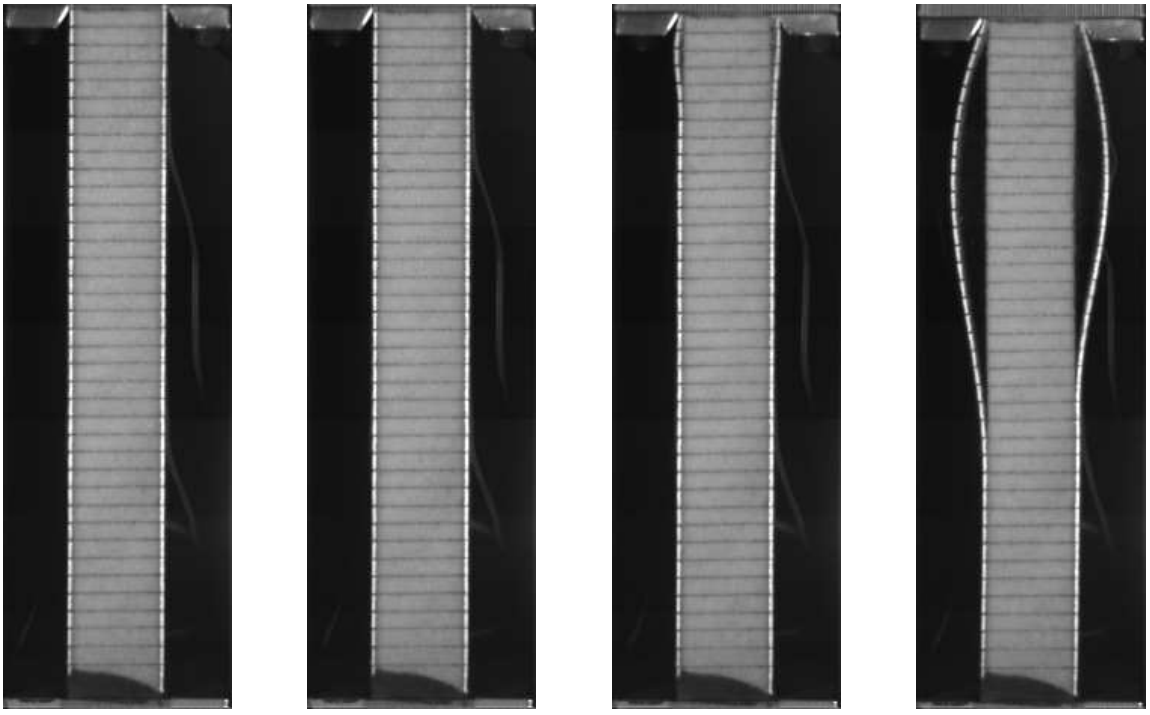

(a) Point A (b) Point B (c) Point C (d) Point D

Figure 6.6: Dynamic buckling evolution causing the collapse of the sandwich beam after the axial impact. The corresponding loads to the each deformation are indicated in Fig. 6.5 from the point A to the poind D. The time interval between the pictures is 1 millisecond.

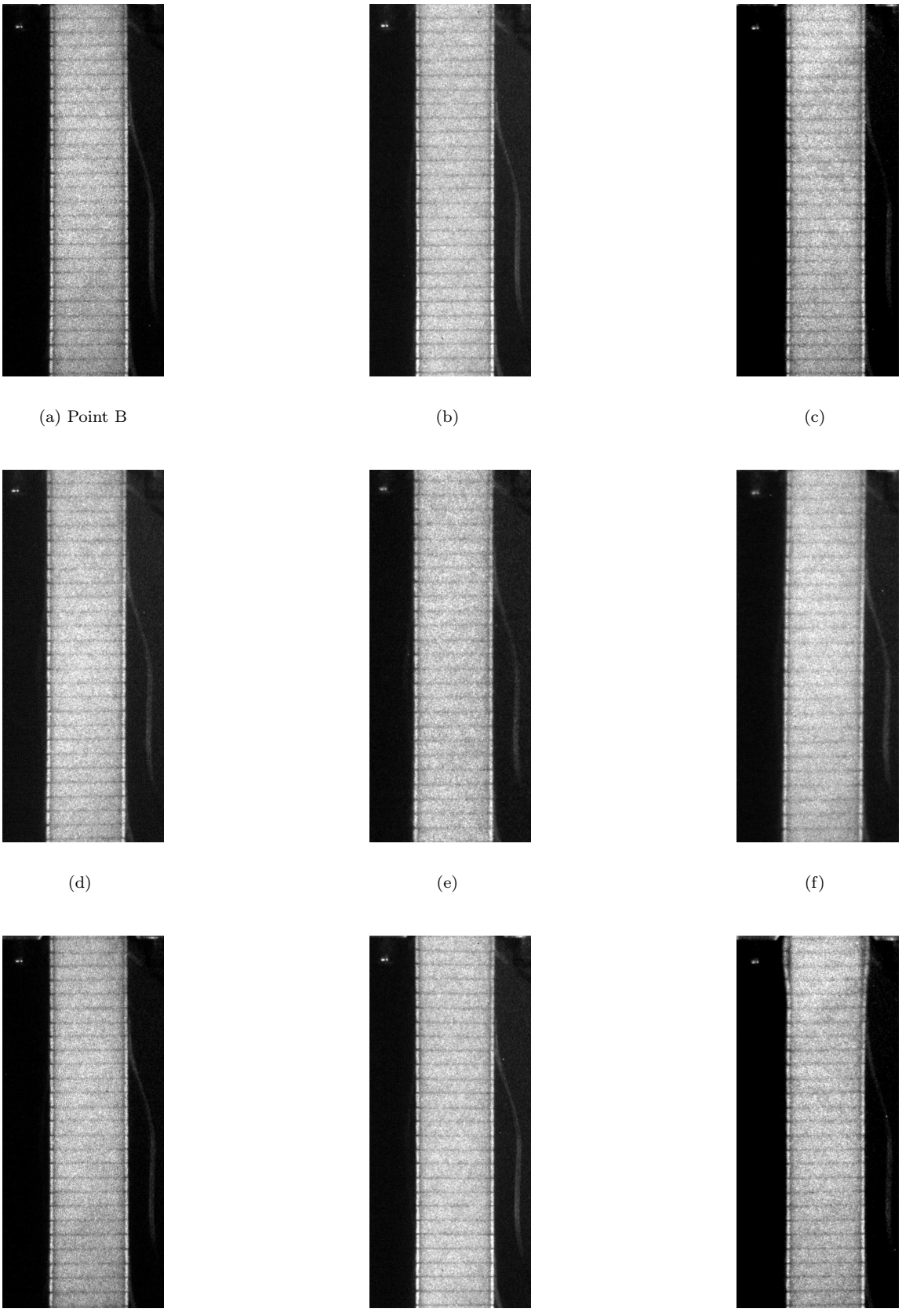

(a) Point B (b) (c)

(d) (e) (f)

(g) (h) Peak load (i) Point C

Figure 6.7: Out-of-plane deformation evolution from the point B to the point C indicated in Fig. 6.5. The time interval between the pictures is 100 microsecond.

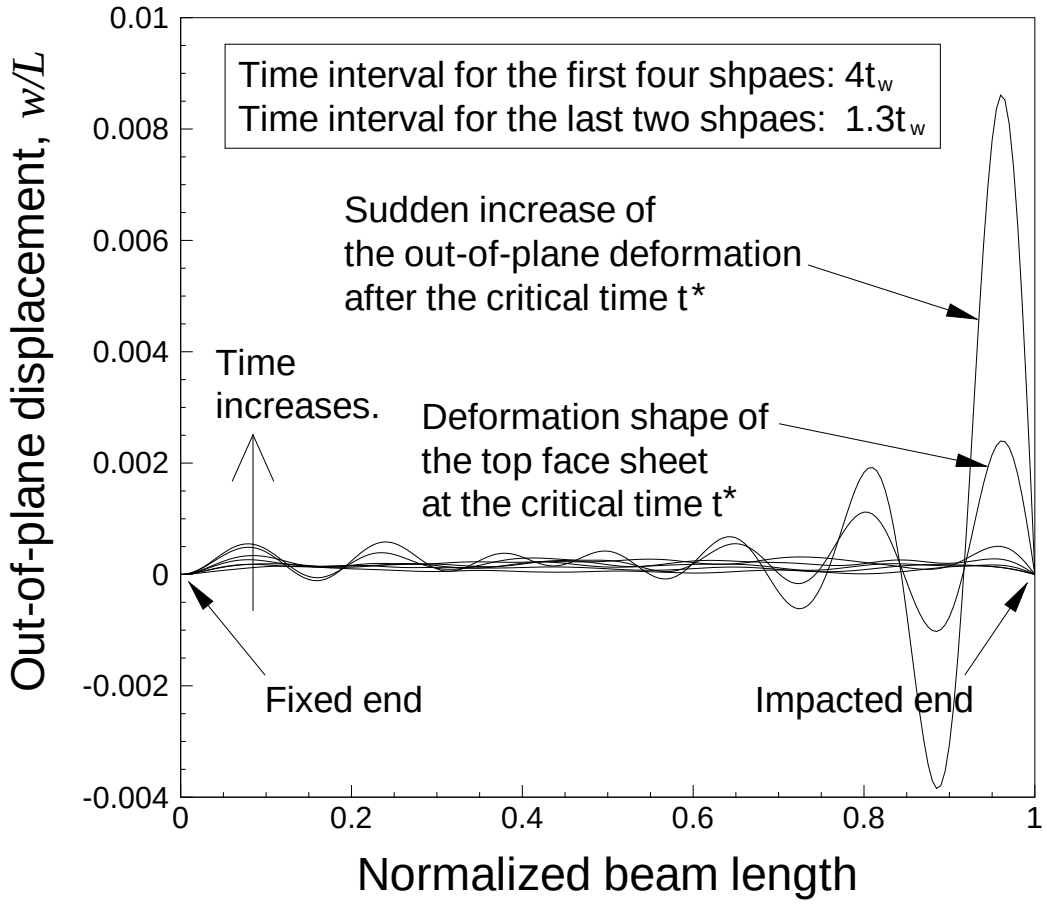

Figure 6.8: Out-of-plane deformation growth of the face sheet computed from FE analysis. The analytical critical time is defined when there is a sudden change of the deformation, causing the loss of load carrying capability of the sandwich beam.

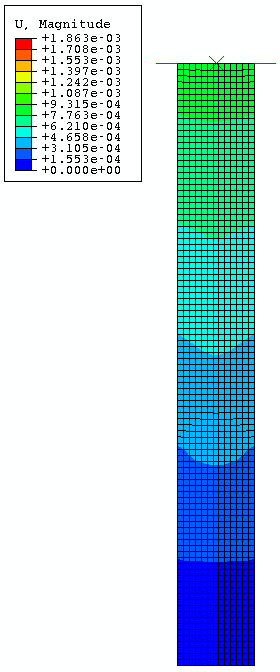

(a) P = 12501 (N)

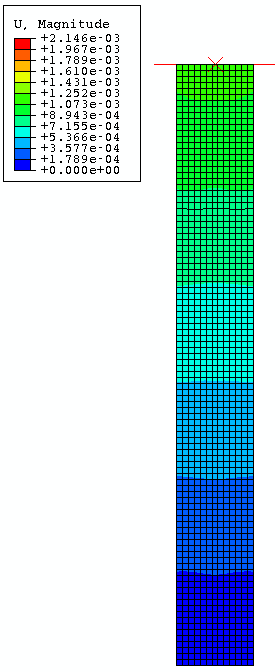

(b) P = 17009 (N)

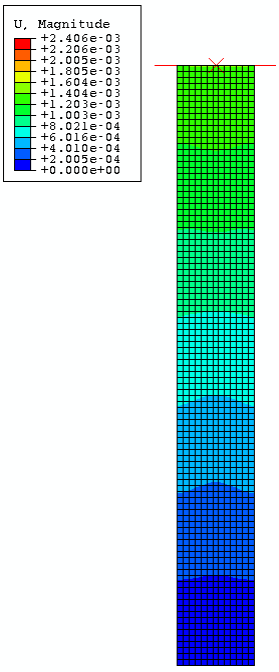

(c) P = 20418 (N)

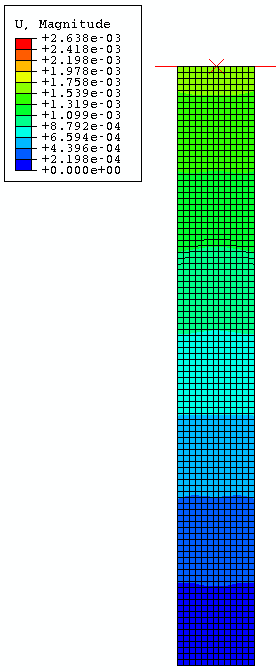

(d) P = 24375 (N)

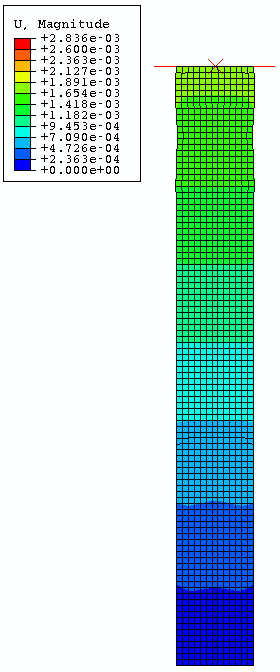

(e) P = 26281 (N)

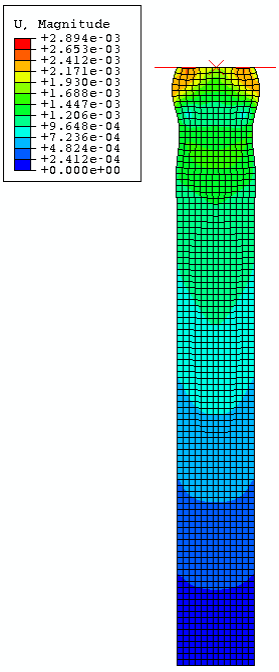

(f) P = 15054 (N)

Figure 6.9: Deformation growth of the sandwich beam from FE analysis. Deformations of the face sheet from (a) to (f) are plotted in Fig. 6.8

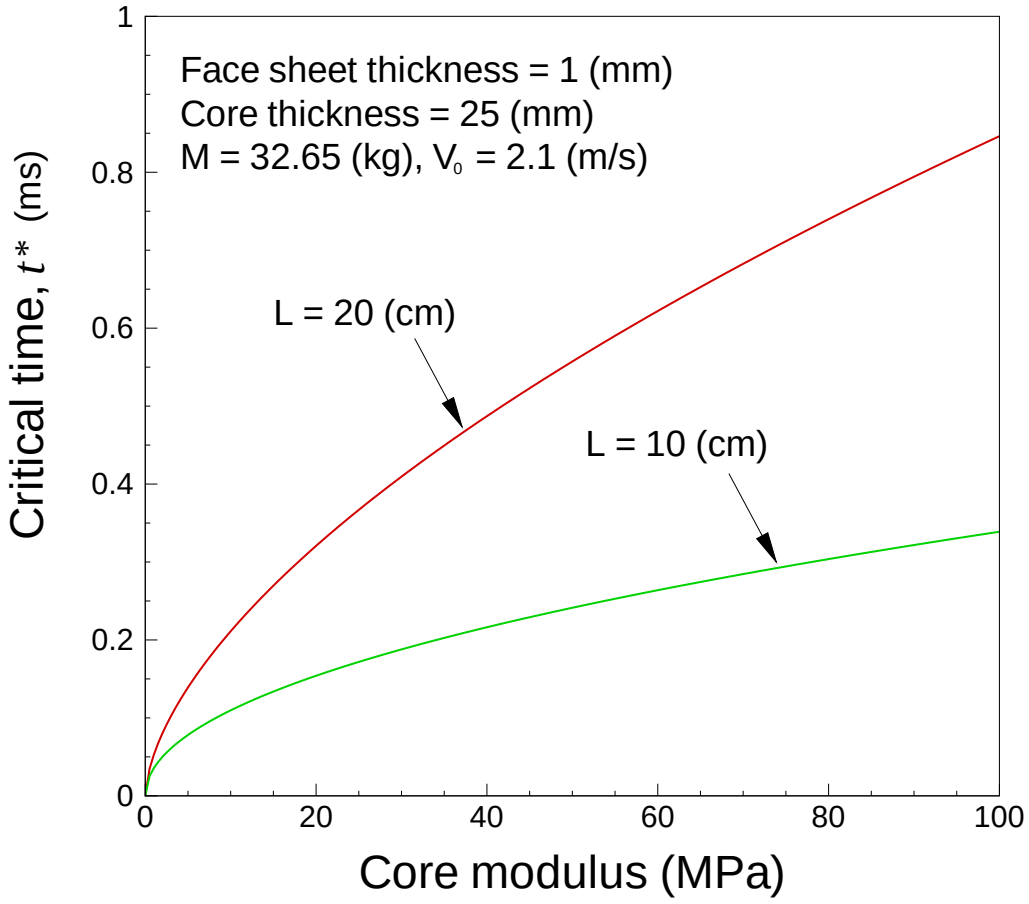

Figure 6.10: Critical time for dynamic buckling as a function of the core stiffness from the bifurcation analysis of a face sheet on elastic foundation

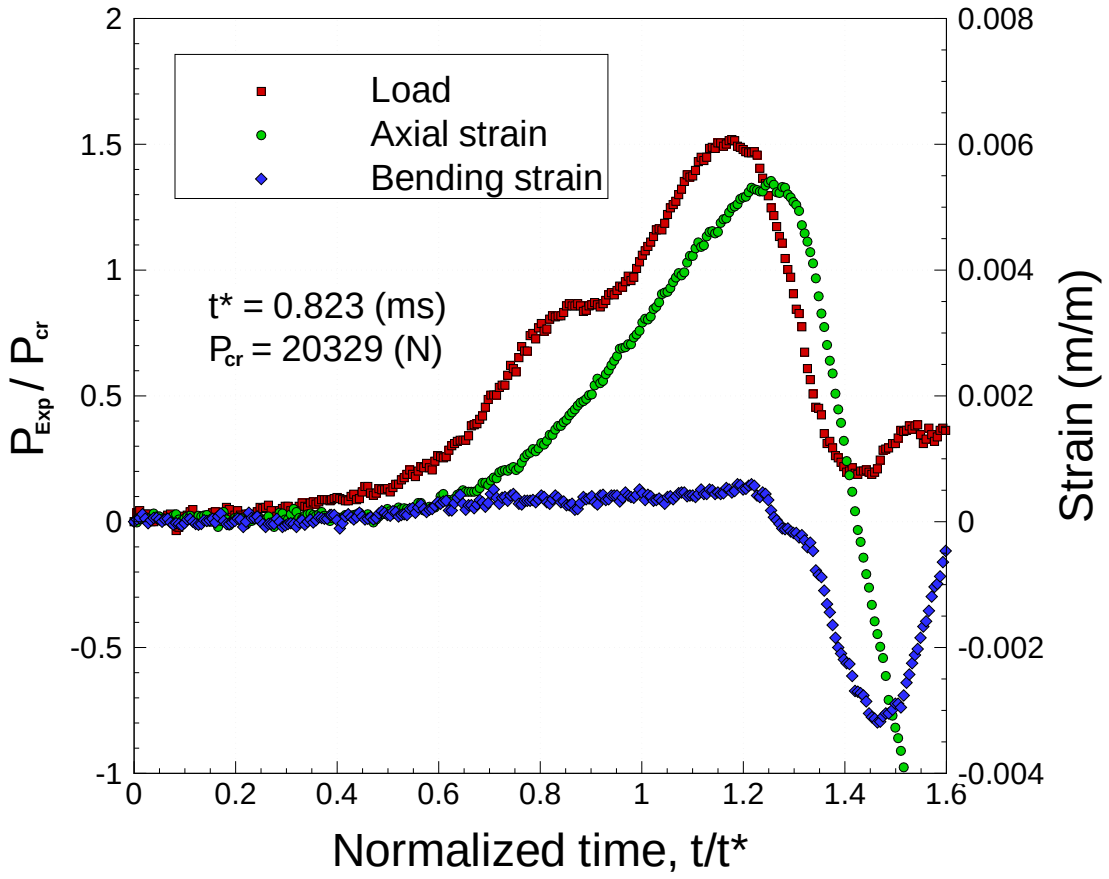

Figure 6.11: Load vs. axial and bending strain. No significant change in the bending strain is not observed until it reaches to the ultimate compressive strength.

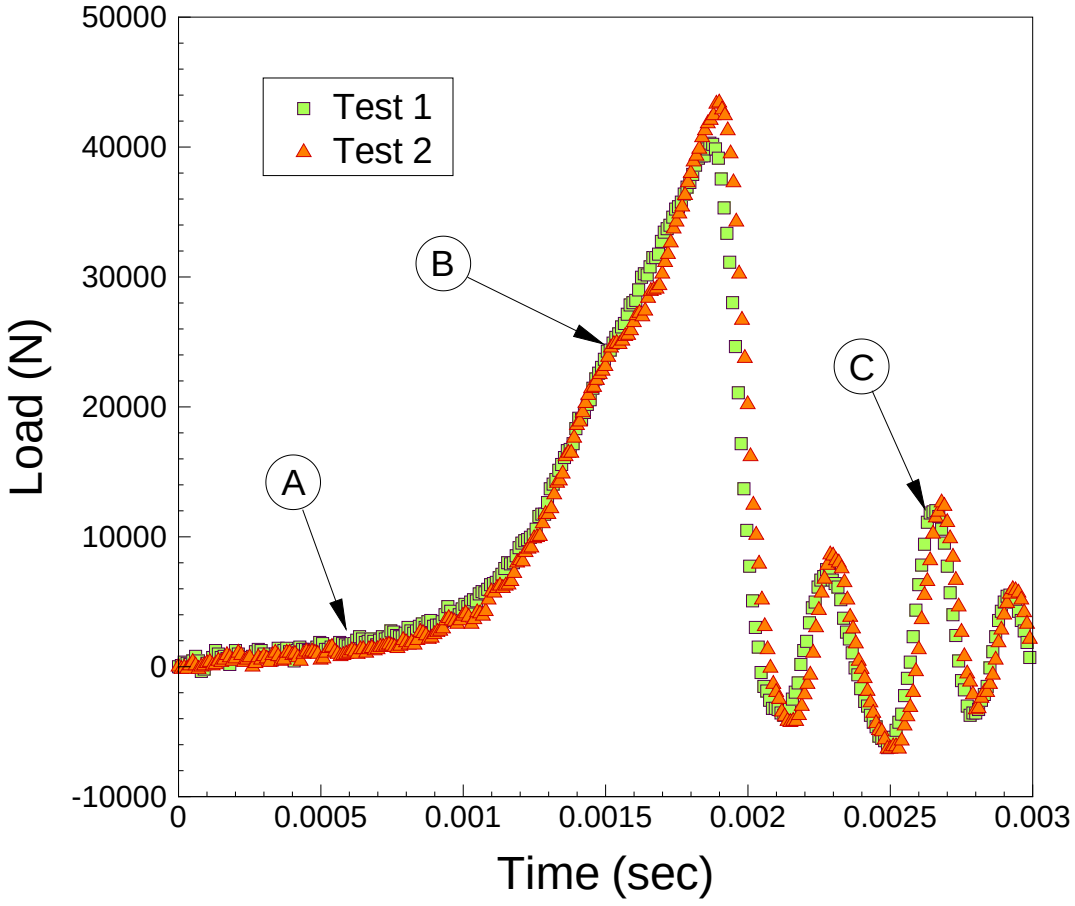

Figure 6.12: Load profiles of the 5.5 cm long sandwich beams with a 12.5 mm thick core

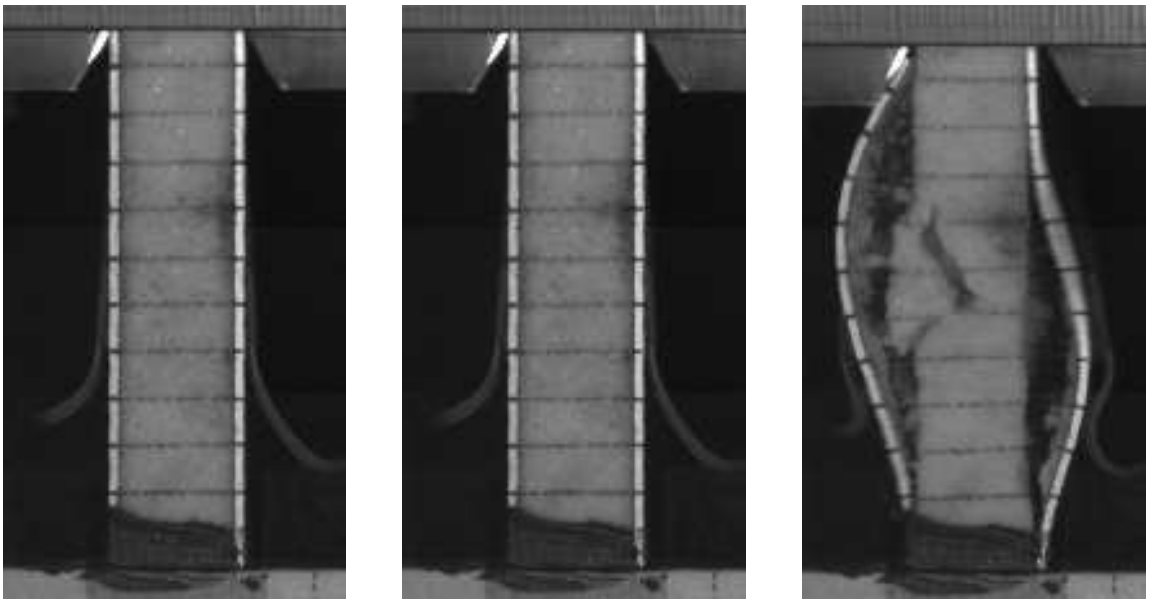

(a) Point A (b) Point B (c) Point C

Figure 6.13: Typical example of the failure growth of the sandwich specimen of the length 5.5 cm. The time interval between the pictures is 1 millisecond.

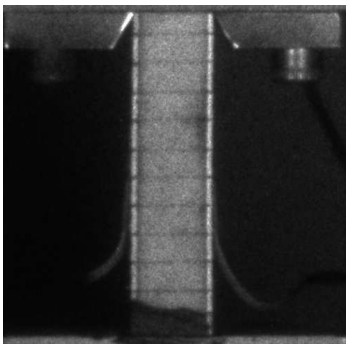

(a) Point B

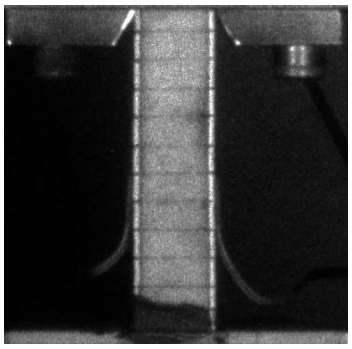

(b)

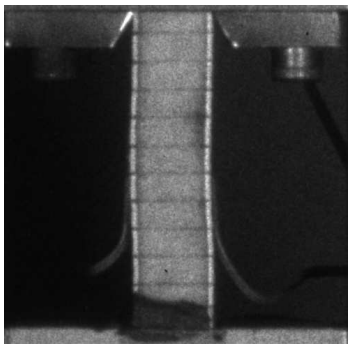

(c) Peak load

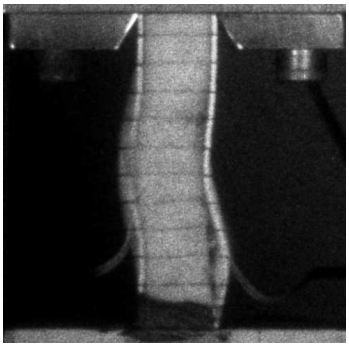

(d)

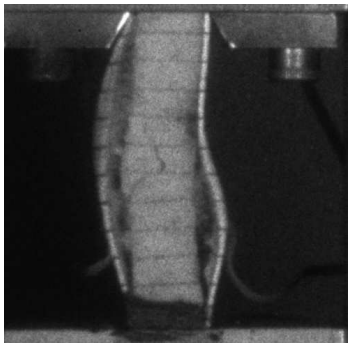

(e)

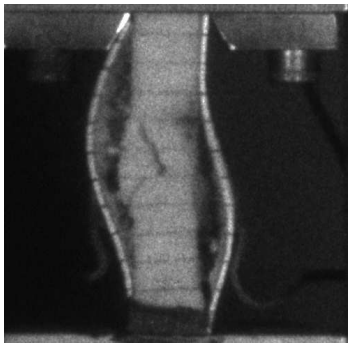

(f) Point C

Figure 6.14: Dynamic buckling evolution from the point B to the point C indicated in Fig. 6.12. The time interval between the pictures is 100 microsecond.

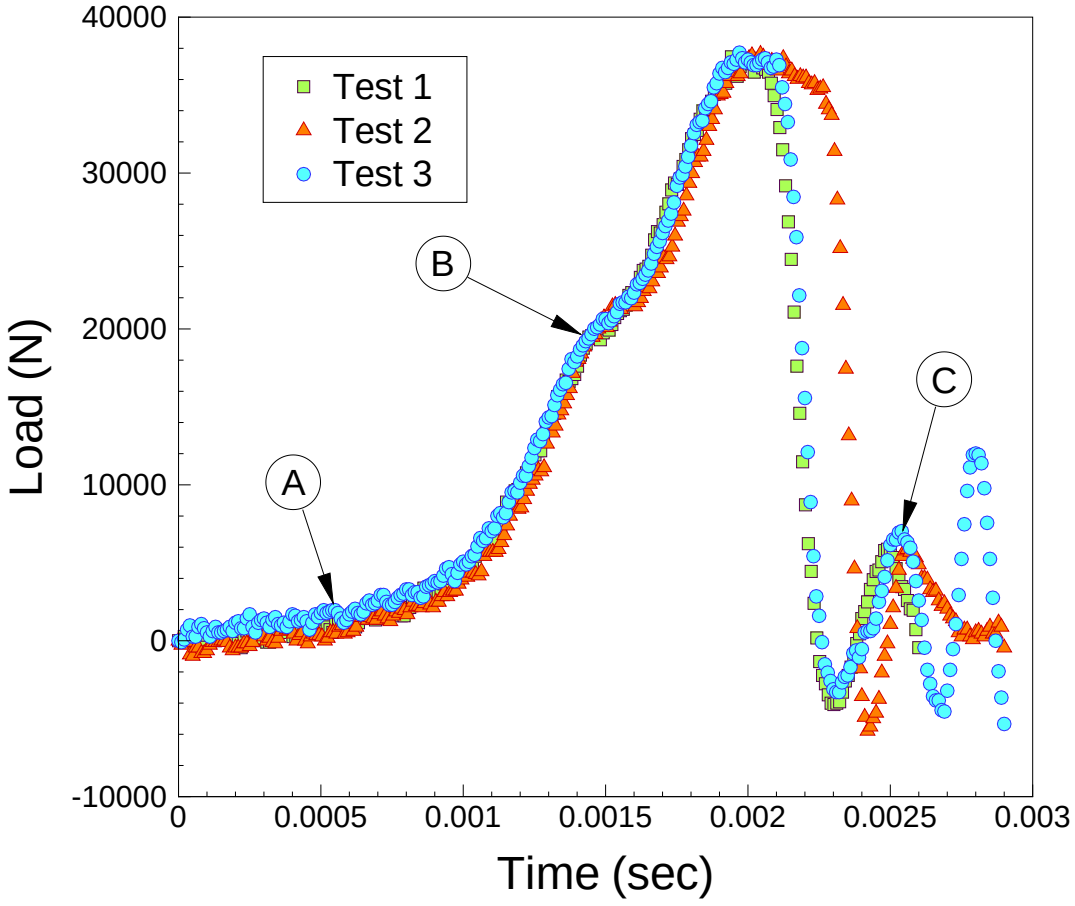

Figure 6.15: Load profiles of the 10 cm long sandwich beams with a 12.5 mm thick core

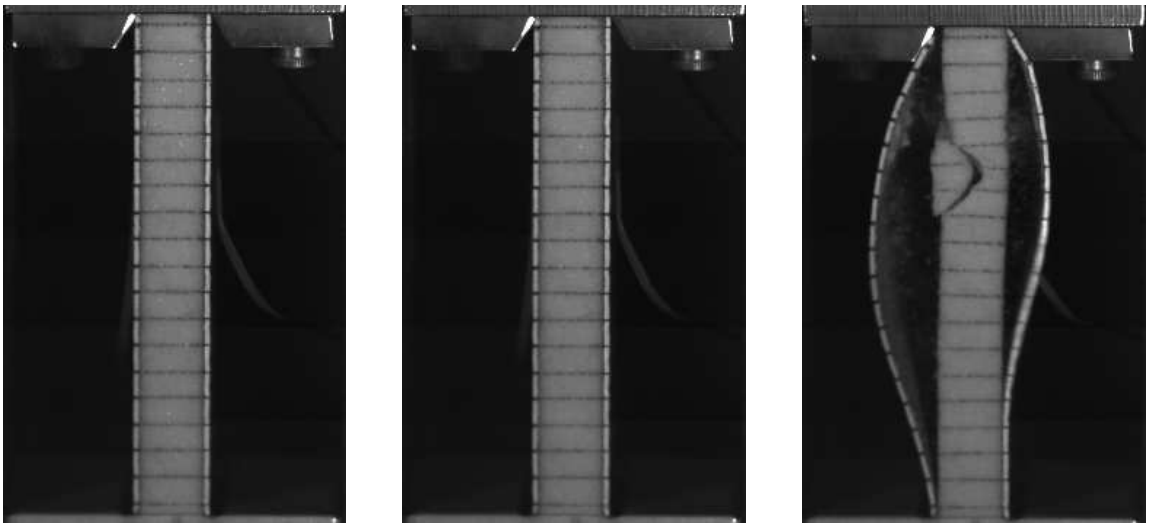

(a) Point A (b) Point B (c) Point C

Figure 6.16: Dynamic buckling evolution of the 10 cm length of the sandwich beam. The points through A to C are indicated in Fig. 6.15. The time interval between the pictures is 1 millisecond.

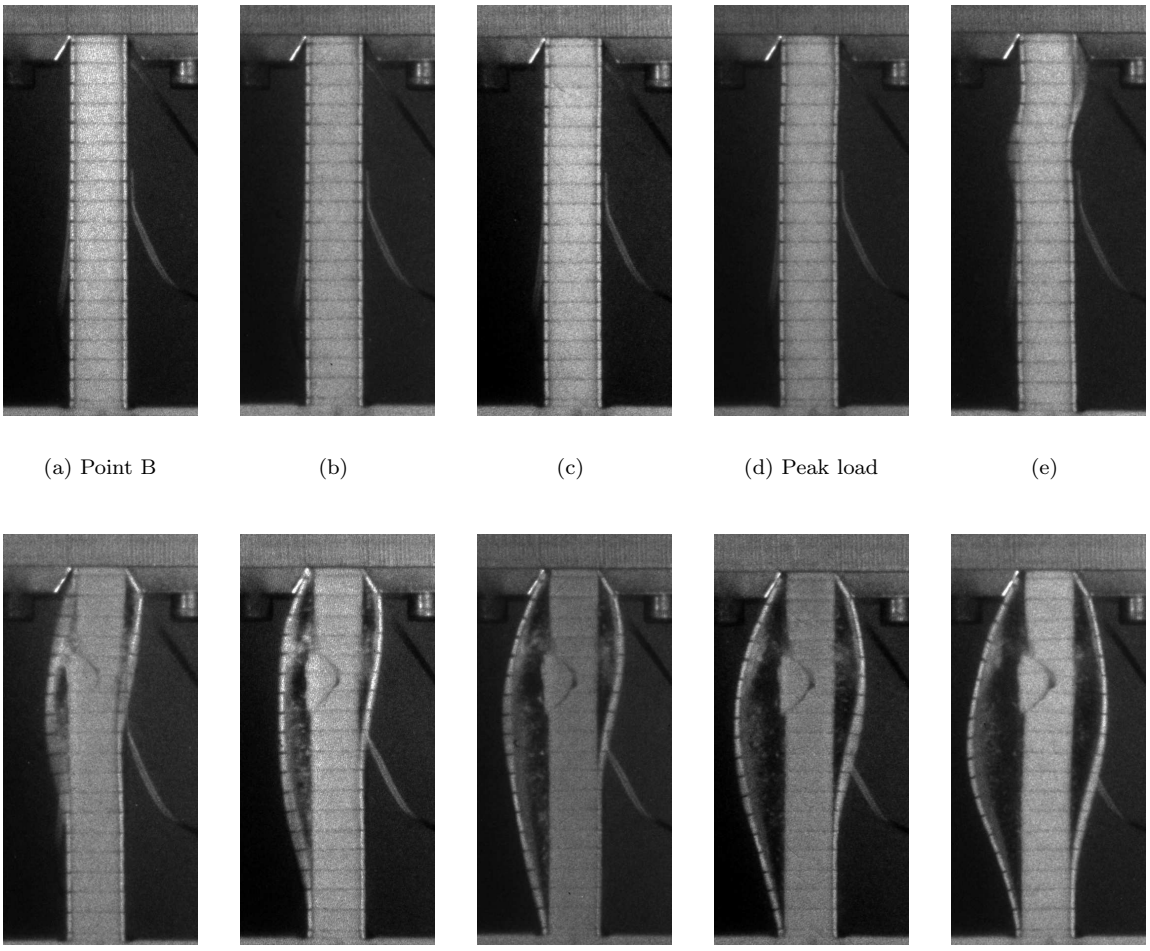

(a) Point B (b) (c) (d) Peak load (e)

(f) (g) (h) (i) (j) Point C

Figure 6.17: Out-of-plane deformation evolution from the point B to the point C indicated in Fig. 6.15. The time interval between the pictures is 100 microsecond.

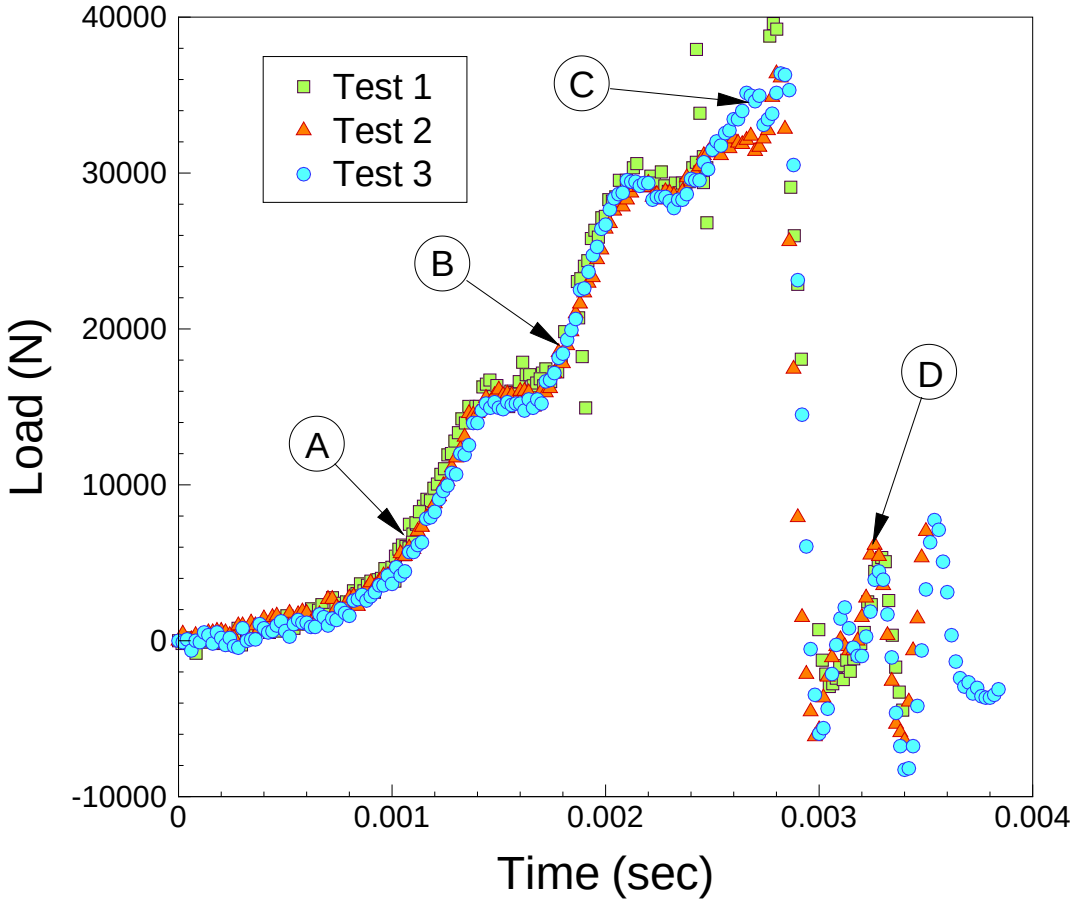

Figure 6.18: Load profiles of the 20 cm long sandwich beams with a 12.5 mm thick core

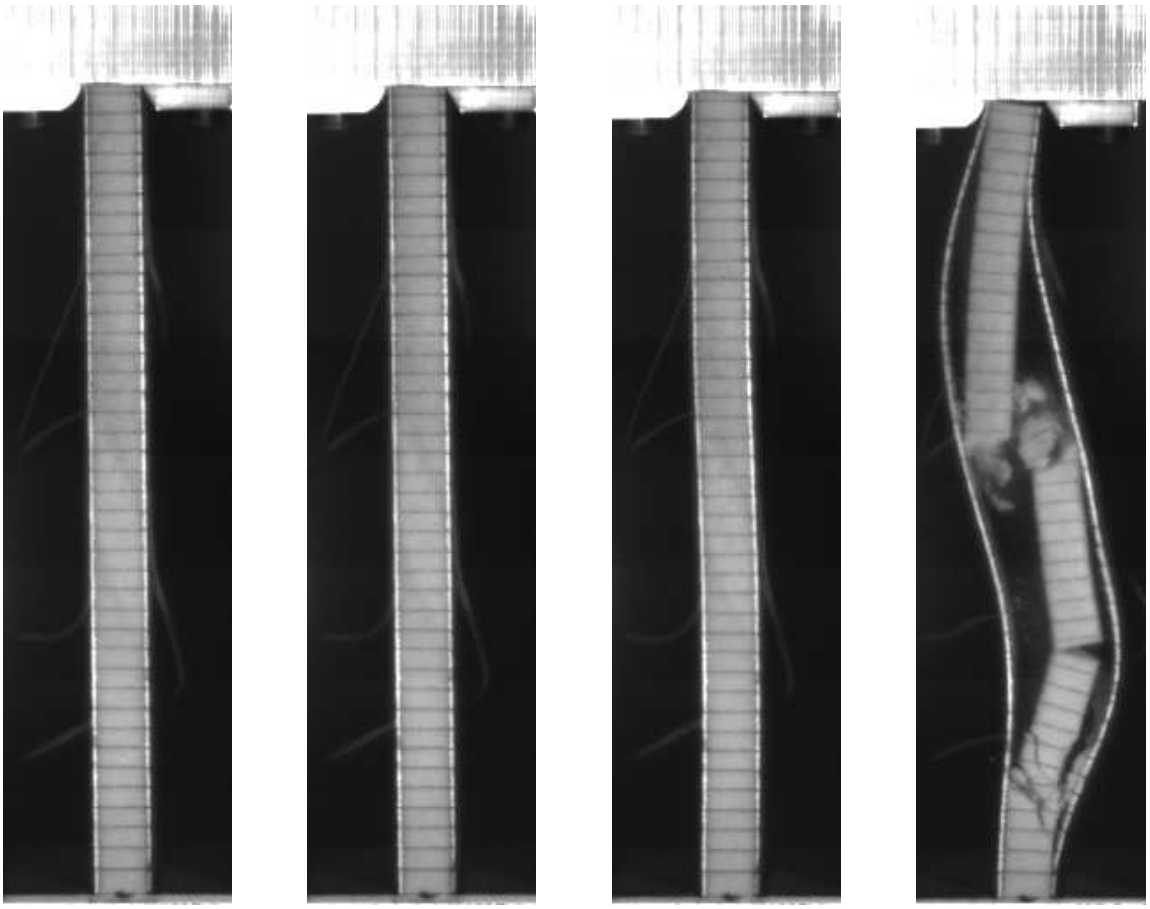

(a) Point A (b) Point B (c) Point C (d) Point D

Figure 6.19: Dynamic buckling evolution causing the collapse of the sandwich beam after the axial impact. The corresponding loads to the each deformation are indicated in Fig. 6.18 from the point A to the poind D. The time interval between the pictures is 1 millisecond.

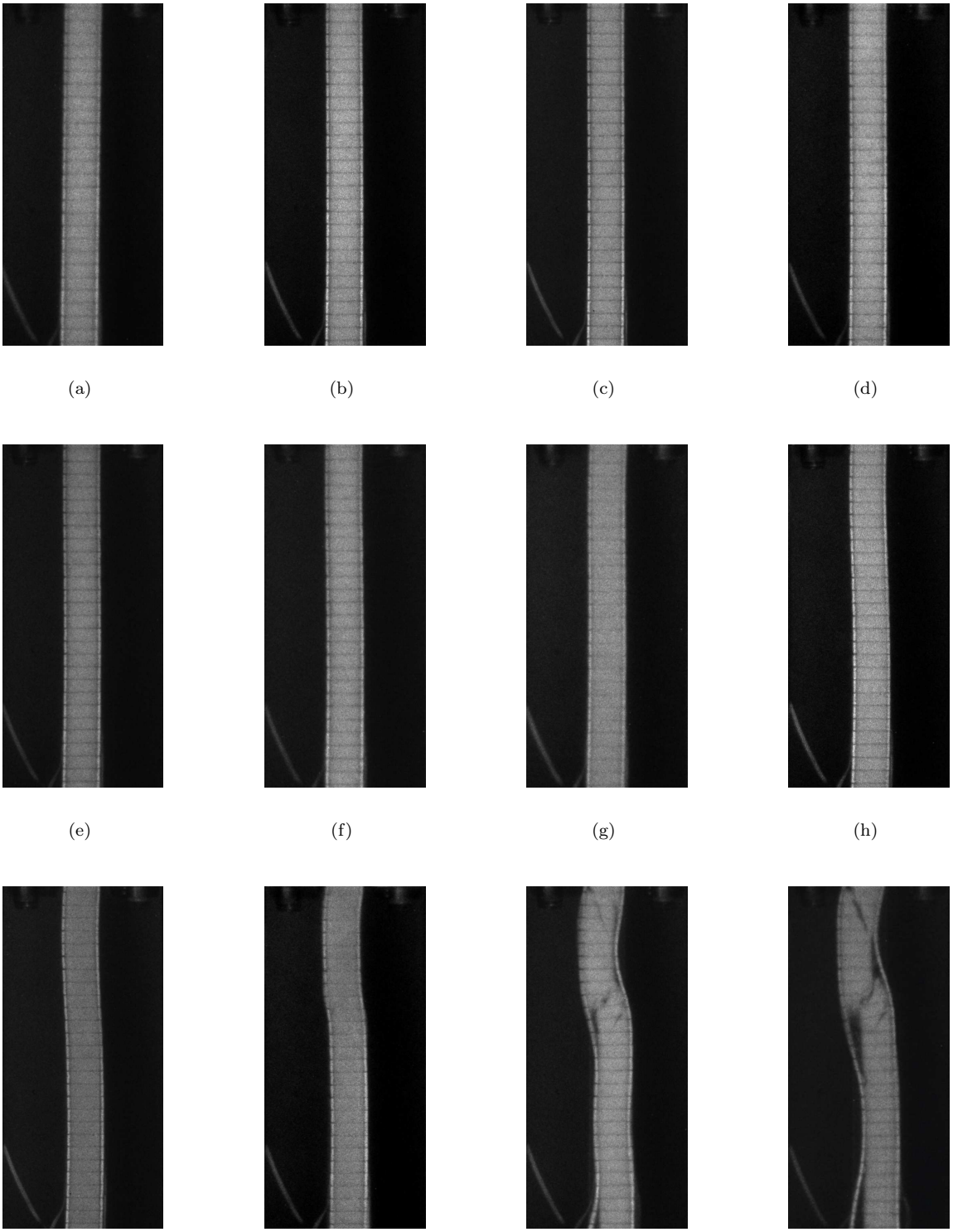

(a) (b) (c) (d)

(e) (f) (g) (h)

(i) Peak load (j) (k) (l)

Figure 6.20: Out-of-plane deformation evolution from the point B to the point D indicated in Fig. 6.18. The time interval between the pictures is 100 microsecond.

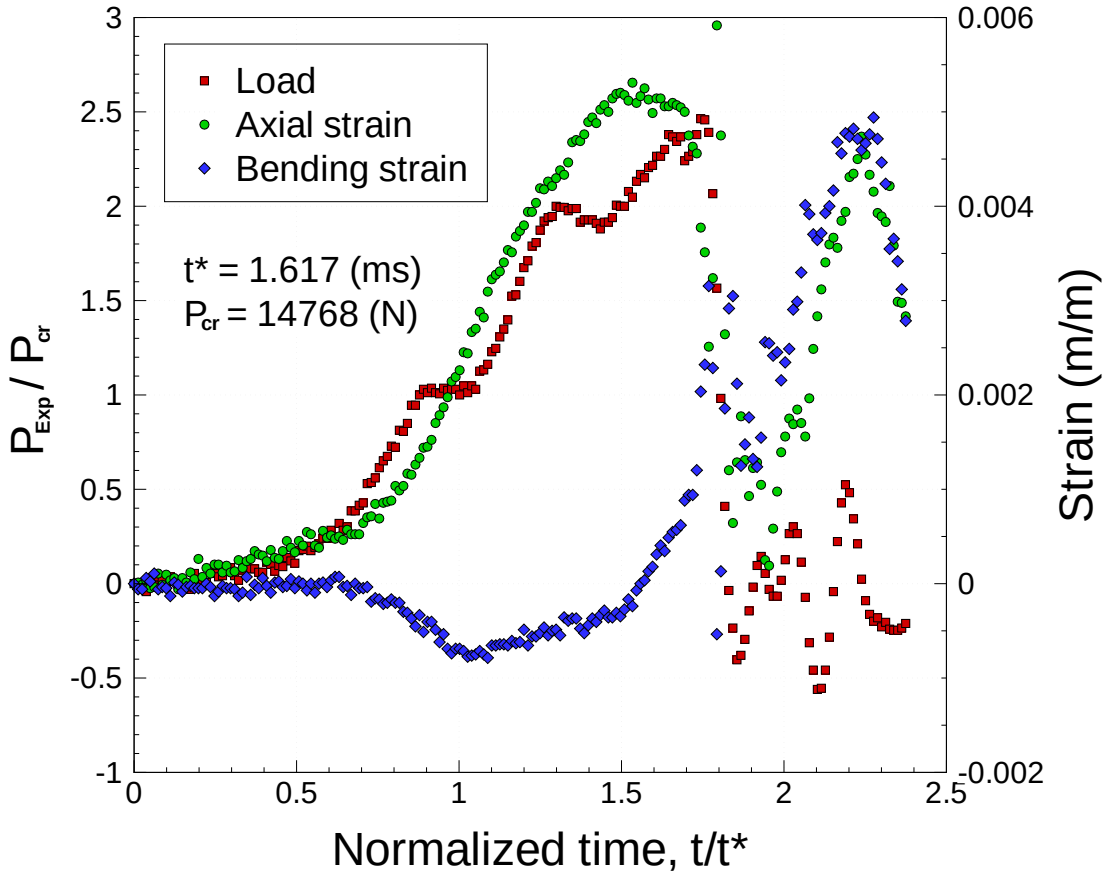

Figure 6.21: Load vs. axial and bending strain. Dynamic instability initiates when the bending strain starts to take off from the axis. The sandwich beam is stabilized until it reaches to the ultimate compressive strength.

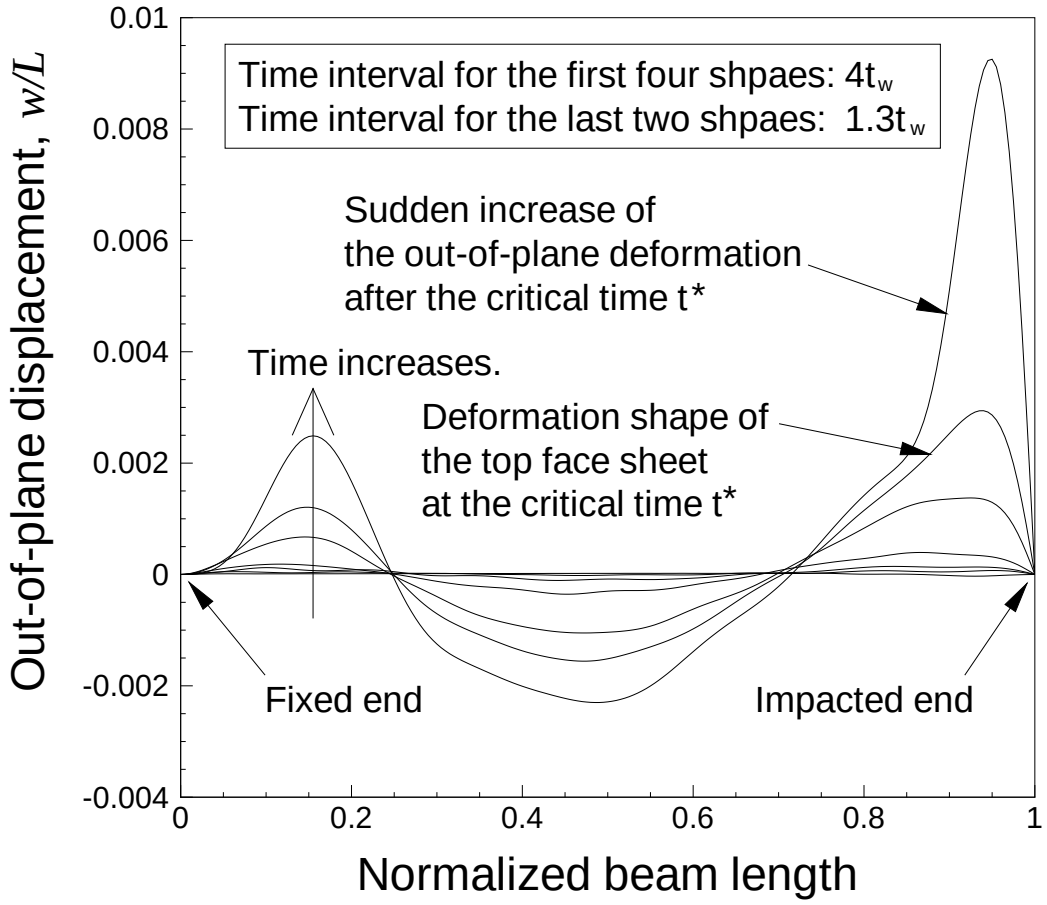

Figure 6.22: Out-of-plane deformation growth of the face sheet computed from FE analysis. The analytical critical time is defined when there is a sudden change of the deformation, causing the loss of load carrying capability of the sandwich beam.

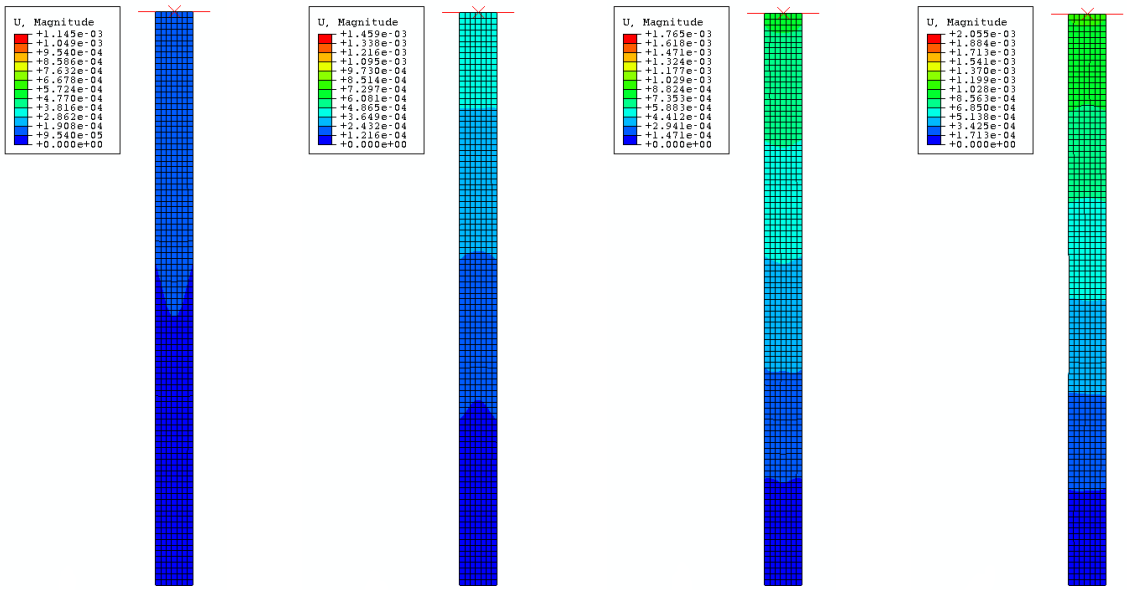

(a) P = 2934 (N) (b) P = 15383 (N) (c) P = 21353 (N) (d) P = 30829 (N)

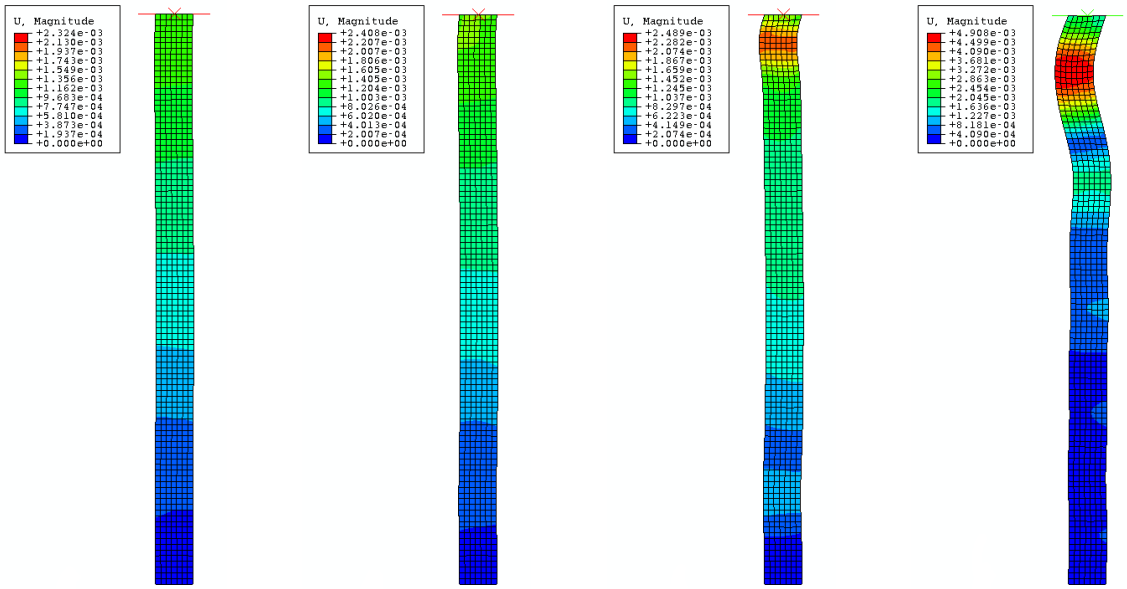

(e) P = 37733 (N) (f) P = 40132 (N) (g) P = 26567 (N) (h) P = 5717 (N)

Figure 6.23: Deformation growth of the sandwich beam from FE analysis. Deformations of the face sheet from (a) to (f) are plotted in Fig. 6.22

CHAPTER VII

Conclusions and suggestions for future work

An analytical method for predicting global and wrinkling instabilities of a sandwich beam is presented. The sandwich beam is modeled as a 2D-linear elastic continuum. Field equations representing a solid slightly deformed from a state of initial stress and under conditions of plane strain is adopted in the analysis. The results obtained yield the buckling stress and the associated wavelength. The results have shown that the buckling stress for the anti-symmetrical deformation mode is always lower that that of the symmetrical one. The buckling behavior of the two modes is parameterized according to the ratio of core thickness to the face sheet thickness. The results are compared with previous experimental results, theoretical analyses, and a finite element analysis prediction. Since the present analysis has fewer assumptions than previous analyses, the limitations of previous investigation are discussed for different combination of geometry and material properties. The results presented here, which have been verified by finite element analysis and compared against experimental results, reproduce the buckling behavior accurately for a wide range of material and geometric parameters. The results that have been presented here are a good prediction of the overall behavior of a sandwich beam in a uniaxial compressive load environment regardless of the core modulus and thickness ratio. In particular,

for thick face sheets and for relatively stiff cores, the present model is found to be more accurate than previous models that assume beam like behavior for the face sheets and neglect the axial load carrying capability of the core. The results from finite element analysis have verified the findings of the present analytical model. In addition the correct formulation of the 2D elastic sandwich column problem has been presented along with a FE formulation of the problem. The latter has revealed deficiencies in the formulation adopted by popular commercial codes[1].

An analytical prediction of dynamic buckling is also presented in this thesis. Dynamic buckling of a structure under uniaxial impact compression is studied. Fully coupled equations of inplane and out-of-plane motions are solved to find the condition of the onset of dynamic buckling. There exists a critical time for the axial strain to satisfy the emergence of the buckling deformation. The bifurcation condition is derived for the simple Euler-Bernoulli beam as well as the sandwich beam. Experimental studies are also performed to investigate the failure mechanism of the sandwich structure under axial impact loading. The sequential responses of the sandwich specimens reveal that the structure initially experiences the axial deformation only until the buckling deformation emerges at a certain load value corresponding to the critical time. FE analysis is also performed to simulate the dynamic response and it is found that there exist a sudden increase of the bending deformation after numerous superpositions of axial strain waves.

The dynamic buckling analysis presented here has numerous potential applications in various fields. The analysis is not dependent on the beam response, but is derived quantitatively so that it is adaptable to various engineering applications. The dynamic buckling analysis can be extended further for better understanding of more

[1]such as ABAQUS

complex material under dynamic loading. The analysis can be improved considering inelastic behavior of the material, orthotropic material, shear deformation, and various combinations of material and geometric properties for the sandwich structure. The analysis combined with fracture mechanics can be used to explain the failure mechanism of the sandwich structure under axial loading. The latter is suggested for future work. In addition, extension of the Euler-Bernoulli model to a Timoshenko beam model is suggested for the impact buckling problem, so that shear deformation effects can be accounted for. Adopting the work of Von Karman [34], the effects of column plasticity on the "critical time to buckle" can be captured and this is also suggested for future work. Finally, it is possible to develop a sandwich beam FE model that includes cohesive zone models for the face sheet-core interface. Such a model in conjunction with an explicit FE code can be used to obtain a comprehensive response model for the sandwich beam impact problem.

BIBLIOGRAPHY

BIBLIOGRAPHY

[1] H. G. Allen. *Analysis and design of structural sandwich panels.* Pergamon Press, Oxford, 1969.

[2] J. Ari-Gur, T. Weller, and J. Singer. Theoretical studies of columns under axial impact and experimental verifications. TAE Rep. 377, Dept. of Aeronautical Engineering, Technion-Israel Institute of Technology, Haifa, Israel, August 1979.

[3] J. Ari-Gur, T. Weller, and J. Singer. Experimental and theoretical studies of columns under axial impact. *International Journal of Solid and Structures*, 18(7):619–641, 1982.

[4] M. Arroyo and T. Belytschko. Large deformation atomistic-based continuum analysis of carbon nanotubes. *Collection of Technical Papers - AIAA/ASME/ASCE/AHS/ASC Structures, Structural Dynamics and Materials Conference*, 2:907–916, 2002.

[5] Z. P. Bažant. A correlation study of formulations of incremental deformation and stability of continuous bodies. *Transactions of the ASME. Series E, Journal of Applied Mechanics*, 38(4):919–928, 1971.

[6] Z. P. Bažant and A. Beghini. Sandwich buckling formulas and applicability of standard computational algorithm for finite strain. *Composites Part B (Engineering)*, 35B(6–8):573–581, 2004.

[7] Z. P. Bažant and A. Beghini. Which formulation allows using a constant shear modulus for small-strain buckling of soft-core sandwich structures. *Journal of Applied Mechanics*, 72(5):785–787, 2005.

[8] Z. P. Bažant and A. Beghini. Stability and finite strain of homogenized structures soft in shear: Sandwich or fiber composites, and layered bodies. *International Journal of Solids and Structures*, 43(6):1571–1593, 2006.

[9] Z. P. Bažant and Luigi Cedolin. *Stability of structures : elastic, inelastic, fracture and damage theories.* Oxford University Press, New York, 1991.

[10] A. Beghini, Z. P. Bažant, A. M. Waas, and S. Basu. Postcritical imperfection sensitivity of sandwich or homogenized orthotropic columns soft in shear and in transverse deformation. *International Journal of Solids and Structures*, 43(18–19):5501–5524, 2006.

[11] C. B. Biezeno and H. Hencky. General theory of elastic stability. In *Proceedings Koninklijke Akademie van Wetenschappen te Amsterdam*, pages 444–456.

[12] M. Biot. Non-linear theory of elasticity and linearised case for a body under initial stress. *Philosophical Magazine*, 27:468–489, 1939.

[13] V. V. Bolotin. *The dynamic stability of elastic systems.* Holden-Day, London, 1964.

[14] D. O. Brush and B. O. Almroth. *Buckling of bars, plates, and shells.* McGraw-Hill, New York, 1975.

[15] B. Budiansky and R. S. Roth. Axisymmetric dynamic buckling of clamped shallow spherical shells. Technical Report NASA TN D-1510, 1962.

[16] General Plastics Manufacturing Company. Fr–6700 product data sheet. Technical report.

[17] J. F. Davidson. Buckling of struts under dynamic loading. *Journal of the Mechanics and Physics of Solids*, 2(1):54–66, 1953.

[18] Clive L. Dym. *Stability theory and its applications to structural mechanics*. Dover Publications, 2002.

[19] L. Fagerberg. Wrinkling and compression failure transition in sandwich panels. *Journal of Sandwich Structures and Materials*, 6(2):129–144, 2004.

[20] N. A. Fleck and I. Sridhar. End compression of sandwich columns. *Composites-Part A: Applied Science and Manufacturing*, 33(3):353–359, 2002.

[21] N. A. Fleck, V. L. Tagarielli, and V. S. Deshpande. The dynamic response of composite sandwich beams to transverse impact. *International Journal of Solids and Structures*, 44(7–8):2442–57, 2007.

[22] Y. Frostig and M. Baruch. High-order buckling analysis of sandwich beams with transversely flexible core. *Journal of Engineering Mechanics*, 119(3):476–495, 1993.

[23] L. Fu and A. M. Waas. Experimental testing of composite rings under uniform external hydrostatic pressure. *Collection of Technical Papers – AIAA/ASME/ASCE/AHS/ASC Structure*, 5:2745–2755, 1994.

[24] J. R. Gladden, N. Z. Handzy, A. Belmonte, and E. Villermaux. Dynamic buckling and fragmentation in brittle rods. *Physical review letters*, 94(3):035503, 2005.

[25] J. N. Goodier and C. S. Hsu. Nonsinusoidal buckling modes of sandwich plates. *Journal of the Aeronautical Sciences*, pages 525–532, 1954.

[26] N. J. Hoff. Dynamics of buckling of elastic columns. *Transactions, Journal of Applied Mechanics*, 18(1):68–74, 1951.

[27] C. S. Hsu. The effects of various parameters on the dynamic stability of a shallow arch. *Journal of Applied Mechanics*, 34(2):349–356, 1967.

[28] J. W. Hutchinson and B. Budiansky. Dynamic buckling estimates. *AIAA Journal*, 4(3):525–530, 1966.

[29] W. Ji and A. M. Waas. Wrinkling and edge buckling in orthotropic sandwich beams. *Journal of Engineering Mechanics*, 134(6):455–461.

[30] W. Ji and A. M. Waas. Global and local buckling of a sandwich beam. *Journal of Engineering Mechanics*, 133(2):230–237, February 2007.

[31] W. Ji and A. M. Waas. Dynamic bifurcation buckling of an impacted column. *International Journal of Engineering Science*, 46(10):958–967, 2008.

[32] N. Jones. *Structural Impact*. Cambridge University Press, 1997.

[33] G. A. Kardomateas. Wrinkling of wide sandwich panles/beams with orthotropic phases by an elastic approach. *Journal of Applied Mechanics*, 72(6):818–825, 2005.

[34] T. V. Karman and P. Duwez. Propagation of plastic deformation in solids. *Journal of Applied Physics*, 21(10):987–994, 1950.

[35] S. Kenny, F. Taheri, and N. Pegg. Dynamic elastic buckling of a slender beam with geometric imperfections subject to an axial impulse. *Finite Elements in Analysis and Design*, 35(3):227–246, 2000.

[36] C. Koning and J. Taub. Impact buckling of thin bars in the elastic range hinged at both ends. *National Advisory Committee for Aeronautics – Technical Memorandums*, (748):32, 1934.

[37] L. Léotoing, S. Drapier, and A. Vautrin. First applications of a novel unified model for global and local buckling of sandwich columns. *European Journal of Mechanics, A/Solids*, 21(4):683–701, 2002.

[38] L. Léotoing, S. Drapier, and A. Vautrin. Using new closed-form solutions to set up design rules and numerical investigations for global and local buckling of sandwich beams. *Journal of Sandwich Structures and Materials*, 6(3):263–289, 2004.

[39] R. P. Ley, W. Lin, and U. Mbanefo. Facesheet wrinkling in sandwich structures. Technical Report NASA CR-1999-208994, 1999.

[40] H. E. Lindberg and A. L. Florence. *Dynamic pulse buckling : theory and experiment.* Martinus Nijhoff, Dortrecht, 1987.

[41] A. E. H. Love. *A treatise on the mathematical theory of elasticity.* Cambridge University Press, London, 1892.

[42] J. H. Meier. On the dynamics of elastic buckling. *Journal of the Aeronautical Sciences*, 12(4):433–440, 1945.

[43] K. Niu and R. Talreja. Modeling of wrinkling in sandwich panels under compression. *Journal of Engineering Mechanics*, 125(8):875–883, 1999.

[44] V. V. Novozhilov. *Foundations of the nonlinear theory of elasticity.* Graylock, Rochester, N.Y., 1953.

[45] F. J. Plantema. *Sandwich construction: the bending and buckling of sandwich beams, plates, and shells.* Wiley, New York, 1966.

[46] E. Sevin. On elastic bending of columns due to dynamic axial forces including effects of axial inertia. *Transactions, Journal of Applied Mechanics*, 27(1):125–131, 1960.

[47] G. J. Simitses. *Dynamic stability of suddenly loaded structures.* Springer-Verlag, New York, 1989.

[48] J. Singer, J. Arbocz, and T. Weller. *Buckling experiments: experimental methods in buckling of thin-walled structures.* Wiley, New York, 1998.

[49] V. Sokolinsky and Y. Frostig. Boundary condition effects in buckling of soft core sandwich panels. *Journal of Engineering Mechanics*, 125(8):865–874, 1999.

[50] J. Taub. Impact buckling of thin bars in elastic range for any end condition. *National Advisory Committee for Aeronautics – Technical Memorandums*, (749):60, 1934.

[51] M. T. Tilbrook, V. S. Radford, D. D. abd Deshpande, and N. A. Fleck. Dynamic crushing of sandwich panels with prismatic lattice cores. *International Journal of Solids and Structures*, 44(18–19):6101–6123, 2007.

[52] E. Trefftz. Stability of elastic equilibrium. *Zeitschrift für Angewandte Mathematik und Mechanik*, 13:160–165, April 1933.

[53] A. M. Waas. Effect of interphase on compressive strength of unidirectional composites. *Journal of Applied Mechanics*, 59(2):S183–S188, 1992.

[54] A. M. Waas, C. D. Babcock Jr., and W. G. Knauss. A mechanical model for elastic fiber microbuckling. *Journal of Applied Mechanics*, 57(1):138–149, 1990.

[55] S. A. Wainwright, W. D. Biggs, J. D. Currey, and J. M. Gosline. *Mechanical Design in Organisms*. Princeton University Press, New Jersey, 1982.

[56] A. Wang and W. Tian. Twin-characteristic-parameter solution for dynamic buckling of columns under elastic compression wave. *International Journal of Solids and Structures*, 39(4):861–877, 2002.

[57] Z. Wei, K.P. Dharmasena, H.N.G. Wadley, and A.G. Evans. Analysis and interpretation of a test for characterizing the response of sandwich panels to water blast. *International Journal of Impact Engineering*, 34(10):1602–1618, 2007.

[58] A. Wineman. Bifurcation of response of a nonlinear viscoelastic spherical membrane. *International Journal of Solids and Structures*, 14:197–212, 1978.

[59] L. Yueming, A. V. Spuskanyuk, S. E. Flores, D. R. Hayhurst, J. W. Hutchinson, R. M. McMeeking, and A. G. Evans. The response of metallic sandwich panels to water blast. *Journal of Applied Mechanics*, 74(1):81–99, 2007.